Van Allen Radiation Belt Electron Dynamics During Geomagnetic Storms

by

Leonid Olifer

A thesis submitted in partial fulfillment of the requirements for the degree of

Doctor of Philosophy

Department of Physics

University of Alberta

Abstract

Space radiation is often identified as one of the most prominent dangers of space exploration. It mostly originates at the Sun and streams into the space between planets, creating hazardous radiation conditions at every point of the solar system which is not shielded by an atmosphere. Therefore, it is crucial to characterize this radiation and determine the worst-case radiation levels to aid in the design of radiation-tolerant spacecraft and satellites, mitigate damaging space radiation effects, and protect humans during the exploration of deep space. This thesis focuses on studying the dynamics of the electron radiation trapped in the magnetic field of the Earth, also known as Van Allen radiation belts, during geomagnetic storms that create the most hazardous radiation conditions around our planet.

Often, the dynamics of the electron radiation belt are asserted to result from a delicate balance between acceleration and loss. In contrast, this thesis shows evidence for some remarkable repeatability in flux dynamics associated with both the loss and acceleration phases of geomagnetic storms. In relation to loss, this thesis presents a study of 69 geomagnetic storms that demonstrate intense and isolated compressions of the magnetopause, characterized by the location of the last closed drift shell (LCDS), to assess the repeatability of loss processes associated with magnetopause shadowing. A superposed epoch analysis of the particle dynamics associated with periods of low LCDS reveals a clear and repeatable organization of the loss as a function of both L^* and energy for electrons with energies above 600 keV. The high repeatability reveals

almost the same fraction of pre-existing particles is rapidly lost in every event. This can be explained by the fast outward radial diffusion of the electrons to the compressed LCDS.

On the other hand, the lower energy electron population does not experience loss over the course of the storm but is instead accelerated to levels two to three orders of magnitude above the pre-storm level within a period of hours at the beginning of the storm. Significantly, the maximum flux reached in every event for this lower energy population ($\lesssim$800 keV) is identical in almost every storm! Remarkably, the maximum flux reaches the theoretically derived limit exactly as predicted by the Kennel and Petschek (1966) theory developed more than 50 years ago. A superposed epoch analysis of 70 strong geomagnetic storms shows that the Kennel-Petschek limit impacts the radiation belt electron dynamics in almost every storm of at least strong intensity in the Van Allen Probes era (2012-2019). The study presented in this thesis also reveals how the Kennel-Petschek theory elegantly explains the evolution and hardening of the electron spectrum up to strongly relativistic (up to 2.6 MeV) energies, introducing an energy-dependent maximum flux limit. No current radiation belt models include this theory. As shown here, this is an important process that has a strong and sometimes controlling and limiting effect on electron flux. Its impacts appear to be essential for understanding and accurately predicting the absolute limits of the most extreme electron space radiation.

Finally, this thesis presents studies of geomagnetic storms with very fast radiation belt acceleration that increases the electron flux of relativistic or strongly relativistic electrons by orders of magnitude over very short periods of time ($\lesssim$1-hr). The multipoint measurements by the Van Allen Probes reveal how the apparent phase space density (PSD) peak, commonly associated with local acceleration by the chorus waves, can instead arise from aliasing monotonic PSD profiles which are rapidly increasing due to acceleration from very fast

inwards radial diffusion. In the absence of such multi-satellite conjunctions during fast acceleration events, such peaks might otherwise be interpreted as caused by local acceleration processes. As also shown in this thesis, utilizing an even larger electron radiation belt measurement dataset from 20 Global Positioning System satellites can reveal even faster radiation belt dynamics with greater detail.

Overall, this thesis provides an extensive study of the storm-time radiation belt dynamics, the main results of which not only contribute to the understanding of the dynamics of the near-Earth plasma but also can be used for the improved radiation specification models for designing radiation-hard space infrastructure.

Preface

This thesis is an original work by Leonid Olifer.

Chapter 3 was published in the Journal of Geophysical Research: Space Physics as **Olifer, L.**, I. R. Mann, L. G. Ozeke, S. G. Claudepierre, D. N. Baker, and H. E. Spence (2021), *On the Similarity and Repeatability of Fast Radiation Belt Loss: Role of the Last Closed Drift Shell*.

Chapter 4 was published in the Geophysical Research Letters as **Olifer, L.**, I. R. Mann, A. Kale, B. H. Mauk, S. G. Claudepierre, D. N. Baker, H. E. Spence, and L. G. Ozeke (2021), *A Tale of Two Radiation Belts: The Energy-dependence of Self-limiting Electron Space Radiation*.

Chapter 5 was accepted for publication in the Journal of Geophysical Research: Space Physics as **Olifer, L.**, I. R. Mann, S. G. Claudepierre, D. N. Baker, H. E. Spence, and L. G. Ozeke,*A Natural Limit to the Spectral Hardness of Worst-case Electron Radiation in the Terrestrial Van Allen Belt*.

Chapter 6 was published in the Geophysical Research Letters as **Olifer, L.**, I. R. Mann, L. G. Ozeke, S. K. Morley, and H. L. Louis (2021), *On the Formation of Phantom Electron Phase Space Density Peaks in Single Spacecraft Radiation Belt Data*.

Chapter 7 is currently being prepared for peer-review as **Olifer, L.**, S. K. Morley, L. G. Ozeke, I. R. Mann, M. Kalliokoski, M. Henderson, R. Niyazov, and A. Hoover, *Rapid Acceleration Bursts in the Van Allen Radiation Belt*. This paper has been sent for review in Nature Communications but despite positive technical reviews was rejected by the editor due to its likely generation of only "specialist interest". To be submitted to an alternative discipline-specific journal.

In all these publications, I was responsible for the data analysis and the manuscript composition. I. R. Mann was the supervisor for research presented in Chapters 3 to 6 and S. K. Morley was the supervisor for the project in Chapter 7. L. G. Ozeke, S. G. Claudepierre, D. N. Baker, H. E. Spence, A. Kale, B. H. Mauk, H. L. Louis, M. Kalliokoski, M. Henderson, R. Niyazov, and A. Hoover contributed as the coauthors by providing constructive feedback on the results of my research and the journal manuscript composition.

Acknowledgements

First, I would like to thank my supervisor, Prof. Ian Mann, for all the help and guidance that he has given me throughout my Ph.D. Without him, this thesis would not have been possible. I am also grateful to Dr. Steve Morley for his advice and discussions that led to many successfully published papers, some of which are prominently featured in this thesis. Ian and Steve, you have set an extremely high bar for what a scientific leader should be like — a level that I will strive to reach in the future. I am also grateful to my supervisory committee, Prof. Richard Sydora and Prof. Joseph Maciejko, Arm's length examiners Prof. Gregory Sivakoff and Prof. Richard Marchand, as well as the External examiner Prof. Emilia Kilpua, for their feedback and constructive questions on my research and this thesis.

I would also like to thank all of the extremely smart people with whom I worked during my degree (in no particular order) Louis Ozeke, Jonny Rae, Seth Claudepierre, Kyle Murphy, Harlan Spence, Dan Baker, Mike Henderson, Barry Mauk, Allison Jaynes, Dave Knudsen, Kathryn McWilliams, Jøran Moen, Andres Spicher, Hannah Louis, Milla Kalliokoski, Andy Kale, Rustam Niyazov, Andrew Hoover, Harriet George, Hannah Parry, Katelyn Ball, Sam Walton, and many many more. Your enthusiasm, passion for physics, love for exploring the unknown, and most importantly chats about space over coffee, or something stronger, have been the decisive factor for me to continue my academic track.

Finally, many thanks to my friends, family, and loved ones for their support and love which helped me greatly to find a home far away from home.

Table of Contents

List of Tables

List of Figures

List of Acronyms

AU	–	Astronomical unit
CGS	–	Centimetre–gram–second system of units
EMIC	–	Electromagnetic ion cyclotron
GSE	–	Geocentric solar ecliptic
GSM	–	Geocentric solar magnetospheric
ICME	–	Interplanetary coronal mass ejection
IMF	–	Interplanetary magnetic field
KP	–	Kennel-Petschek
LCDS	–	Last closed drift shell
MSE	–	Mean square error
PAD	–	Pitch angle distribution
PSD	–	Phase space density
SEP	–	Solar energetic particles
SI	–	International system of units
SIR	–	Stream interaction region
SSPB	–	Symmetric signed percentage bias
ULF	–	Ultra-low frequency
VLF	–	Very-low frequency

Chapter 1

Introduction

It is believed that a large portion of the visible Universe exists in the form of plasma. Plasma, comprising a hot ionized gas, permeates the interplanetary and interstellar media, composes stellar atmospheres, and plays a role in planetary ionospheres, nebulas, and aurorae. Throughout the cosmos, plasmas exist in a variety of states with different densities and temperatures with a variety of different physical processes driving their dynamics, being strongly influenced by both electric and magnetic fields. This chapter presents an overview of various plasma environments within our solar system with a focus on the main subject of this thesis – the Van Allen radiation belts of the Earth and the processes that govern their dynamics.

1.1 Sun-Earth Coupling

Throughout the Solar system, the vast majority of various plasma populations originate from the Sun. The solar atmosphere expands into interplanetary space to form the solar wind that carries the interplanetary magnetic field (IMF) with it. Depending on the conditions at the solar surface, this plasma outflow can vary greatly in terms of speed, density, and, characteristics of the magnetic fields embedded within it. Such variability creates a dynamic environment around different planets which in turn may react differently to these changes depending on their own characteristics and structure. This section focuses on the influence that the solar wind produces in near-Earth space, specifically how it can change the radiation conditions around our planet, and what are the

typical characteristics of these interactions. So naturally, it is good to start this description with the source of the solar wind – the Sun.

1.1.1 The Sun

The Sun is a main sequence G-type star located 8 light minutes, or 1 astronomical unit (AU), from the Earth. It is a ball of hot plasma that is held together by gravitational forces, with an energy source sustained by nuclear fusion processes that are active in the Sun's core. It radiates energy predominantly in the form of visible light, and infrared and ultraviolet radiation, with a similar intensity to a black body heated to 5777 K. The Sun is mostly composed of hydrogen (about 2/3 of its mass), helium (about 1/3), and much smaller quantities of heavier elements like oxygen and iron (e.g., *Priest*, 1995). It is by far the heaviest object in the solar system with an equatorial radius of 109 times that of the Earth and almost 333,000 times heavier than our planet. Overall, from the perspective of an astrophysicist, the Sun is representative of a yellow dwarf star, formed approximately 4.6 billion years ago and has ∼5.5 billion years before its transformation into a red giant. However, from the perspective of a space physicist, the Sun and its interactions with the planets is one of the most exciting subjects to study, partially due to the lack of in-situ observations from any other planetary system.

From inside out, the solar interior is composed of the core, radiative zone, convection zone, photosphere, chromosphere, and corona. The latter three layers compose the solar atmosphere, with the outermost corona being the hottest ($\sim 2 \cdot 10^6$ K) and the photosphere being responsible for the majority of the electro-magnetic radiation emitted (characteristic temperature of 5777 K). The anomalous heating of the solar corona is typically attributed to the dissipation of the magnetohydrodynamic waves (e.g., *Golub*, 2010), but the processes responsible remain poorly understood. In particular, particles in the corona can be heated or accelerated due to the energy deposition from waves that propagate from the solar surface into the corona (e.g., *Priest*, 1982). Alternatively, plasma can be heated through magnetic reconnection processes that rapidly accelerate particles through the transfer of energy stored in the

magnetic field into kinetic and thermal energy in plasma (e.g., *Priest*, 1982, 1995). Due to the lower densities of the corona in comparison to the interior of the Sun, these processes can lead to the anomalous heating of the plasma population in the corona.

Solar wind particles can escape the gravitational pull of the Sun and stream into interplanetary space. However, the solar wind is not steady and is commonly accompanied by explosive bursts of plasma that travel into interplanetary space as a result of coronal mass ejections (e.g., *Kilpua et al.*, 2017). As the Sun goes through the solar cycle – an 11-year period during which the North and South poles of the Sun flip – the magnetic activity at the Sun's surface and thus that of the solar wind changes greatly (e.g., *McComas et al.*, 2003). In particular, during solar maximum, the solar activity is much more intense and explosive in nature, when compared to quiet conditions and more steady solar wind streams that dominate solar minimum. The next section provides some further details about the solar wind and structures within it, as well as their characteristics at Earth's orbit.

1.1.2 Solar Wind

According to the first theoretical model of the solar wind as a rapidly expanding solar corona developed by *Parker* (1958), the solar wind speed, $v(r)$, can be calculated using the following equation (1.1):

$$v(r) \approx 2\,(RT)^{1/2} \left(\ln \frac{2RTr}{GM_{\odot}} \right)^{1/2}, \tag{1.1}$$

where r is the distance from the Sun, R is the gas constant, T is the coronal temperature, G is the universal gravitational constant, and $M_{\odot}$ is the mass of the Sun. According to this model, the solar wind speed in near-Earth space can be on the order of 200–1000 km/sec, depending on the temperature of the solar corona. In-situ observations of the plasma properties around our planet show that the solar wind mostly consists of ionized hydrogen, a much smaller number of ionized helium, an even smaller number of heavier ions, and electrons in equal numbers to that of the ions. At 1 AU, the average proton

number density in the solar wind is approximately 6.6 cm^{-3} and the electron density is around 7.1 cm^{-3} (e.g, *Hundhausen*, 1995). The solar wind also carries a magnetic field from the Sun that is stretched into the interplanetary space, such that its magnetic field lines are almost parallel to the plane of the ecliptic and approximately 45° to a line connecting the Sun and the Earth (e.g., *Hundhausen*, 1995). This magnetic field is commonly referred to as interplanetary magnetic field (IMF). Its strength is relatively weak and on the order of 10 nT (*Baumjohann and Treumann*, 1996). Interestingly, the sound speed in the solar wind is approximately 60 km/s, which means that even a steady solar wind is supersonic and its interaction with any object in the solar system includes the creation of a shock region upstream where its speed is lowered.

Due to the dynamic nature of the solar corona, the steady solar wind stream can be accompanied by solar ejections, explosive releases of plasma into interplanetary space, or be perturbed by fast streams which overtake the ambient solar wind. The most prominent examples of these processes in the heliosphere can be the formation of interplanetary coronal mass ejection (ICME) or a solar wind stream interaction region (SIR). For example, an ICME can be created by a magnetic field reconnection inside a prominence (*Webb and Howard*, 2012), which causes an outer part of the prominence to break off from the Sun and stream into space. ICMEs are prevalent during the period of solar maximum and can reach speeds up to 2000 km/s. The SIR is formed by the interaction of a high-speed plasma that originates at a coronal hole with the preceding slower solar wind (e.g., *Kilpua et al.*, 2017). This interaction creates a region of higher plasma density. SIRs are commonly long-lived and can exist for up to a few months, creating solar wind conditions that vary periodically (at ∼27 day intervals corresponding to the solar rotation period). Both ICMEs and SIRs cause substantial changes in the typical solar wind density, velocity, and embedded magnetic field, thus creating a highly variable, both spatially and temporally, interplanetary environment. Thus, the presence of ICMEs, SIRs, or any other solar transients can cause a variable response from a planetary magnetosphere, resulting in a number of processes. Periods

of strong interaction between planetary magnetospheres and solar wind are generally referred to as magnetic storms.

1.1.3 Earth's Magnetosphere

Close to the planet's surface, the magnetic field of the Earth is well represented by a dipole field with the magnetic dipole being misaligned with the rotational axis of the Earth by ∼11.3° and offset from its center by ∼550 km (e.g., *Baumjohann and Treumann*, 1996; *Russell*, 1995). Its magnetic moment has a magnitude of $8.07 \cdot 10^{22}$ Am^2. The current understanding is that the magnetic field is created by the self-sustaining processes of a dynamo through which the movement of the liquid metal inside the Earth's core can sustain the generation of the dipole-like magnetic field over long periods of time (e.g., *Akasofu and Chapman*, 1973; *Glatzmaier and Roberts*, 1995). Note that the magnitude of the magnetic moment, its offset, and tilt angle change over time and are usually described by empirical models. One of the most commonly used ones is the International Geomagnetic Reference Field (IGRF) model (e.g., *Alken et al.*, 2021).

Further from the Earth's surface, the dipole field is distorted due to the interaction with the solar wind and IMF (e.g., *Hundhausen*, 1995). Figure 1.1 shows a schematical representation of the Earth's magnetic field and some of its regions. Curved solid lines with arrows represent the magnetic field lines and their direction which are distorted after the interaction between the solar wind and the Earth. The dotted lines represent the purely dipolar magnetic field indicating schematically the distortion of the magnetic field. The outermost boundary of the Earth's magnetosphere is called the bow shock. It is a shock boundary created ∼10-13 R_E from the Earth's surface by the supersonic solar wind, beyond which the solar wind slows and increases its density. The next boundary, located ∼7-10 R_E from the Earth at the dayside along the Sun-Earth line is called the magnetopause. It separates the distorted magnetic field of the Earth from that of the IMF. While Figure 1.1 represents a schematic of the static background magnetic field around our planet, it is important to note that the magnetosphere is constantly perturbed by the variable solar

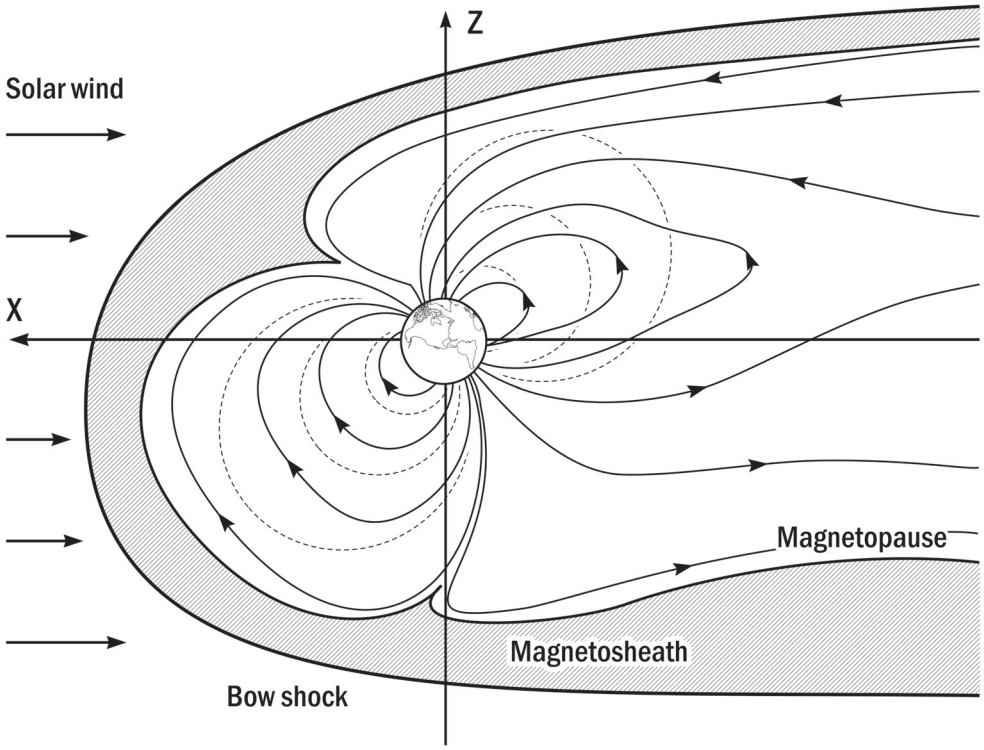

Figure 1.1: Schematic representation of the magnetic field lines of the Earth. Solid curved lines represent the magnetic field lines of the Earth with arrows showing the direction of the magnetic field. Dotted lines around the Earth represent the field lines of the magnetic dipole for comparison with the more realistic representation. The schematic also labels various magnetospheric boundaries. From *Olifer* (2019).

wind. Figure 1.1 also shows a situation where field lines from the Earth do not connect to the IMF – a so-called closed magnetosphere. During periods of southward IMF, magnetic reconnection strongly couples the solar wind to the magnetosphere and creates a cycle of magnetic convection known as the Dungey cycle (*Dungey*, 1961).

This solar wind coupling can also excite plasma waves inside the magnetosphere. In turn, these waves can alter the trapped plasma populations by, for example, accelerating lower energy electrons up to relativistic energies. Notably, wave activity is higher during geomagnetic storms and during fast or rapidly varying solar wind conditions. This thesis will investigate interactions between various plasma waves in the magnetosphere with the charged particles that are

trapped in the magnetic field of the Earth.

The majority of the terrestrially trapped charged particles originate at the Sun and are captured by the magnetosphere from the solar wind, with a smaller portion originating from the Earth's ionosphere. Thus, the plasma around our planet is mostly composed of electrons and protons with very small portions of He^+, O^+, and heavier ions. Regions of the Earth's magnetosphere can be separated by the energies of the dominant populations. For example, cold plasma in the plasmasphere and energetic particles in the ring current and the Van Allen radiation belts. While overlapping in some regions, these plasma populations are differentiated by their origin and particle energies.

The plasmasphere is a torus-shaped region within $\sim$4 R_E from the center of the Earth. It contains mostly cold, low-energy ($\lesssim$ 1 eV) particles that drift upwards from the ionosphere and corotate with the Earth. This population is mostly stable due to its proximity to the Earth's surface. However, during times of high geomagnetic activity, the outer plasmasphere boundary, the plasmapause, gets closer to the Earth additionally forming a plasmaspheric plume on the dusk side, which can extend all the way to the magnetopause (e.g., *Walsh et al.*, 2013). This region is also populated by waves within the extremely low frequency (ELF) range (300 Hz to 10 kHz) called plasmaspheric hiss.

As will be explained in Chapter 2, energetic electrons and protons drift around the Earth in opposite directions, creating a steady electric current known as the ring current that is mostly carried by protons. The major source of particles in the ring current is the solar wind. The ring current occupies the region of the magnetosphere above $\sim$4 R_E but sometimes overlaps with the plasmasphere, extending further into the inner magnetosphere. The majority of particles in the ring current are protons and electrons with energies around $\sim$10-200 keV, with a very minor inclusion of heavier ions. The dynamics of the ring current are also commonly used to identify periods of storm-time geomagnetic activity using the disturbance storm time (Dst) index.

The Van Allen radiation belts are formed by highly energetic, $\sim$200 keV-10 MeV, electrons and protons. They typically extend from $\sim$2 to 7 R_E and

are usually shaped as two toroidal belts surrounding the Earth. The outer Van Allen radiation belt population is highly dynamic with characteristics that strongly depend on the level of solar-terrestrial coupling. This thesis in particular focuses on the dynamics of the Van Allen belt during storm times.

1.1.4 Van Allen Radiation Belts

Discovered in early 1958, the Van Allen radiation belts comprise a highly energetic plasma population trapped around the Earth. Typically, they form two distinguishable regions – the inner and the outer belts. The inner belt is located around 1.5-2 R_E from the center of the Earth and consists of low energy electrons (<0.05 MeV), much higher energy protons (with energies ∼1-10 MeV and more), and heavier ions like helium or oxygen (e.g., *Walt*, 1994). The inner belt population remains largely unaltered by geomagnetic storm processes, because of its proximity to the Earth's surface and the relative stability of the background magnetic field there. However, the most intense geomagnetic storms can still influence those regions (e.g., *Baker et al.*, 2004; *Ozeke et al.*, 2018).

The outer radation belt is located ∼3-7 R_E from the center of the Earth and consists mostly of relativistic electrons with energies >500 keV (e.g., *Walt*, 1994). The magnetic field of the Earth is highly dynamic in that region due to the interaction with the solar wind. Therefore, the outer radiation belt is prone to drastic changes in its population which can occur on timescales of minutes to days or even years (e.g., *Rodger et al.*, 2010; *Olifer et al.*, 2018). These changes may even result in the splitting of the outer radiation belt into two or even more belts, creating a three- or four-belt morphology around the Earth (e.g., *Mann et al.*, 2016). Figure 1.2 shows diagrams of the median flux of charged particles in the inner and outer belts as provided by the empirical, epoch-independent NASA AP8/AE8 model (*Sawyer and Vette*, 1976; *Vette*, 1991). Note that this model is storm-time independent and only capable of predicting typical fluxes present in the radiation belts, and does not include any storm-time variability. Moreover, recent studies showed that it, or its more modern counterpart AP9/AE9, is also incapable of predicting worst-case

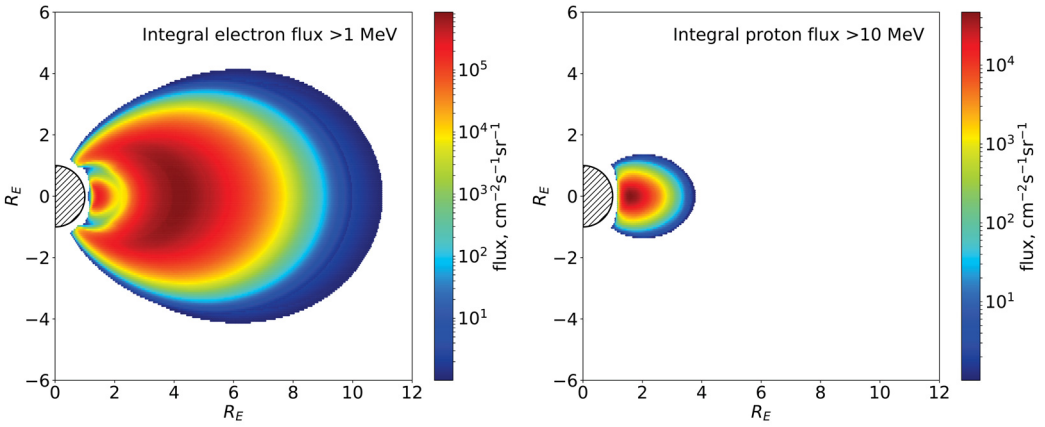

Figure 1.2: Integral, omnidirectional electron (left panel) and proton (right panel) fluxes as provided by NASA AP8/AE8 model (*Sawyer and Vette*, 1976; *Vette*, 1991). Note, that the cavity (slot) between inner and outer belts is present for electron >1 MeV population and this population is larger in the outer belt. Meanwhile, the majority of protons with energies >40 MeV mostly concentrate in the inner belt. Adopted from *Walt* (1994)

scenario radiation levels around the Earth (e.g., *Zhang et al.*, 2021).

The highly dynamic nature of the terrestrial radiation belt poses a major obstacle to creating accurate models of the near-Earth radiation environment, and therefore for mitigating radiation impacts on spacecraft infrastructure. Over the course of a geomagnetic storm, the radiation belt flux, a measure of how many charged particles there are in the belt, can change by multiple orders of magnitude over very short periods of time. The possible damaging effects of the changing radiation conditions on satellites, and ways to mitigate them, are presented in the next section of this chapter.

1.2 Space Weather and its Impacts

Space weather commonly refers to the cumulative conditions of the Sun, solar wind, planetary magnetospheres, and ionospheres that can affect the operations of any kind of infrastructure and impact the health or lives of humans. Extreme space weather events can critically damage or even destroy space- or Earth-based infrastructures with the potential for cascading failures through key services like power, communication, healthcare, and/or stock trading (e.g.,

U.S. National Space Weather Plan, 2019). Thus, understanding the processes that lead to the formation of severe space weather events, their impacts, and possible outcomes are the main steps required in order to protect society from such dangerous effects.

Typically, extreme space weather at the Sun or solar wind can be linked to various explosive events that occur on the solar surface and propagate into interplanetary space. They include solar flares, solar energetic particles (SEPs), and interplanetary coronal mass ejections (ICMEs, discussed earlier in the chapter) (e.g., *Schwenn*, 2006). Solar flares are sudden releases of a massive amount of electromagnetic radiation across a wide wavelength range (from radio waves to gamma rays). Typically, they heat up the terrestrial atmosphere within minutes, causing it to expand, thus leading to increased drag on satellites and a shortening of their projected orbital lifetime. A similar process likely caused 40 SpaceX Satlink satellites to quickly decay their very low orbit and burn up in the atmosphere in February 2022.

Another example of extreme and potentially damaging space weather arises from SEPs, that are comprised of charged particles, accelerated to near-relativistic energies, and may, among other things, severely endanger astronauts that are located outside the magnetic protection afforded by planetary magnetospheres. For example, only luck prevented the astronauts of the Apollo 16 and 17 missions being caught in the SEP event which occurred on August 4, 1972 (e.g., *Knipp et al.*, 2018). Coronal mass ejections are not extremely dangerous on their own when encountered in interplanetary space, apart from increased plasma density within them. However, upon reaching the Earth, ICMEs cause geomagnetic storms that in turn can be detrimental to space-based and ground-based infrastructure.

1.2.1 Geomagnetic Storms

Typically, geomagnetic activity is characterized using geomagnetic indices that are derived from ground-based magnetometer measurements. The disturbance storm time (Dst) index is classically used to determine the times of geomagnetic storms, classify their intensity, and separate various storm phases. Dst is

determined using a network of near-equatorial magnetometers that measure the hourly variation of the horizontal component of the equatorial magnetic field. Changes in Dst are caused by the strengthening of the ring current, and thus the magnetic field that is generated by it, during the geomagnetically active times. According to the *Loewe and Prölss* (1997) classification, geomagnetic conditions with Dst< -30 nT can be classified as a geomagnetic storm. The periods of decreasing (more negative) Dst are commonly referred to as the main phase of the storm, and the subsequent periods of increasing (less negative) Dst are referred to as the recovery phase. Other geomagnetic indices that can be used for determining geomagnetically active times include the planetary Kp index (determined using the largest magnetic field variation in magnetometer data across various latitudes), auroral electrojet index (AE, determined using horizontal magnetic field variation within the auroral oval), or SYM-H (equivalent to a continuous measure of Dst and determined using north-south component of geomagnetic disturbances at mid-latitudes).

Figure 1.3 shows an example summary of solar wind conditions, geomagnetic indices, and radiation belt response during a strong geomagnetic storm for September 7-9, 2017. It is adapted from *Olifer et al.* (2021c) (also Chapter 6 of this thesis) and shows (a) the solar wind speed, (b) the $z-$component of the interplanetary magnetic field (IMF), B_z, in the geocentric solar magnetospheric (GSM) coordinates (c) solar wind dynamic pressure, (d) resulting Dst and Kp indices, and (e) radiation belt response characterized by 3 MeV electron flux measured by constellation of Global Positioning System (GPS) satellites. Figure 1.3 shows that the main phase of the storm (decreasing, more negative, Dst between $\sim$20 UT on September 7 and $\sim$2 UT on September 8) is accompanied by a strong increase in the solar wind speed, dynamics pressure, and increasingly southward component of the IMF – all characteristic of a geomagnetically active period. This time period is also accompanied by the loss of the relativistic electrons from the radiation belt (Figure 1.3e) with the 3 MeV electron flux decreasing by more than 3 orders of magnitude over only a few hours.

Following the end of the main phase of the storm, the recovery phase begins

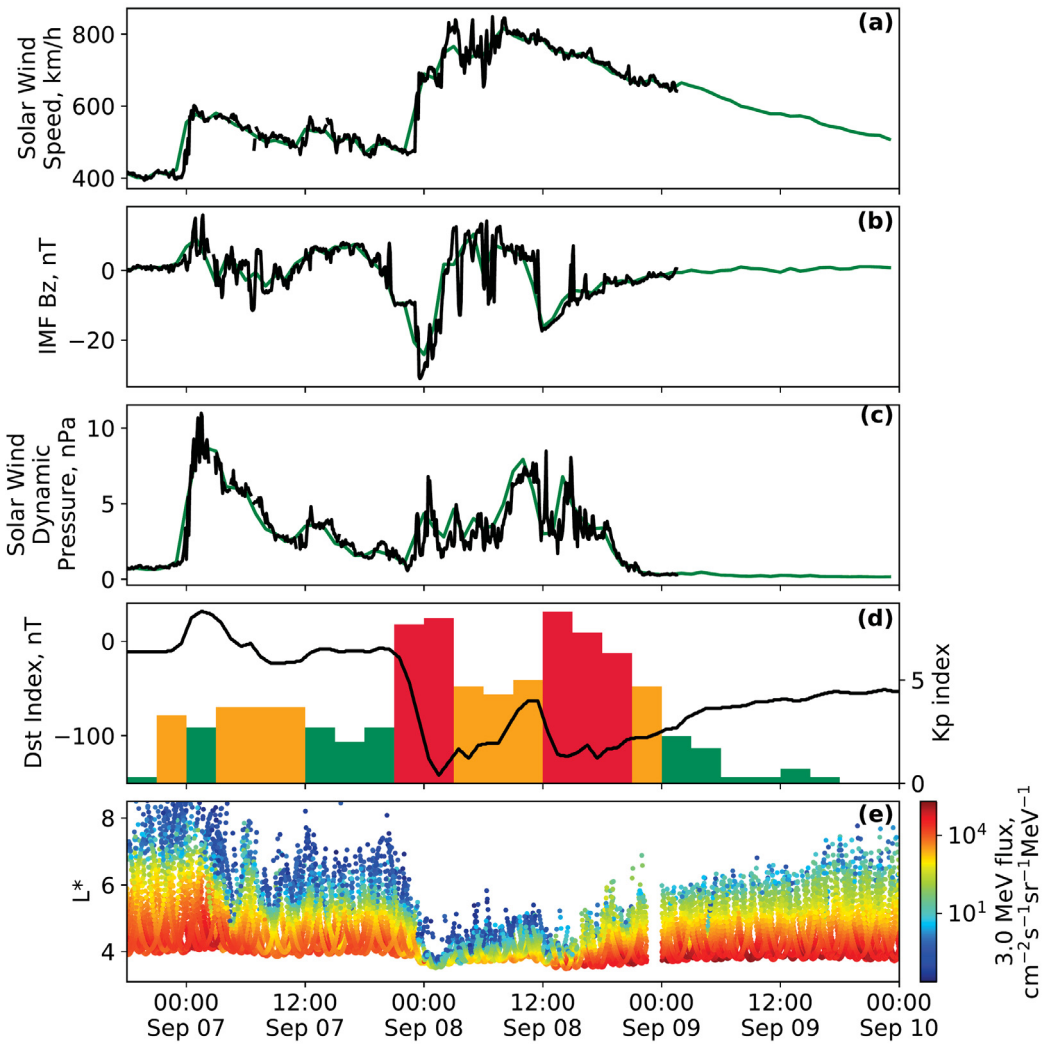

Figure 1.3: (a) Solar wind speed, (b) B_z component of the interplanetary magnetic field (IMF) in GSM coordinates, (c) solar wind dynamic pressure (5-min data in black, and 1-h resolution data in green). High-resolution solar wind data is absent for the majority of September 9. (d) Dst index as a line plot and Kp index as a histogram (secondary y-axis). (e) 3 MeV electron flux measured by the constellation of global positioning system (GPS) satellites (*Morley et al.*, 2017) as a function of time and L^*. L^* is a coordinate related to the radial distance of the trajectory of energetic particles, and is described in detail in section 2.3.1 in the next chapter. Adapted from *Olifer et al.* (2021c)

at around 2 UT on September 8, which is partially interrupted by another period of increased geomagnetic activity at 12 UT on the same day. During this recovery period, the Dst is steadily increasing (becoming less negative), accompanied by the lowering of the solar wind speed, dynamic pressure, and

IMF B_z magnitude. Importantly, during the recovery period, the radiation belt flux is replenished to levels almost an order of magnitude above the pre-storm values, creating harsher space radiation conditions around the Earth. Such substantial variations in the relativistic electron flux during geomagnetic storms naturally lead to the need for radiation mitigation for any space-based infrastructure, as the impacts of such charged particles on spacecraft may be detrimental for example as a result of deep dielectric charging and the damage acquired as a result of a discharge (e.g., *Lai*, 2012).

1.2.2 Spacecraft Charging

Trapped radiation in near-Earth space can produce serious operational problems for space-based infrastructure and electronics placed in various orbits around our planet. Such effects can often be related to spacecraft charging, which occurs when various charged particle populations interact with a satellite placed in the space plasma environment. Two main concerns for spacecraft operations in near-Earth space are surface and deep (dielectric) charging. They are caused by the low (∼10-∼100 keV) and high (∼200 keV-∼5 MeV) energy electrons respectively (e.g., *Lai*, 2012, and references therein). Both of these effects can cause operational interruptions or even catastrophic failures of satellites, resulting in social and economic losses that can be equivalent to many tens of millions of dollars. The maximum radiation levels that a satellite may withstand while continuing the nominal operations vary with its design. However, and probably not surprisingly, the probability of detecting a failure in spacecraft operations increases with the number of charged particles in the radiation belts. For example, if the daily fluence of electrons with energies above 300 keV exceeds $\sim 10^{11}$ electrons/cm^2, there is at least a 50% chance to detect the effects of deep-dielectric discharge inside the spacecraft (*Baker*, 2000). Above this fluence level, the probability quickly increases.

Spacecraft surface charging is predominantly caused by electrons with lower energies between ∼10 keV and ∼100 keV. These electrons can charge isolated surfaces of a spacecraft up to several kilovolts potential. Differential charging of different spacecraft surfaces can lead to discharges (e.g., *Baker*, 2000). They can

introduce additional noise into spacecraft systems, may interrupt their nominal operations, result in false commands, or even cause physical damage to the satellite bus (*Baker*, 2001). While such effects could be present throughout the magnetosphere, this effect has been identified as being pronounced on satellites operating at geosynchronous orbit during geomagnetic storms. Since the beginning of the space race, hundreds of spacecraft command and operational anomalies caused by surface charging have been detected.

Deep dielectric charging is caused by relativistic electrons with energies above ∼200 keV. Due to their high energies, these electrons can penetrate through satellite shielding and deposit their charge in the internal satellite systems. Various dielectric materials, like circuit boards, are especially vulnerable to charging by this radiation (e.g., *Garrett and Whittlesey*, 2000). Similar to surface charging, deep dielectric charging can cause a charge buildup inside dielectric materials (with potential differences of several kV) which typically results in an intense breakdown that can damage or even destroy circuits or other internal systems. Deep charging is prevalent in the heart of the radiation belt (at ∼3-5 R_E from the Earth, Figure 1.2) and can potentially damage satellites that are located in any trajectory between geosynchronous and low earth orbits.

The damaging effects of space radiation are typically correlated with the geomagnetic activity (*Baker*, 2000). During a geomagnetic storm, harsher radiation conditions can develop that increase deep and surface charge buildup in a spacecraft. While an informed spacecraft design remains the primary mitigation method for preventing catastrophic outcomes arising from spacecraft charging events linked to space weather, providing an accurate forecast of the radiation environment can help alleviate or reduce operational risks. This can be done by ensuring that a space mission is designed with proper radiation tolerance or by turning off non-essential spacecraft subsystems during a predicted time of increased radiation dose. However, accurate descriptions of the dominant physical processes that are responsible for driving the radiation belt dynamics, which is crucial for the creation of a robust and high-fidelity forecasting model, are still hotly debated in the research community.

This thesis addresses various aspects of radiation belt dynamics during geomagnetic storms and seeks to determine the dominant physical processes active within them to shape belt morphology. We especially focus on radiation belt dynamics during the most intense storms of the last decade, during which the electron radiation was subjected to sudden and substantial losses or accelerations, and which remain an active area of current research.

1.3 Thesis Outline

Overall, it is important to characterize near-Earth space radiation and determine the worst-case radiation levels to aid in the design of radiation-tolerant spacecraft and satellites, thus protecting humans and space-based infrastructure during space exploration. The goal of this thesis is directly related to these challenges and focuses on investigating typical and extreme radiation belt conditions and their dynamics during geomagnetic storms.

This thesis extends the study of radiation belt dynamics during geomagnetic storms, which was initiated in the *Olifer* (2019) master's thesis. The studies outlined in *Olifer* (2019) focussed on investigating geomagnetic storms with fast radiation belt losses, occurring on timescales <4 hours. Their results showed that the magnetopause shadowing loss – a type of electron radiation loss caused by fast compression of the magnetopause into the heart of the radiation belt – is likely a dominant loss mechanism that empties the radiation belt of electrons within only a few hours during the main phase of the storm. In particular, *Olifer* (2019) (as well as *Olifer et al.*, 2018, 2019) found that the dynamics of the outer magnetospheric boundary, as defined by the location of the last closed electron drift shell, are closely related to the fast radiation belt loss progression observed in various geomagnetic storms. Chapter 3 of this thesis generalizes this assessment by performing a statistical superposed epoch analysis of all geomagnetic storms observed by the NASA Van Allen Probe mission (*Mauk et al.*, 2012) between 2012 and 2019 and which contain a strong compression of the magnetopause into the inner magnetosphere. Chapter 3 identifies the typical characteristic electron radiation belt loss patterns in such storms and

further showcases similarities and repeatabilities in the characteristics of the electron losses from one event to the next. A strong similarity and repeatability of the electron loss reported in Chapter 3 can be used in the future to create an empirical model of radiation belt loss driven by magnetopause shadowing that does not rely on sophisticated and resource-expensive simulation techniques. Thus, simplifying the creation of a potential future loss forecast model. This chapter is also published in the Journal of Geophysical Research: Space Physics with the same title (*Olifer et al.*, 2021a).

Chapter 4 presents a superposed epoch analysis of all geomagnetic storms of at least moderate intensity (Dst≤ -50 nT) that occurred between the years 2012 and 2019, again using NASA Van Allen Probe data. This chapter focuses on determining typical radiation belt behavior during the recovery and radiation belt acceleration phase of a storm. Importantly, Chapter 4 shows that the electron population at energies below $\sim$800 keV is capped at almost the same level in every geomagnetic storm. This level is consistent with the theoretical model of the maximum limit to space radiation developed by *Kennel and Petschek* (1966) more than 50 years ago. This model went largely untested due to the lack of in-situ particle measurements, however, its validity was confirmed in our studies. Interestingly, ours shows that the natural limit to space radiation is reached in essentially every storm, thus, showcasing the importance of adding relevant *Kennel and Petschek* (1966) physics to any physics-based radiation belt simulation or forecast model. This chapter is also published in Geophysical Research Letters with the same title (*Olifer et al.*, 2021b).

Chapter 5 continues the examination of the influence of the Kennel-Petschek limit on radiation belt particles during the six geomagnetic storms with the largest 2.6 MeV electron flux ever recorded during the Van Allen Probe era. It shows that both relativistic and strongly relativistic particles ($\sim$100 keV-2.6 MeV) reached but never exceeded the Kennel-Petschek limit to the flux of space radiation. This finding proves that the effects of the Kennel-Petschek limit can extend up to relativistic energies and not only affect but also define the worst-case scenario electron space radiation levels around our planet. My

thesis especially demonstrates how intense the near-Earth radiation can become during geomagnetic storms, and defines worst-case requirements which can be used for designing radiation-hard satellites. Chapter 5 was accepted for publication in a form presented in this thesis in the Journal of Geophysical Research: Space Physics on August 2, 2022 (*Olifer et al.*, 2022a).

Continuing the examination of radiation belt acceleration, Chapter 6 presents a study of a very fast and intense electron radiation belt enhancement during the September 7–9, 2017 geomagnetic storm. By analyzing electron flux and phase space density (PSD), we show that inward radial diffusion is the dominant cause of the very fast acceleration observed in this event. Moreover, we show for the first time how very fast radial diffusion can mimic characteristic signatures in measured and processed data which were previously associated with local acceleration. Note that local acceleration and radiation diffusion are different and are often competing physical processes that are commonly assumed to be responsible for radiation belt acceleration. Our analysis and conclusions are made possible only through a careful analysis of the multipoint measurements by the state-of-the-art NASA Van Allen Probes mission. This study clearly highlights the importance and showcases the approach of utilizing measurements from multiple scientific satellites when analyzing fast radiation belt dynamics, especially when substantial changes occur on timescales shorter than 1 hour. Chapter 6 is published in the Geophysical Research Letters with the same title (*Olifer et al.*, 2021c).

Chapter 7 introduces for the first time approach for calculating electron PSD from electron flux data measured by a constellation of 20+ Global Positioning System (GPS) satellites. In this study, we exploit the data from the GPS constellation of satellites with unprecedented spatial and temporal resolution to assess belt dynamics in unprecedented detail. Due to the design of the energetic particle detector on-board the GPS satellites, the electron flux provided by these spacecraft is omnidirectional. However, directionality information is needed for the PSD calculation, and thus, for discriminating between the dominant physical processes that drive the overall radiation belt dynamics. Due to a large number of satellites, as compared to other missions, GPS data enables

us to resolve the radiation belt dynamics on previously unreachable minute timescales. Chapter 7 also applies the technique approach to an analysis of the August 26, 2018, geomagnetic storm. Our results clearly show that electron interactions with localized chorus plasma waves and larger scale and more global ultra-low frequency (ULF) waves are both capable of enhancing the radiation belt by orders of magnitude in much shorter bursts of acceleration than have been previously reported. Observations by other missions have been unable to determine whether acceleration progresses quasi-continuously (as is usually assumed) or in short bursts that may have different and indeed separate and distinct causes (as shown here). Importantly, our results provide a new and much higher temporal resolution view of radiation belt dynamics. This paper has been sent for review in Nature Communications but despite positive technical reviews was rejected by the editor due to its likely generation of only "specialist interest". Currently, this paper is under preparation to be submitted to an alternative discipline-specific journal (*Olifer et al.*, 2022b).

Chapter 2

Charged Particles in Earth's Magnetosphere

This chapter focuses on a mathematical description of the charged particle dynamics in a planetary magnetosphere, with a focus on the near-Earth environment. We assess the motion of particles trapped in a dipole magnetic field and derive adiabatic invariants associated with their trajectories. This chapter also introduces basic mathematical models to describe interactions between particles and various waves or magnetosphere boundaries that can impact planetary radiation belts. The equations and models of particle dynamics can also be generalized to describe other planetary or stellar magnetospheres with predominantly dipole magnetic fields. For the purposes of this thesis, this chapter acts as a short overview of various models and approaches for studying radiation belt dynamics that are utilized in the later chapters (3 through 7).

2.1 Single Particle Motion

The equation of motion of a charged particle under the influence of electric and magnetic field can be described using equation (2.1).

$$\frac{\mathrm{d}\mathbf{p}}{\mathrm{d}t} = q\left(\mathbf{E} + \mathbf{v} \times \mathbf{B}\right), \tag{2.1}$$

where $\mathbf{p}$ is the relativistic particle momentum, $\mathbf{v}$ its velocity, q its charge, and $\mathbf{E}$ and $\mathbf{B}$ are electric and magnetic fields, respectively. Particle momentum is connected to its velocity as $\mathbf{p} = \gamma m \mathbf{v}$, where γ is the Lorentz factor $\gamma =$

$1/\sqrt{1-v^2/c^2}$, m is particle mass measured in its rest frame, and c is the speed of light.

In the dipole-like magnetic field of the Earth, the charged particles complete three types of periodical motion: gyrating around a magnetic field line, bouncing along it, and drifting around the Earth. They are schematically shown in Figure 2.1. Each of these motions is periodical with different characteristic times. For example, for a relativistic 1 MeV electron located in the heart of the radiation belt, the frequency of gyration is on the order of a few kHz, the frequency of bounce motion is on the order of 1 Hz, and the drift frequency is ∼10 mHz. This section describes these three types of periodic motion and three adiabatic invariants associated with them.

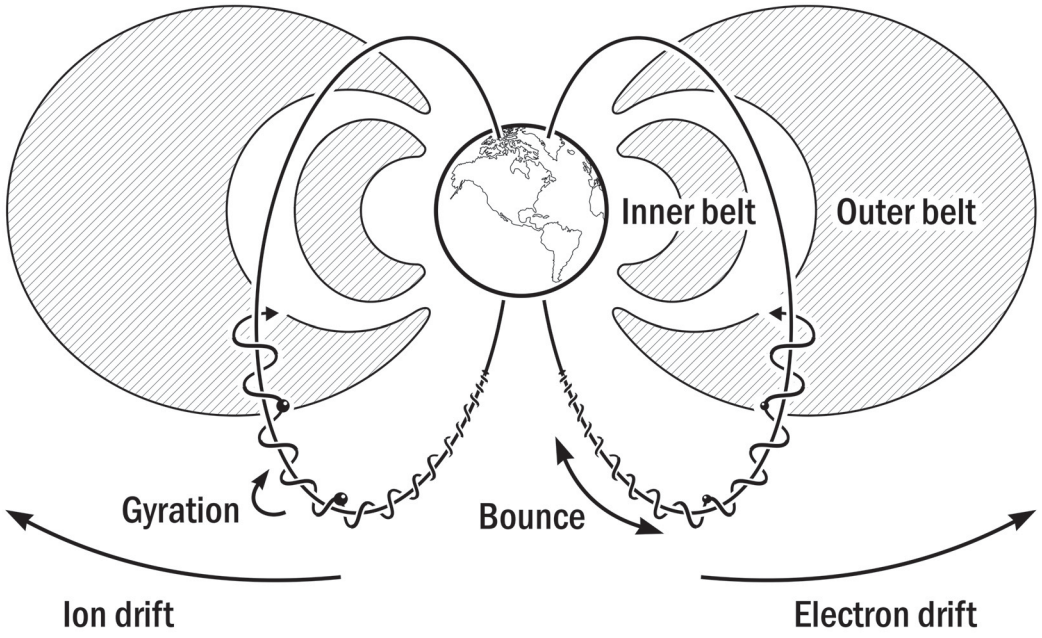

Figure 2.1: Schematic representation of the single charged particle motion in the magnetosphere of the Earth. The direction of gyration and drift is different for positively and negatively charged particles as represented in the schematic. Particles that complete these types of motion are trapped in the magnetic field and constitute the Van Allen radiation belts. Adopted from *Olifer et al.* (2021c)

2.1.1 Gyro-Motion

When a non-relativistic particle is subjected to a uniform magnetic field, and in the absence of an electric field, the equation of motion (2.1) can be transformed into the form shown in (2.2).

$$m\frac{\mathrm{d}\mathbf{v}}{\mathrm{d}t} = q\,\mathbf{v}\times\mathbf{B}. \tag{2.2}$$

It describes a helical motion with constant speed $v_{\parallel}$ along the magnetic field and a circular motion around it. The circular motion has a constant tangential speed $v_{\perp}$ and a constant angular frequency ω_c (equation 2.3). The directionality of the circular motion is determined by the sign of the charge of the particle.

$$\omega_c = \frac{qB}{m}. \tag{2.3}$$

ω_c is often called a gyro-frequency, cyclotron frequency, or Larmor frequency. For an electron, its oscillation frequency can be written as f_{ce} (Hz) $= 28\,B$ (nT). In the heart of the radiation belt, at $L = 4.5$, the dipole magnetic field strength is ∼350 nT, resulting in the electron gyro frequency of ∼9.8 kHz.

Pitch angle, α, is another important quantity that defines the helical motion of the particle and defines the angle between the particle velocity and the direction of the magnetic field. It is determined using equation (2.4) and combines circular speed, $v_{\perp}$, perpendicular to the field, and constant speed $v_{\parallel}$ along the field:

$$\tan\alpha = \frac{v_{\perp}}{v_{\parallel}}. \tag{2.4}$$

At $\alpha = 90°$, the motion of the particle is purely circular, and at $\alpha = 0°$ the particle follows the magnetic field line along a straight trajectory. Due to the properties of the Earth's magnetosphere and ionosphere, the radiation belt traps only particles with equatorial pitch angles above $\sim 5°$, and lower pitch angles are lost into the atmosphere.

According to the Hamilton-Jacobi theory, any periodic motion of a system can be associated with an adiabatic invariant J (e.g., *Landau and Lifshitz*,

1976). Under the slow changes present in that system (slow with respect to the characteristic timescales of the periodic motion), the adiabatic invariants are conserved. The general equation for an adiabatic invariant is $J_i = \oint p_i \mathrm{d}q_i$, where the integration of the canonical momentum p_i is performed over a single period for generalized coordinate q_i. In the case of the particle in a magnetic field, the equation becomes $J_i = \oint_{\Omega_i} (\mathbf{p} + q\mathbf{A}) \mathrm{d}\mathbf{l}$, where $\mathbf{A}$ is the vector potential of the magnetic field, $\mathrm{d}\mathbf{l}$ is a vector along the particle trajectory, and Ω_i denotes different types of periodic motion. For gyro-motion, the adiabatic invariant is $J_1 = \pi p_\perp^2 / Bq$. It is often called the first adiabatic invariant. It is often used in a form of equation (2.5), which is equivalent to J_1 except for constant factors, and is equivalent to the magnetic moment of the particle in the non-relativistic case. In radiation belt physics it is often given in units of MeV/G (mega electron-volts per Gauss).

$$\mu = \frac{p_\perp^2}{2mB}. \tag{2.5}$$

2.1.2 Bounce Motion

In the case of an inhomogeneous magnetic field strength along the magnetic field line, particles that complete helical motion ($\alpha < 90°$) can experience a so-called bounce motion. Due to the conservation of the first adiabatic invariant, μ, an increase in the magnitude of the magnetic field B along the trajectory of the particle causes an increase in the perpendicular component of its momentum $p_\perp$. It is associated with an increase in pitch angle until $\sin\alpha = 1$. At that point, the particle trajectory becomes purely circular which causes it to bounce back in the opposite direction along the same magnetic field line. The point along the field line where $\alpha = 90°$ is called the mirror point and its magnetic field strength is denoted as B_m. In the case of a dipole magnetic field, an approximate formula for the electron bounce period, τ_b, is given by equation (2.6) (e.g., *Walt*, 1994):

$$\tau_b = 0.117 \frac{L}{\beta} \left[1 - 0.4635 \sin^{3/4}\alpha\right], \tag{2.6}$$

where $\beta = v/c$ and α is the equatorial pitch angle. For the 1 MeV electron, trapped in the heart of the radiation belt, at $L = 4.25$, and 30° pitch angle this results in a bounce period of ∼0.4 s and thus a frequency of ∼2.5 Hz.

The second adiabatic invariant, associated with the bounce motion, only depends on the integral of the particle momentum along the magnetic field line $J_2 = \oint p_{\parallel} \mathrm{d}s$, as the magnetic flux over the negligibly small area enclosed by the bounce motion is $\oint q\mathbf{A} \cdot \mathrm{d}\mathbf{s} = q \int \mathbf{B} \cdot \mathrm{d}\mathbf{S} = 0$. By expressing $p_{\parallel}$ in terms of the total energy in the parallel component, $W_{\parallel}$, and the magnetic field energy, it is possible to transform the equation for J_2 in the form shown in equation (2.7).

$$J_2 = \oint \sqrt{2m\left(W_{\parallel} - \mu B\left(s\right)\right)} \mathrm{d}s. \tag{2.7}$$

To remove the particle momentum from the definition of the second adiabatic invariant and express it based only on field geometry, it is commonly presented in a form of $I = J_2/2p$. However, even more common is another related quantity $K = I\sqrt{B_m}$. Using this value as the second adiabatic invariant allows one to account for nonconservative I, B_m, and p when external forces (perpendicular to the magnetic field) are present (*Roederer*, 1970). Equation (2.8) shows an alternative form of the second adiabatic invariant. It is commonly given in units of $R_E \mathrm{G}^{0.5}$, where R_E is Earth radii.

$$K = \int_{B'_m}^{B''_m} \sqrt{B_m - B(s)} \mathrm{d}s, \tag{2.8}$$

where B'_m and B''_m are two mirror points along a magnetic field line.

2.1.3 Drift Motion

The third type of periodic motion, present in dipole-like magnetic fields is drift motion. It arises in the system due to the curvature of the magnetic field lines and the presence of a magnetic field strength gradient in the direction perpendicular to the field lines. These factors perturb the particle drift trajectory, causing it to change its gyro radius over the course of a single revolution. This, in turn, creates a drift of the particles in the direction perpendicular to the magnetic field lines that typically become apparent only after a substantial

number of gyro orbits. Figure 2.1 schematically shows the direction of the particle drift around the Earth, the velocity of which in general depends on particle charge and energy. Multiple space physics textbooks present a detailed description of various types of drift motion, including adiabatically perpendicular drifts which can develop for example as a result of the action of electric fields which are perpendicular to the background magnetic field. Thus, for more information, we recommend the reader to refer to the material presented in, for example, *Walt* (1994) (their Chapter 2) or *Koskinen and Kilpua* (2022) (their Chapter 2). For the dipole magnetic field, equation (2.9) (e.g., *Walt*, 1994) can be used for calculating drift period for electrons, τ_d:

$$\tau_d = 1.557 \cdot 10^4 \frac{1}{L\beta^2\gamma} \left[1 - 0.333 \sin^{0.62} \alpha\right]. \tag{2.9}$$

For the 1 MeV electron, trapped in the heart of the radiation belt, at $L = 4.25$, and 30° pitch angle this results in a drift period of ∼15 min and thus a frequency of ∼1 mHz.

Importantly, periodic drift motion is also associated with the third adiabatic invariant $J_3 = q \int \mathbf{B} \cdot \mathrm{d}\mathbf{S} = q\Phi$, where Φ is the magnetic field flux enclosed by the drift path. For the case of a dipole field $\Phi = 2\pi B_0 R_E^2/L$, where L is the distance to the trajectory of a charged particle in the magnetic equatorial plane in units of Earth radii, commonly referred to as the McIlwain L-shell (*McIlwain*, 1966) and B_0 is the mean strength of the terrestrial magnetic field at the equator. In radiation belt physics, a value L^* is usually used as the third adiabatic invariant (*Roederer*, 1970) and it is given by equation (2.10).

$$L^* = -\frac{2\pi M_0}{\Phi R_E}, \tag{2.10}$$

where $M_0 = 8.22 \cdot 10^{22}$ Am^3 is the Earth's magnetic dipole moment. Importantly, equation (2.10) is applicable to the distorted dipole magnetic field, but the L^* calculation in this case requires numerical tracing of the particle drift trajectory through a magnetic field model followed by numerical integration of the magnetic field flux through the surface enclosed by it. In the case of the dipole field, $L^* \equiv L$. In combination with μ and K, the triad (μ, K, L^*)

fully describes an unperturbed trajectory of the particle around the Earth and is commonly referred to as the adiabatic coordinates or a coordinate system based on adiabatic invariants. These adiabatic invariants are conserved as long as there are no changes in the system at the timescales of each of the periodic motions, which in the case of the terrestrial magnetosphere is typically only true during non-storm times and periods of low geomagnetic activity. During a geomagnetic storm, however, various types of electromagnetic waves are generated in the magnetosphere. Their frequency can range from a few mHz to hundreds of kHz, thus, having the possibility to resonate with each type of periodic motion, thereby violating the conservation of their respective adiabatic invariants. This property of wave-particle interactions is key to explaining the high degree of variability observed in the space radiation population in the Van Allen belts around the Earth.

2.2 Statistical Description of the Radiation Belt

The section above explained the dynamics of a single charged particle inside the Earth's magnetosphere. However, plasma that is trapped around our planet is much more appropriately described self-consistently as a collective using the concepts of statistical physics. Such a self-consistent approach is especially important for an accurate description of the electromagnetic fields that are created by the moving particles. This section focuses on introducing some statistical physics methods for describing the collective dynamics of the Earth's radiation belt plasma population and makes connections between those populations and satellite measurements.

2.2.1 Brief Overview of Statistical Theory of Plasmas

Equation (2.11) shows the differential-integral Boltzmann equation for the particle distribution function f_α for particle species α that accounts for external fields, fields generated by the plasma, and collisions between different plasma species. Here we use index α to identify the particle species (electrons or ions).

The distribution function, f_α, is normalized in such a way that its integral over the whole phase space, Ω, gives the number of all particles of that species, N_α, within it, $\int_\Omega f_\alpha(\mathbf{r},\mathbf{p},t)\mathrm{d}\mathbf{r}\mathrm{d}\mathbf{p} = N_\alpha$. An alternative normalization of the function to 1 is also common.

$$\frac{\partial f_\alpha}{\partial t} + \mathbf{v}\cdot\frac{\partial f_\alpha}{\partial \mathbf{r}} + q_\alpha\left(\mathbf{E}+\mathbf{v}\times\mathbf{B}\right)\cdot\frac{\partial f_\alpha}{\partial \mathbf{p}} = \left(\frac{\mathrm{d}f_\alpha}{\mathrm{d}t}\right)_C, \tag{2.11}$$

where $(\mathrm{d}f_\alpha/\mathrm{d}t)_C$ is a collision term which is typically a complicated function of velocity (e.g., *Koskinen and Kilpua*, 2022). Importantly, both electric and magnetic fields in the equation above obey Maxwell equations, and include both external fields as well as those generated by the plasma through charge distribution and its movement.

If the collision term $(\mathrm{d}f_\alpha/\mathrm{d}t)_C$ is zero or negligible, equation (2.11) is also called the Vlasov equation and describes the dynamics of collisionless plasma. In some collisionless systems (including radiation belts), however, it is common to use the collision term to describe the impact on the plasma from fluctuations of the background fields. In the presence of collisions between particles, it can be represented in a form of Landau collision operator $(\mathrm{d}f_\alpha/\mathrm{d}t)_C = \sum_\beta C_{\alpha\beta}$.

The solution of equation (2.11) provides the time evolution of the phase space density in a system. However, in the general case, this equation becomes extremely complicated to solve even using modern computer simulation techniques. Instead, the Boltzmann equation can be rewritten as a diffusion equation that can include wave-particle interactions or Coulomb collisions. This approach is commonly referred to as a quasi-linear theory. It describes only the slow temporal evolution of the distribution functions ignoring any non-linear effects arrising for example from large-amplitude perturbations.

The formal introduction of this quasi-linear theory is done by using a Fokker-Planck approach. In this thesis we follow the approach presented by *Walt* (1994) by introducing the probability function $\mathbb{P}(\mathbf{p}-\Delta\mathbf{p},\Delta\mathbf{p},\Delta t)$ which describes the probability of change in particle momentum $\mathbf{p}$ by $\Delta\mathbf{p}$ ($\Delta p \ll p$) over time Δt due to collisions or wave-particle interactions. In this case, the phase space density function can be represented in a form shown in equation

(2.12, e.g., *Walt*, 1994).

$$f(\mathbf{p},t) = \int \mathrm{d}^3\Delta p f(\mathbf{p}-\Delta\mathbf{p}, t-\Delta t)\mathbb{P}(\mathbf{p}-\Delta\mathbf{p},\Delta\mathbf{p},\Delta t). \tag{2.12}$$

If Δp and Δt are small, the product under the integral can be represented in the form of a Taylor series (equation 2.13), with implied summations over repeating indices (e.g., *Walt*, 1994):

$$\begin{aligned} &f(\mathbf{p}-\Delta\mathbf{p}, t-\Delta t)\mathbb{P}(\mathbf{p}-\Delta\mathbf{p},\Delta\mathbf{p},\Delta t) \\ &\quad\approx \left(1-\Delta t\frac{\partial}{\partial t}-\Delta p_i\frac{\partial}{\partial p_i}+\frac{1}{2}\Delta p_i\Delta p_j\frac{\partial^2}{\partial p_i\partial p_j}\right)\times f(\mathbf{p},t)\mathbb{P}(\mathbf{p},\Delta\mathbf{p},\Delta t) \end{aligned} \tag{2.13}$$

The Fokker-Planck equation can be obtained by substituting (2.13) into (2.12) and introducing the notation of an average of an arbitrary function g as $\langle g\rangle \equiv \frac{1}{\Delta t}\int \mathrm{d}^3\Delta p g(\Delta\mathbf{p})\mathbb{P}(\mathbf{p},\Delta\mathbf{p},\Delta t)$ results in equation (2.14).

$$\frac{\partial f}{\partial t} = -\frac{\partial}{\partial p_i}\langle\Delta p_i\rangle f + \frac{1}{2}\frac{\partial^2}{\partial p_i\partial p_j}\langle\Delta p_i\Delta p_j\rangle f. \tag{2.14}$$

The first coefficient $\langle\Delta p_i\rangle$ is commonly referred to as a drag coefficient and is responsible for the acceleration or deceleration of particles due to collisions. The second coefficient $\langle\Delta p_i\Delta p_j\rangle/2$ is called the diffusion coefficient with a common notation D_{ij}. Equation (2.14) can be further expressed in a diffusion form:

$$\frac{\partial f}{\partial t} = \frac{\partial}{\partial p_i}\left(D_{ij}\frac{\partial f}{\partial p_j}\right) \tag{2.15}$$

As is described in the next section, in the physics of the radiation belts it is common to use the triad of the adiabatic invariants as the coordinates for the phase space density instead of the location and momentum phase space. In this case, equation (2.15) can be rewritten in a form (2.16, e.g., *Walt*, 1994).

$$\frac{\partial f(\mu,K,\Phi)}{\partial t} = \frac{\partial}{\partial x_i}\left(D_{ij}\frac{\partial f(\mu,K,\Phi)}{\partial x_j}\right), \tag{2.16}$$

where x_i designates one of the adiabatic invariants μ, K, and Φ. This equation is commonly used as a basis for radiation belt models as it can describe the evolution of the particle distribution function due to the violation of three adiabatic invariants, which often occurs under the influence of plasma waves of different frequencies that are present in the magnetosphere. Importantly, and as mentioned above, this quasi-linear theory is only valid for small changes occurring over long periods of time and the limits of its applicability to radiation belt dynamics under a range of conditions are still not fully understood.

2.2.2 Particle Fluxes and Distributions

Until now, this chapter presented the description of plasma in terms of a phase space density (PSD) $f(\mathbf{r}, \mathbf{p}, t)$ or $f(\mu, K, \Phi)$. However, the actual particle measurements of the space plasma are often made in terms of particle flux $j(W, \alpha, L, t)$. Particle flux, or more strictly a differential directional flux, is a measure of the number of particles that cross a unit of area per second, from a specific direction, and at a specific energy. In radiation belt physics it is commonly given in units of $\mathrm{cm}^{-2}\mathrm{s}^{-1}\mathrm{sr}^{-1}\mathrm{keV}^{-1}$. The flux is typically a derived quantity from the number of counts per second measured in-situ by a spacecraft-based particle detector. These counts are usually processed by the spacecraft mission team, taking into account the design of the detector, providing the differential directional flux as a function of energy, pitch angle, location, and time. However, as described above, the quasi-linear theory typically used to address radiation belt dynamics is based on solving diffusion equations for the particle phase space density rather than flux. The connection between flux and PSD can be easily found by postulating that the number of particles that cross an area, $\mathrm{d}A$, per unit time in terms of flux (equation 2.17) and in terms of PSD (equation 2.18) is the same (e.g., *Walt*, 1994).

$$\mathrm{d}N = j(W, \alpha)\,\mathrm{d}A\,\mathrm{d}\Omega\,\mathrm{d}W = j\,\mathrm{d}x\,\mathrm{d}y\,\mathrm{d}\Omega\,\frac{p}{m}\mathrm{d}p. \tag{2.17}$$

$$\mathrm{d}N = f\,\mathrm{d}x\,\mathrm{d}y\,\mathrm{d}z\,\mathrm{d}p_x\,\mathrm{d}p_y\,\mathrm{d}p_z = f\,\mathrm{d}x\,\mathrm{d}y\,vp^2\,\mathrm{d}\Omega\,\mathrm{d}p. \tag{2.18}$$

Equating equations (2.17) and (2.18) provides a simple relation between flux and PSD:

$$f(\mathbf{r}, \mathbf{p}) = \frac{j(W, \alpha)}{p^2}. \tag{2.19}$$

While straightforward, providing the PSD as a function of three adiabatic invariants, $f(\mu, K, L^*)$, which is useful for determining the driving physical processes that are responsible for radiation belt dynamics, requires additional, often numerical, processing. In particular, by studying the evolution of $f(\mu, K, L^*)$ it is possible to investigate which adiabatic invariant is violated, if any, and to draw conclusions about the relative impact of various disturbances in the magnetosphere in driving radiation belt dynamics. Often, electromagnetic waves act as the main cause of the observed radiation belt dynamics as a result of the violation of one or more adiabatic invariants.

2.3 Wave-Particle Interactions

The equations presented in Sections 2.1 and 2.2 above are valid for describing the dynamics of any charged particle species trapped in any planetary magnetosphere with a dipole-like magnetic field. In this section, however, we focus on applying the main results from the earlier sections to the electron radiation belts around the Earth. A relativistic electron trapped in the heart of the terrestrial Van Allen belt completes the three types of periodic motion over three different characteristic times ($\sim$0.1-1 ms for gyration, 1 s for bounce, and $\sim$10 min for drift). Therefore, in the presence of electromagnetic waves with periods close to the periods of these periodic particle motions, the conservation of the associated adiabatic invariants can be violated. In Earth's magnetosphere, there are multiple wave species with different frequencies that may drive the radiation belt dynamics. They range from very-low-frequency (VLF) whistler mode chorus waves with frequencies of a few kHz to ultra-low frequency (ULF) waves with frequencies of a few mHz. Under their influence, radiation belt electrons can be lost or accelerated to relativistic or even ultra-relativistic energies over the course of a geomagnetic storm.

2.3.1 Ultra-Low Frequency (ULF) Wave Radial Diffusion

In space physics, ULF waves are pulsations in the electromagnetic field with frequencies from approximately 2 mHz to 0.2 Hz (e.g., *Elkington and Sarris*, 2016). These are not to be confused with the radio communication ULF waves that according to the International Telecommunication Union designation have frequencies from 0.3 kHz to 3 kHz. ULF waves in the magnetosphere of the Earth can be excited by a range of large-scale phenomena in the magnetosphere, for example, due to the action of the Kelvin–Helmholtz instability at the magnetopause that can penetrate ULF waves which propagate into the magnetospheric cavity (e.g., *Kivelson*, 1995). Importantly, the frequency of these ULF waves is similar to the frequency of the drift motion for relativistic electrons inside the Van Allen belt. Thus, in the presence of the ULF waves, the third adiabatic invariant of relativistic electrons may not be conserved. However, because the ULF frequencies are much lower than those of gyro and bounce motion, the first and second invariants are still conserved.

Under these circumstances, the diffusion equation (2.16) can be simplified by only keeping the terms associated with the violation of the third adiabatic invariant. Equation (2.20) shows the final form of the electron diffusion equation where the third adiabatic invariant is presented in terms of L, which is equivalent to L^* for the case of a dipole field (e.g., *Walt*, 1994).

$$\frac{\partial f}{\partial t} = L^2 \frac{\partial}{\partial L}\left(\frac{D_{LL}}{L^2}\frac{\partial f}{\partial L}\right), \tag{2.20}$$

where D_{LL} is often called the radial diffusion coefficient and can be characterized using the wave power in the ULF band.

Importantly, equation (2.20) describes the diffusion of particles across different L-shells or when cast in terms of L^* across different L^*. Depending on the sign of the PSD gradient, $\partial f/\partial L$, the particles can diffuse inwards or outwards. Typically, the outward diffusion is observed during the main phase of a storm, when radiation belt electrons are lost. Particles can be diffused outwards to the edges of the magnetosphere and be subsequently

lost at the magnetopause by a process known as magnetopause shadowing (e.g., *Turner et al.*, 2012). The inward diffusion dominates during the recovery phase when the new source population, injected at high L^*, is transported inward to replenish the radiation belt. The inward diffusion is also associated with electron acceleration. Due to the conservation of the first adiabatic invariant, particle energy increases when it is transported into regions with higher magnetic field, as is the case with inward radial diffusion.

Chapters 3, 6, and 7 of this thesis present statistical and case studies addressing the importance of radial diffusion in driving the dynamics of Earth's radiation belts. By analyzing the measured electron fluxes and derived PSD as a function of three adiabatic invariants, as well as performing radial diffusion simulations using equation (2.20), we show that the radial diffusion process is often a dominant factor in driving storm-time radiation belt dynamics.

2.3.2 Pitch Angle and Energy Diffusion

Higher frequency waves can cause a violation of the first and/or second adiabatic invariants of radiation belt electrons. Some examples of these waves include plasmaspheric hiss whistler mode chorus waves, and signals from man-made VLF transmitters. Notably, electromagnetic ion cyclotron (EMIC) waves, while having frequencies between ∼0.2-5 Hz, can also violate the first adiabatic invariant once the effects of the Dopler shift from the parallel motion of the electron along the field are taken into account (e.g., *Usanova and Mann*, 2016). The evolution of electron PSD under the influence of these waves can be presented in the form of equation (2.21), commonly used for the radiation belt simulations (e.g., *Koskinen and Kilpua*, 2022, and references therein).

$$\frac{\partial f}{\partial t} = \frac{1}{p \sin\alpha} \frac{\partial}{\partial \alpha} \sin\alpha \left(D_{\alpha\alpha} \frac{1}{p} \frac{\partial f}{\partial \alpha} + D_{\alpha p} \frac{\partial f}{\partial p} \right) + \frac{1}{p^2} \frac{\partial}{\partial p} p^2 \left(D_{p\alpha} \frac{1}{p} \frac{\partial f}{\partial \alpha} + D_{pp} \frac{\partial f}{\partial p} \right). \tag{2.21}$$

This form of equation (2.16) allows for an easier calculation of diffusion coefficients $D_{\alpha\alpha}$, $D_{p\alpha}$, and D_{pp}, which depend on the wave activity in a respective frequency band. Under the influence of these waves, the electrons can be

lost into the atmosphere through the diffusion of particles towards the lower pitch angles during the main phase of a storm, or be accelerated during the recovery phase.

2.3.3 Maximum Limit on Trapped Flux

An interesting outcome arising from the competition between the excitation of electron cyclotron plasma waves and pitch angle diffusion and subsequent atmospheric loss induced by chorus waves was discovered by *Kennel and Petschek* (1966). In their paper, *Kennel and Petschek* (1966) showed that whistler mode chorus waves can be generated by an absolute instability arising in the system due to the temperature anisotropy of electron distributions in the directions parallel and perpendicular to the magnetic field (typically when $T_\perp > T_\parallel$). Moreover, the intensity of the chorus waves is higher in the system with larger anisotropy and larger particle flux. However, in the presence of whistler waves, pitch angle diffusion of particles also occurs resulting in the electron distribution becoming more isotropic and driving enhanced losses by transporting particles into the loss cone. Based on this property, *Kennel and Petschek* (1966) have postulated that an upper limit to the electron population exists, beyond which any increase in the electron flux results in a generation of more intense chorus waves, which in turn cause this new population to diffuse towards lower pitch angles and precipitate into the atmosphere. In the literature, the level at which the electron population self-limits itself in this way is known as the Kennel-Petschek (KP) limit. In this thesis, we follow an improved KP theory developed by *Mauk and Fox* (2010) which applies to relativistic and non-relativistic energies and which presents the analysis in terms of differential flux, as opposed to the integral flux used by *Kennel and Petschek* (1966). Note that the following equations are presented in CGS units, consist with the work by *Mauk and Fox* (2010), meanwhile, the remainder of this thesis flows SI unit convention.

According to the KP theory, the electron population is limited when any losses of whistler wave amplitude, caused by ionospheric reflections of these waves, are balanced out by subsequent wave growth of the reflected wave

and where the growth rate of whistler-mode waves directly depends on the temperature anisotropy and the flux of the particle distribution. Following *Mauk and Fox* (2010), we start our introduction of the KP theory by estimating the gain G of whistler wave amplitudes when they pass through the magnetic equator in equation (2.22).

$$G \approx \exp\left\{\int_{-D/2}^{D/2} \frac{\gamma}{V_g} \mathrm{d}s\right\} = \exp\left\{\frac{\gamma}{V_g} D\right\}, \tag{2.22}$$

where D is the total distance along the magnetic field line, γ is the temporal wave growth rate associated with the absolute instability, V_g is the wave group speed and $\mathrm{d}s$ is the infinitesimally small distance along the magnetic field line. Typically, the length D is roughly estimated as $R_E \cdot L$.

If R is the ionospheric reflection coefficient for wave amplitudes, the KP theory is defined by the condition $R \cdot G = 1$. By assuming that $R = 0.05$ and applying the condition above, equation (2.22) can be rewritten in a form of equation 5.1:

$$\gamma(j(W, \alpha)) \approx \frac{3 V_g(\omega(W_r))}{L R_E}, \tag{2.23}$$

where $\ln G = \ln 1/R \approx 3$, and we explicitly state that the wave growth depends on differential directional electron flux $j(W, \alpha)$ meanwhile the group speed V_g depends on wave frequency at a resonant energy W_r. Thus, equation (5.1) defines conditions for the KP limit at various energies. By calculating γ and V_g for different resonant energies and wave frequencies, it is possible to find the electron differential flux j that satisfies condition (5.1) and thus represents the limiting KP flux. As assessed by *Mauk and Fox* (2010), V_g can be estimated using equation (2.24):

$$V_g = \frac{2c^2 k \omega_c \left(1 - \omega/\omega_c\right)^2}{\omega_{pe}^2 + 2\omega_c \omega \left(1 - \omega/\omega_c\right)^2}, \tag{2.24}$$

where k is the wavenumber and ω_{pe} is plasma frequency ($\omega_{pe} = \sqrt{4\pi n e^2/m_e}$).

Calculating the temporal wave growth rate γ involves solving a set of rather long and complicated equations. Following *Mauk and Fox* (2010) (whose

calculation relies on theoretical estimations by *Summers et al.* (2009) and *Xiao et al.* (1998)), γ can be calculated using equations (2.25-2.27).

$$\gamma = \pi\omega_{pe}^2\eta\left(A - \frac{\omega}{\omega_c - \omega}\right)\left[2\omega + \frac{\omega_{pe}^2\omega_c}{(\omega - \omega_c)^2}\right]^{-1}, \tag{2.25}$$

where η is the fraction of the energetic electron distribution near cyclotron resonance (equation 2.26).

$$\eta = \frac{\pi m_e(\omega - \omega_c)}{n_e k}\int_0^\infty \mathrm{d}p_\perp \frac{p_\perp^2}{\Delta_R}\left(\frac{\partial f}{\partial p_\perp}\right)_{p_\parallel = p_R}, \tag{2.26}$$

where $p_R = m_e(\gamma_R\omega - \omega_c)/k$ is the parallel momentum for resonant particles with γ_R denoting the Lorentz factor, $\Delta_R = 1 - \omega p_R/m_e c^2 k\gamma_R$, and f is electron phase pace density in ($p_\parallel$, $p_\perp$) coordinates.

A is relativistic distribution pitch angle anisotropy factor (equation 2.27):

$$A = \frac{k}{m_e(\omega - \omega_c)}\left[\int_0^\infty \mathrm{d}p_\perp \frac{p_\perp^2}{\gamma_R\Delta_R}\left(p_\perp\frac{\partial f}{\partial p_\parallel} - p_\parallel\frac{\partial f}{\partial p_\perp}\right)_{p_\parallel = p_R}\right]\times \left[\int_0^\infty \mathrm{d}p_\perp \frac{p_\perp^2}{\Delta_R}\left(\frac{\partial f}{\partial p_\perp}\right)_{p_\parallel = p_R}\right]^{-1}. \tag{2.27}$$

The distribution function f, as well as the electron flux $j = fp^2$, that satisfies equation (5.1) defines the KP limit at a particular time and location in the radiation belt of the Earth as a function of resonant particle energy. Plasma density and background magnetic field can change during the course of a storm resulting in changes in related plasma and electron cyclotron frequencies. Therefore, the resulting KP limit can vary based on these changes. Notably, however, the variation of the KP limit from storm to storm is rather small, as we show later in this thesis (Chapters 4 and 5), introducing the concept that there can be a maximum electron flux in the radiation belts as a result of the action of the KP process.

Chapter 3

On the Similarity and Repeatability of Fast Radiation Belt Loss: Role of the Last Closed Drift Shell

Based on *Olifer et al.* (2021a) On the similarity and repeatability of fast radiation belt loss: Role of the last closed drift shell, *Journal of Geophysical Research: Space Physics*, 126 (11), doi:10.1029/2021ja029957. The paper was reformated to fit thesis formatting guidelines without any changes to its content.

Properly characterising fast relativistic electron losses in the terrestrial Van Allen belts remains a significant challenge for accurately simulating their dynamics. In particular, magnetopause shadowing losses can deplete the radiation belt within hours or even minutes, but can have long-lasting impacts on the subsequent belt dynamics. By statistically analyzing seven years of data from the entire Van Allen Probes mission in the context of the last closed drift shell, here we show how these losses are much more organized and predictable than previously thought. Once magnetic storm electron dynamics are properly analyzed in terms of the location of the last closed drift shell, not only is the loss shown to be repeatable but its energy-dependent spatio-temporal evolution is also revealed to follow a very similar pattern from storm to storm. Employing an energy-dependent ULF wave radial diffusion model, we further show for the first time how the similar and repeatable fractional loss of the pre-storm

electron population in each storm can be reproduced and explained. Empirical characterisation of this loss may open a pathway towards improved radiation belt specification and forecast models. This is especially important since underestimates of loss can also create unrealistic sources in models, creating phantom electron radiation and leading to the prediction of an overly harsh radiation environment.

3.1 Introduction

Since the discovery of the Earth's Van Allen radiation belts over 50 years ago (*Van Allen and Frank*, 1959), determining the physical processes responsible for their dynamics have been a major focus of space physics research (e.g., *Friedel et al.*, 2002). The dynamics of the trapped relativistic electron population with energies from hundreds of kilo electronvolts (∼100 keV) to millions of electronvolts (∼1 MeV) during geomagnetic storms is of particular interest because of their potential impact on satellite electronics through deep-dielectric charging (*Baker et al.*, 1994). Electrons can be lost at the beginning of the storm before the subsequent acceleration of a source population to MeV energies, which can partially or completely replace those which are lost, in some cases creating radiation orders of magnitude stronger than that which existed pre-storm (e.g., *Reeves et al.*, 2003). In particular, interaction with high-frequency plasma waves, such as chorus (e.g., *Shprits et al.*, 2007; *Lee et al.*, 2013), electromagnetic ion cyclotron (EMIC) (e.g., *Ukhorskiy et al.*, 2010; *Usanova et al.*, 2014), or plasmaspheric hiss (e.g., *Thorne et al.*, 1973) waves, can cause loss into the atmosphere. Meanwhile, ultra-low frequency (ULF) plasma waves (*Mann et al.*, 2016) can cause particles to be transported outwards to the last closed drift shell (LCDS) and lost at the magnetopause into the solar wind in a process known as magnetopause shadowing (e.g., *Turner et al.*, 2012; *Olifer et al.*, 2018). The relative importance of these processes continues to be hotly debated (*Shprits et al.*, 2018; *Mann et al.*, 2018). This chapter, in particular, focuses on investigating whether the LCDS dynamics can explain the fast magnetopause shadowing losses.

Recent studies have shown that a compression of the outer magnetospheric boundary can cause intense electron radiation belt losses occurring on very short (<1 day) timescales. For example, *Olifer et al.* (2018) showed that the LCDS location of the Van Allen belt electrons and its dynamics can explain rapid and intense dropouts of relativistic electrons in some of the most intense geomagnetic storms of the last decade. It is also interesting to investigate on a statistical basis whether a substantial compression of the magnetopause, characterized by inward motion of the LCDS, can cause a radiation belt dropout in every storm and whether the response is repeatable and/or predictable. In this research, we perform a statistical superposed epoch analysis of 69 events which contain rapid and deep magnetopause compressions and reveal how outward radial transport to the compressed magnetopause is the dominant cause of rapid particle depletions in the heart of the Van Allen radiation belt for such storms. Our results also reveal for the first time a remarkable repeatability and indeed similar radiation belt response to such solar wind forcing.

3.2 Results

Recent event-specific studies of radiation belt dropouts (e.g., *Turner et al.*, 2012; *Olifer et al.*, 2018; *Tu et al.*, 2019; *Ozeke et al.*, 2020, and references therein) commonly associate the electron loss with the rapid compression of the last closed drift shell (LCDS) into the heart of the radiation belt. In particular, such studies reveal, using in-situ observational data and radiation belt modeling, that the dropouts in some storm events are caused by magnetopause shadowing loss enhanced by outward radial diffusion and not by precipitation into the atmosphere. Here, we extend these studies by statistically studying the effects of the LCDS compression. We select events with a single isolated intense compression of the LCDS below the L^* value of 5.8 over the course of six days. Notably, the threshold value of 5.8 was selected to obtain the largest number of isolated events with strong magnetopause compression whilst removing any impacts from compound events. For the purposes of this study, we analyze the LCDS dynamics during the entirety of the Van Allen Probes mission

(September 2012 until July 2019) and select 69 isolated events with a single LCDS compression. We calculate the location of the LCDS using the neural network LANL* code (*Yu et al.*, 2012) which allows for fast detection of the times with singular LCDS compression. Once the low LCDS events have been identified, accurate L^* locations of the LCDS are then determined using the full calculation by the LANLGeoMag library (*Henderson et al.*, 2017) for every storm (Supplementary Figure E.1). By superposing the selected events with respect to the minimum LCDS in each event, we analyze the median radiation belt response to the LCDS compression and its variability. The list of selected events is shown in Appendix A.

3.2.1 Overview of the Storms

Figure 3.1 shows the superposed epoch analysis of selected solar wind conditions and geomagnetic indices for these 69 isolated events. Panels a through f show the mean value across different storms in red, median value in black, and upper and lower quartiles in gray as a function of the superposed epoch time in units of days. The bottom panel g shows the median spin-averaged electron flux in the 2.6 MeV channel as a function of the superposed epoch and L^* parameter (*Roederer*, 1970). In this research, the solar wind data were taken from the Qin-Denton dataset provided by the Energetic Particle, Composition, and Thermal Plasma (RBSP-ECT) team (*Spence et al.*, 2013) and the radiation belt flux measurements data were taken from both Van Allen Probes A and B for both of the REPT (*Baker et al.*, 2012) and MagEIS (*Blake et al.*, 2013) instruments. Notably, 66 of the selected 69 events can be considered geomagnetic storms of weak to severe intensity (Dst < -30 nT) according to the typical storm classification by *Loewe and Prölss* (1997). The three remaining events, the May 2015 (minimum Dst $= -28$ nT), the July 2016 (minimum Dst $= -23$ nT) and the June 2019 (minimum Dst $= -17$ nT), still contained a substantial compression of the LCDS (minimum values of 5.5, 5.3, and 5.4 in L^*, respectively) and due to the low value of the LCDS are retained in the statistical analysis.

Figure 3.1g shows that the selected low LCDS events display clear signs of

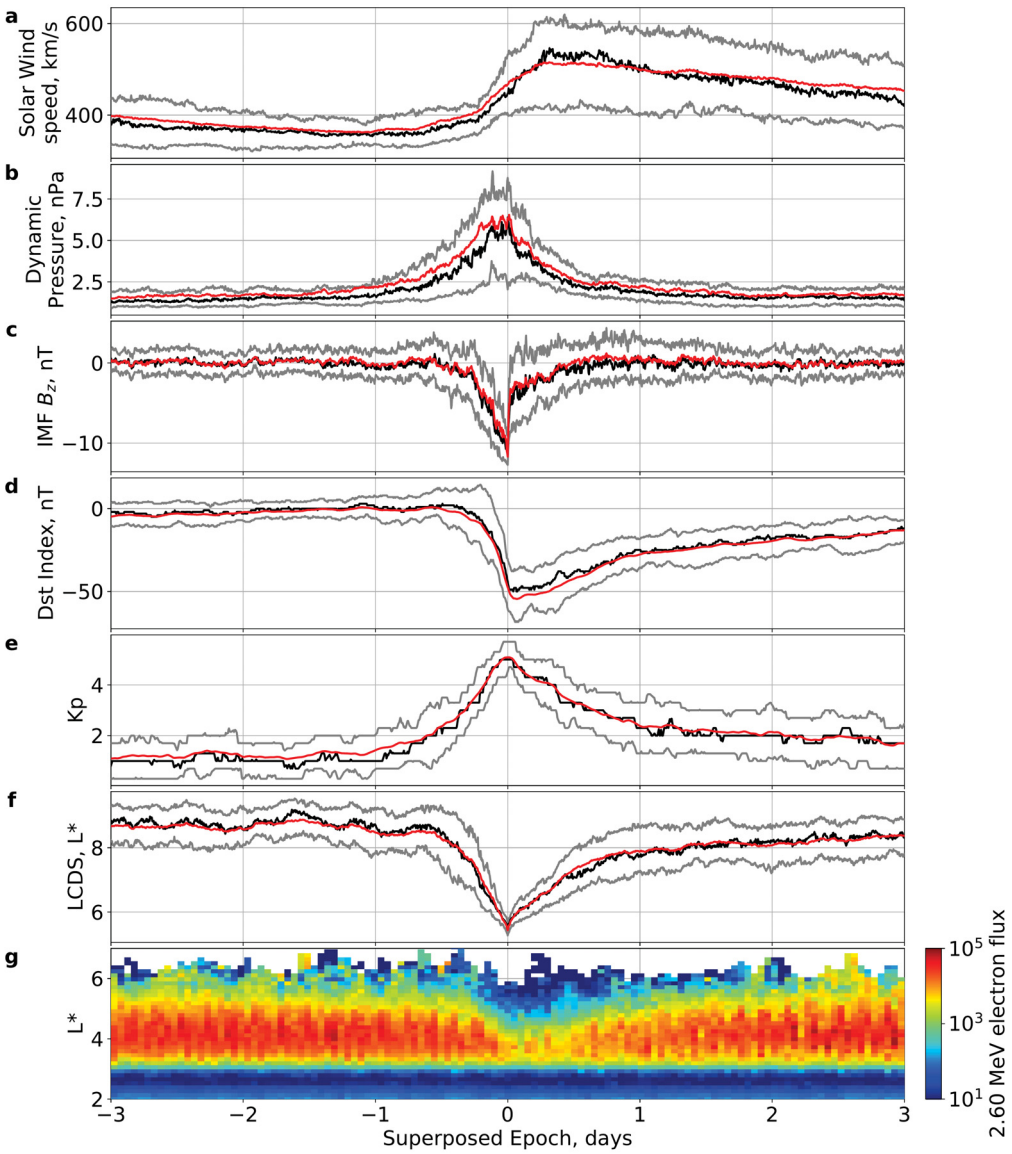

Figure 3.1: Superposed epoch analysis of selected solar wind parameters, geomagnetic indices, and radiation belt response for the selected geomagnetic storm events. a, solar wind speed; b, dynamic pressure; c, southward component of the interplanetary magnetic field (IMF); d, geomagnetic storm-time disturbance index (Dst); e, planetary Kp activity index; f, L^* of the last closed drift shell (LCDS); g, median 2.6 MeV spin-averaged electron flux in units of $\mathrm{cm}^{-2}\mathrm{s}^{-1}\mathrm{sr}^{-1}\mathrm{MeV}^{-1}$. For panels a through f, the mean value across all events is shown with the red line, with the black line and two gray lines representing the median value and the lower and upper quartiles, respectively.

fast radiation belt losses, with maximum depletion occurring within half a day and reaching relatively low L^* regions of $L^*\approx4$ well inside the envelope of the LCDS (Figure 3.1f). These fluxes are reduced by almost an order of magnitude relative to the pre-storm levels (cf., Figure 3.3). To further analyze the radiation belt dynamics and determine the dominant mechanism that causes such rapid and intense loss we perform similar superposed epoch analysis for multiple energy channels from both REPT and MagEIS instruments. However, because different energies and L^*, as well as different storms, have different pre-storm electron flux levels it is beneficial to perform superposed epoch analysis of the relative flux change, with respect to the pre-storm levels.

Figure 3.2 shows the results from a superposed epoch analysis of the fractional flux loss, with different energies shown in different panels. Note that the color scale is the same for the different energies and represents the fraction of the flux changes with respect to the pre-storm level. The yellow color represents no changes with respect to the pre-storm flux, and it is the dominant color on the left side of each panel until half a day before the minimum of the LCDS (zero epoch). This result shows that the pre-storm flux in the selected events is a stable population suitable for subsequent loss analysis. The loss across all panels in Figure 3.2 is represented by the color change from yellow through green to blue. This loss happens earlier for higher L^* regions and later for lower L^*, but occurs with approximately the same timescale across all energy channels. Meanwhile, the normalized minimum flux level reached during the loss period is lower for higher energies. This indicates that all of the energies react at the same time, starting on the higher L^* regions and with the loss propagating inward, but with a loss intensity which increases with energy. On the other hand, the recovery for different energies differs strongly in both intensity and timescale with the lower energies recovering earlier and reaching stronger intensities as compared to the pre-storm flux.

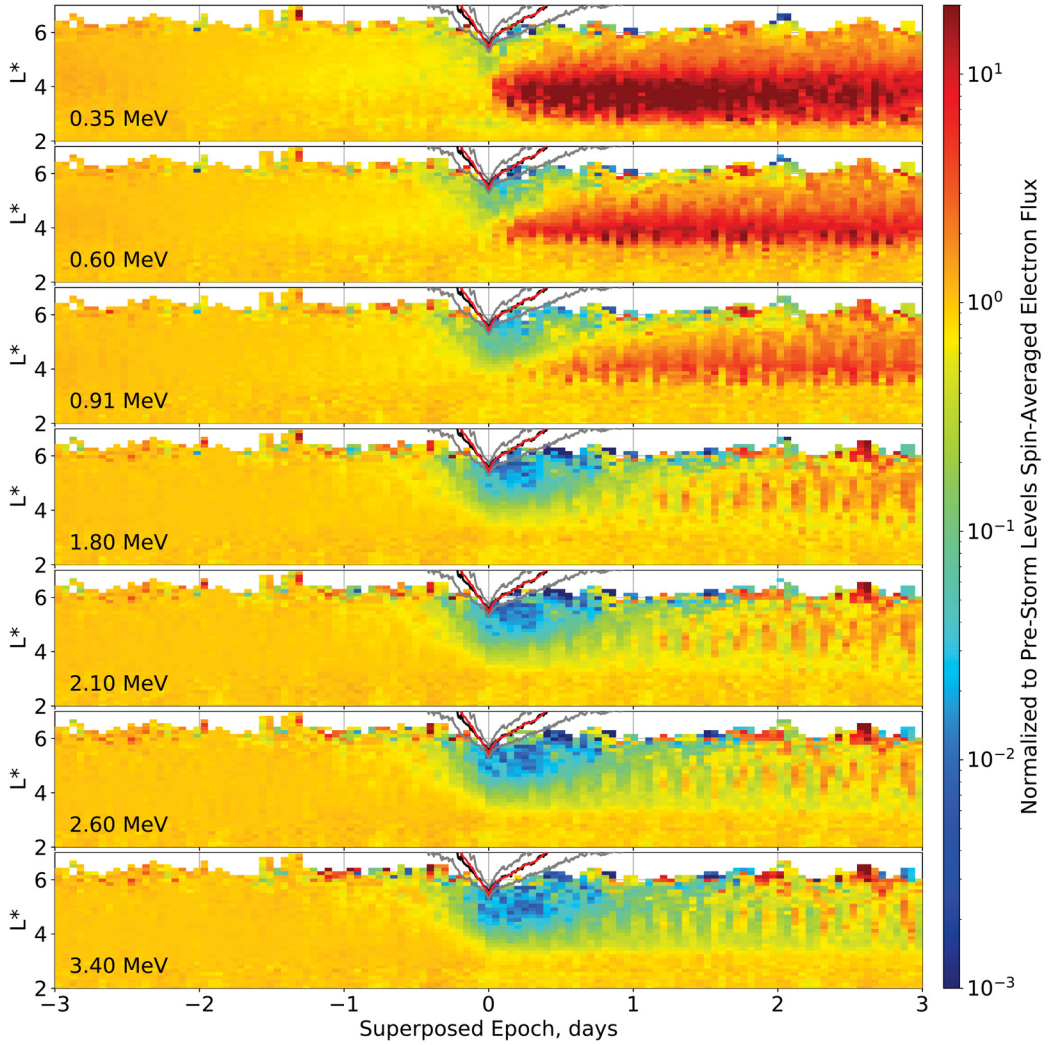

Figure 3.2: Superposed epoch analysis of the normalized spin-averaged electron flux. Different panels represent different energies that are shown on the bottom left corner of each panel. The color scheme in each panel is the same and represents the median relative change of the flux with respect to the pre-storm levels as a function of L^* and superposed epoch days. Electron flux data was taken from both MagEIS and REPT instruments on board both the Van Allen Probes A and B. The mean L^* value of the last closed drift shell across all events is shown with the red line, the black line and two gray lines show the median value and the lower and upper quartiles respectively.

3.2.2 Similarity and Repeatability of the Radiation Belt Loss

To further investigate the loss dynamics and the self-similarity between the storm events, we analyze the evolution of the fractional reduction of the pre-storm flux at a fixed L^* as a function of superposed epoch time. To assess any potentially competing adiabatic effects on the observed flux at fixed energy we also analyze the fractional changes in superposed epoch phase space density (PSD) at fixed first and second adiabatic invariants at the same fixed L^*. Figure 3.3 shows examples of these fixed L^* superposed epoch time series at L^*=4.25 with flux plotted in the panels in the left column and PSD plotted in the right columns. Different energies (left) and first adiabatic invariants (right) are plotted in different rows. In each row, the first adiabatic invariant value on the right corresponds to the energy value on the left at L^*=4.25 at the superposed epoch time zero. The median normalized values are shown with black dots and the upper and lower quartiles are represented by the error bars. Such a representation of the flux and PSD dynamics provides an unexpected but extremely important result about the Van Allen belt loss dynamics during intense magnetic storms. The panels in the left column of Figure 3.3 show that the fractional loss in electron flux is extremely self-similar from one storm to the next. This feature is clearly represented by the small separation between the upper and lower quartiles, which indicates the low level of variability between the different storms during the dropout. Notably, the size of the error bars, representative of the separation between the quartiles, in normalized flux sharply increases from being a factor of three at most up to end of the loss phase, to approximately two orders of magnitude during the recovery. In addition, during the pre-storm phase (up to 3 days before the minimum of the LCDS), the error bars remain small across all energies which indicates that the pre-storm phase of the selected storms is mostly quiet with no significant additional loss processes. Overall, the left column of Figure 3.3 shows that the temporal profile of the fractional loss of pre-existing radiation belt electrons follows almost exactly the same time profile during the period of

loss, independent of the magnitude of the pre-storm flux. Rather unexpectedly the flux evolves such that the relative amount of the particle loss in each event is the same, and depends only on the electron energy and L^*.

Similar behavior is seen in the right panel of Figure 3.3 for the observed evolution of the normalized median PSD and the respective 25% and 75% quartiles. The same observation in PSD demonstrates that the observed changes in flux represent genuine losses and are not explained purely by adiabatic effects, but rather by the LCDS reaching low L^*. It is also interesting to note that the variability of both flux and PSD during the acceleration phase remains symmetrical around the median for all studied energies and first adiabatic invariants. In addition to that, the final median value of the flux of more energetic ($\geq$1.8 MeV) electrons which are reached at the end of the acceleration phase is close to the pre-storm level. A natural interpretation of this result is that the level of flux recovery is strongly dependent on the solar wind conditions and the availability of the new source populations with the same probability for flux recovery to reach above or below the pre-storm flux. This result is in good agreement with the analysis of *Reeves et al.* (2003) where they reported that the properties of the >2 MeV post-storm flux at geosynchronous orbit was almost equally likely to have increased or decreased compared to the pre-storm level.

To further analyze the dynamics of the radiation belt during the dropout we perform a quantitative analysis of the timing and intensity of the loss by fitting a two-sided Gaussian to the L^*= *const* flux and PSD profiles. This approach provides a quantitative method of analyzing loss dynamics. A detailed description is presented in the Appendix B. The two-sided Gaussian fits are shown for both flux and PSD in Figure 3.3 with red lines. The estimated intensity of the loss from the fit as characterized by the ratio of the pre-storm flux to minimum flux, J_{PS}/J_{min} (f_{PS}/f_{min}), is shown in the bottom left corner in each panel. To confirm the self-similarity of the fractional loss of pre-existing radiation belt flux, we analyze 12 different energy channels from the REPT and MagEIS instruments between energies of 0.5 MeV and 4.2 MeV and at 14 different fixed L^* values between 3.75 and 5.57. Figure 3.4 shows a summary

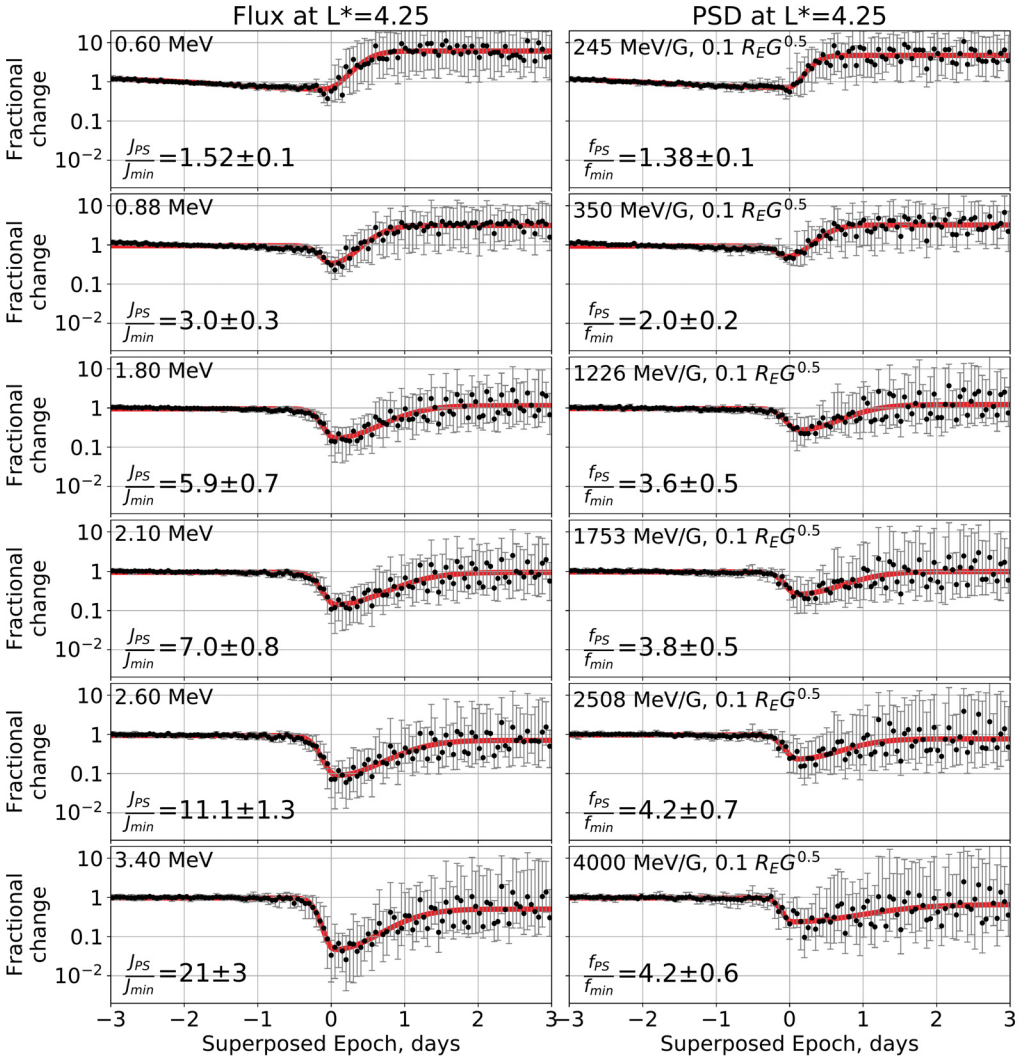

Figure 3.3: Storm-time evolution of the fractional change of electron flux (left) and phase space density (right) at fixed L^*. The left column shows the fractional change of the spin-averaged electron flux with respect to the pre-storm levels at fixed L^*=4.25, with different fixed energies in different rows. The right column shows the fractional change of the electron phase space density (PSD) at fixed first adiabatic invariants at fixed L^*=4.25 and for fixed second adiabatic invariant of K =0.1 $R_E G^{1/2}$. Different first adiabatic invariants are shown in different rows. Note that the first adiabatic invariants shown on the right correspond to the energy channel on the left at the end of the loss phase for the selected L^* and K. Energy and invariant values are shown in the top left corner of every panel. The median values are shown with black dots and the upper and lower quartiles are represented with error bars. Additionally, each panel shows a two-sided Gaussian fit to the data plotted with a red line, and with the maximum loss intensity defined in the bottom left corner of each panel.

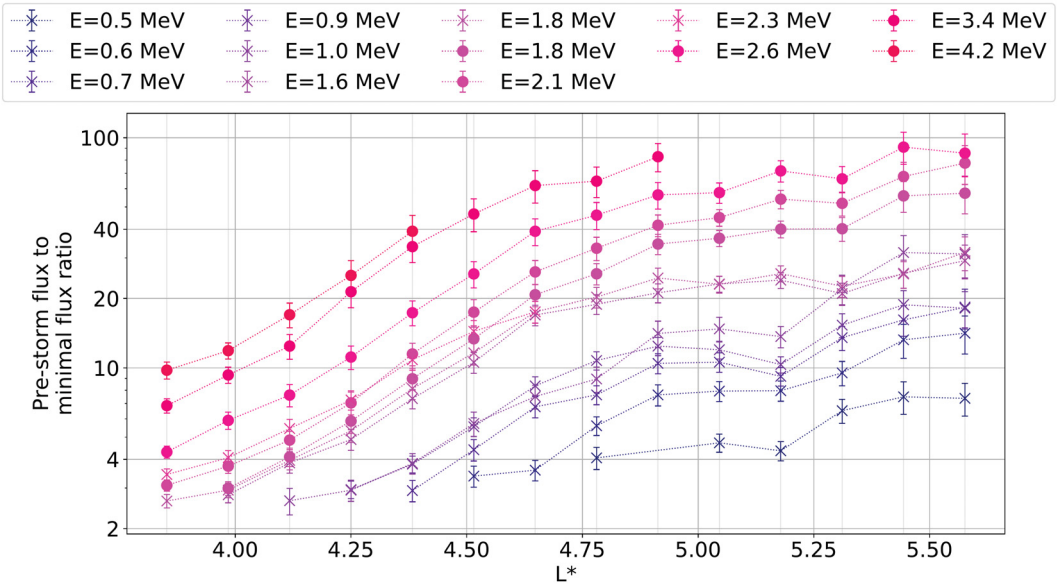

Figure 3.4: The intensity of the fractional flux loss for different energies and L^* locations in the Van Allen radiation belt. Different energies are shown in different colors with data from the MagEIS instrument marked with an "x" and data from the REPT instrument with a circle. The error bars were obtained from the least-squares numerical fitting of the fractional flux loss with a two-sided Gaussian.

of the loss intensity, or by how much the pre-storm flux is larger than the minimum flux reached during the loss, for these fixed energies as a function of L^*. Different energies are shown in different colors and the error bars represent uncertainties in the loss intensity, obtained from the numerical least-squares fitting of the two-sided Gaussian profiles.

Figure 3.4 shows a remarkably clear structuring of the loss intensity in both energy and L^*. First, it shows that the loss is more intense at higher L^*. For different energy channels, the loss at L^*=5.5 is ∼30 times larger than at L^*=4.0 reaching values as large as ∼100 for the highest energies. The magnitude of this loss during low LCDS events is approximately an order of magnitude more intense than has been reported in some previous superposed epoch studies (*Morley et al.*, 2010; *Murphy et al.*, 2018; *Turner et al.*, 2019). Second, the fractional loss is very clearly much more significant at higher energies. For example, the loss of the 3.4 MeV population is an order of magnitude more intense than that at 0.6 MeV, across all values of L^*. In combination with the

L^* dependence, it creates a remarkably well-organized picture of a self-similar and repeatable loss profile in energy-L^* space. Moreover, the relatively small and non-overlapping error bars confirm that this structure repeats from one storm to the next. It shows that even though the initial pre-storm fluxes can differ significantly in magnitude from storm to storm, the relative change during the loss phase is very well-behaved and described by the repeatable pattern shown in Figure 3.4. Our discovery of substantial repeatability during radiation belt losses that occur during the LCDS compression has the potential to play a decisive role in the development of improvements to the accuracy of physics-based radiation belt specification and forecast models.

Supplementary Figure E.2 shows a similar plot to Figure 3.4 but calculated for PSD. Very similar structuring is also present in the PSD data with the higher losses being observed at higher first adiabatic invariants, and higher L^*. Notably, the intensities of the dropouts in PSD are somewhat smaller than those measured in flux at fixed corresponding energies. This proves that the flux decreases are not caused only by adiabatic processes alone, but represent genuine repeatability of loss profiles associated with magnetopause shadowing, as shown below.

3.2.3 Probing the Origin of the Similarity and Repeatability of the Loss

The superposed epoch analysis performed in this chapter allows for an extensive investigation of the role of the compressed LCDS in driving losses in the heart of the Van Allen radiation belt, even at $L^*<5$. In particular, it is interesting to investigate how the energy and L^* dependence of the loss intensity (Figure 3.4) might be explained by outward radial diffusion to a compressed LCDS. The role of this process in radiation belt depletion has been examined in computer simulations in a number of recent case-studies (*Hudson et al.*, 2014, 2015; *Mann et al.*, 2016; *Ozeke et al.*, 2019; *Tu et al.*, 2019; *Wang et al.*, 2020; *Ozeke et al.*, 2020). These studies have already concluded that magnetopause shadowing, perhaps enhanced by ULF wave outward radial diffusion, can explain the losses at $L^*>5$. However, the discussion of whether the losses at lower L-shells ($L^*<5$)

can be explained in terms of ULF wave enhanced magnetopause shadowing still continues (*Shprits et al.*, 2018; *Mann et al.*, 2018). Here, we use our observations to investigate the signatures of the loss as defined by its timing, intensity, and location, and assess whether such an outward radial transport model can explain the repeatable characteristics of the observed dropouts.

Figure 3.5 presents the L^* dependence of the timing of the flux loss as characterized by the time of the beginning of the loss, and the epoch of the minimum flux relative to the time of minimum LCDS at epoch time zero for different energies in the same format as Figure 3.4. It shows that the loss starts earlier at higher L^* and propagates inward, with lower L^* being affected later. Meanwhile, different energies are affected at the same time at fixed L^*. Such behavior is consistent with the radial diffusion paradigm where the particles at the higher L^* are affected and see loss effects earlier as they are transported outward to the more proximal magnetopause. The data from the highest L^*=5.57 observed by the Van Allen Probes in the statistics reported here shows that the loss starts half a day before the time that the minimum of the LCDS is reached. Interestingly, this is the same time as the median LCDS typically starts to move inward (c.f., Figure 3.1). In addition, Figure 3.5 also shows that the losses stop simultaneously for all energies and L^* at the time of superposed epoch $\sim$0.047$\pm$0.003 days, very close to the time at which the LCDS reaches its minimum L^* location. These results show that the timing of the energy-independent loss is controlled by the dynamics of the magnetopause as defined by the LCDS location. This is very strong evidence that outward radial diffusion and magnetopause shadowing are likely the dominant cause of the observed losses.

To describe the global behavior and trends in the PSD evolution we analyze a statistical PSD which is calculated from the statistically well-behaved median flux dynamics. It is important, as the data of the superposed epoch PSD has limited L^* coverage (Supplementary Figure E.3) and a larger deviation from the median (Figure 3.2), suggesting that additional variability in PSD profiles is introduced by the magnetic field model used to convert flux to PSD. The detailed description of this transformation is provided in the Appendix B.

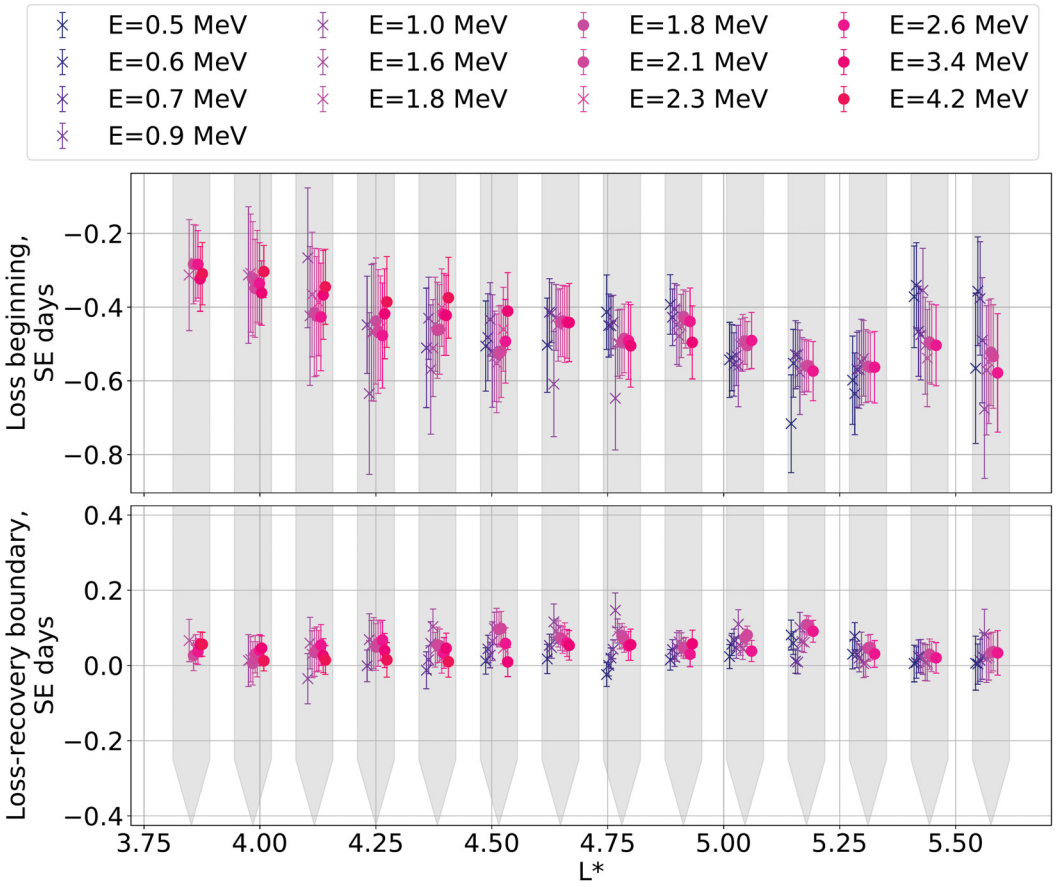

Figure 3.5: Fractional flux loss timescales. The top panel shows the time before the minimum last closed drift shell (LCDS) when the dropout starts for different energies and L^*. The value of this time when the loss begins was obtained from the two-sided Gaussian fitting as described in the Appendix B. The bottom panel shows the time inferred as the end of the loss phase based on the fit, as compared to the epoch time zero at the time of the minimum L^* location of the LCDS. This time also marks the beginning of the recovery. For both panels, different energies are shown in a different color with data from the MagEIS instrument marked with an "x" and data from the REPT instrument with a circle. Also, the timings at fixed L^*, shown by the gray shadowing point on the x-axis, are grouped into the shaded regions and are spread out L^* for the convenience of the reader. The actual L^* value obtained from the analysis corresponds to the center of each bin and is represented in the bottom panel by where the shadowing reaches the x-axis.

Figure 3.6 shows the resulting PSD profiles as a function of L^* for different fixed first adiabatic invariants, μ. Each fixed μ is shown in different rows, with L^* PSD profiles at different times shown in a different color. This statistical PSD is determined from the median flux using a superposed epoch *Tsyganenko and Sitnov* (2005) magnetic field model at the location of the spacecraft, assuming that the spin averaged flux from Figure 3.2 is representative of the flux at a local pitch angle of 90°.

The PSD dynamics in Figure 3.6 again point to outward transport to the compressed LCDS as the dominant cause of the radiation belt depletion. The PSD profiles in the left column show that the population of particles is gradually depleted with time across a wider and wider range of L^*, which causes the profiles to monotonically decrease in magnitude outwards towards the LCDS and with a gradient in L^* which gets steeper with time. Meanwhile, the right column shows that the normalized relative loss in PSD at each L^* is well-behaved and starts earlier and is larger at higher L^*. The same result was already noted for the median flux and median PSD in Figure 3.4 and Supplementary Figure E.2, respectively. Note also that the PSD profiles become more structured in L^* as the epoch approaches the time of the minimum LCDS. For example, the largest PSD fluctuations away from a monotonic profile of PSD decreasing with L^* are present for PSD traces at superposed epoch time zero (brown line in Figure 3.6). According to Figure 3.1f, 75% of all events contain LCDS below L^*=5.8 at epoch time zero with the lowest LCDS reaching L^*=4.3. Hence, such fluctuations away from a monotonic PSD profile as a function of L^* are representative of cases that may have the LCDS inside the L^* domain.

To explain the energy dependence of the dropout intensity in terms of a radial diffusion model we turn to an analysis of the temporal evolution of the PSD profiles as a function of L^*. We use the PSD data calculated for every analyzed storm to determine how fast the electron population at different μ and L^* for fixed K =0.1 $R_E G^{1/2}$ are transported outwards and compare it to that expected based on a model for outwards ULF wave radial diffusion to the LCDS. In particular, we assess the normalized outward transport rate,

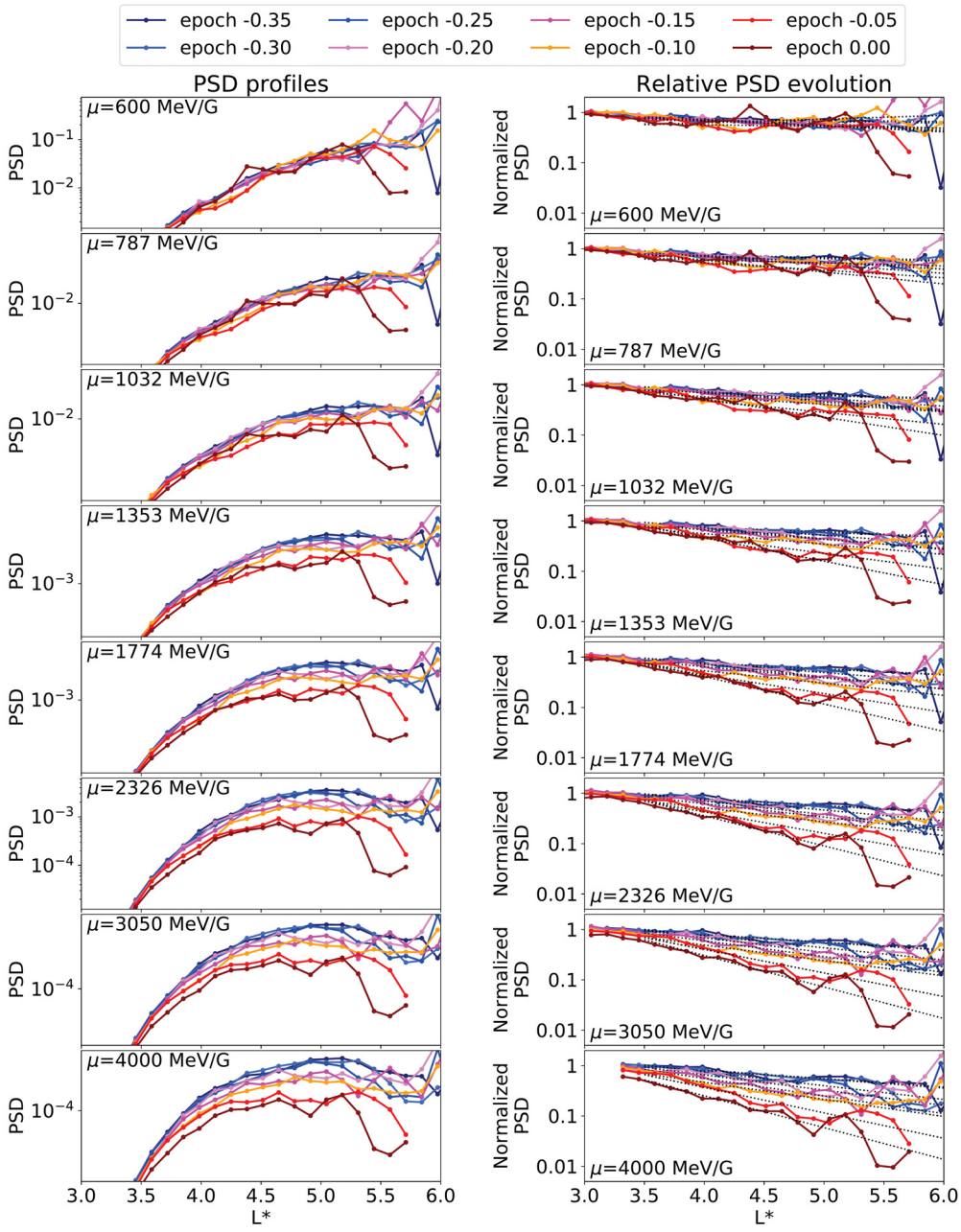

Figure 3.6: Evolution of the phase space density (PSD) profiles. The PSD profiles calculated from the median superposed epoch flux (left column) and their relative change with respect to the pre-storm levels at each L^* (right column) for fixed μ at different epochs in advance of the epoch time zero of minimum LCDS. Different rows show data for different values of the first adiabatic invariant, μ, with different epochs shown in a different color according to the legend on the top of the figure. The right column additionally shows a linear fit to the logarithm of the relative PSD losses as a function of L^* used for the PSD profiles calculations (see text for details).

$\dot{L}$ in units of L^*/day, that combines both PSD gradients and outward radial diffusion coefficients, D_{LL}, in one equation (defined by *Schulz and Lanzerotti* (1974)):

$$\dot{L} = -D_{LL} \left(\frac{\partial \ln f}{\partial L} \right)_{\mu,K}, \tag{3.1}$$

where L is the L^*-shell, D_{LL} is the radial diffusion coefficient in units of L^{*2}/day, f is the PSD, K is the second adiabatic invariant, and the dot represents the time derivative. Radial diffusion coefficients were obtained from the Kp-parametrization in *Ozeke et al.* (2014). The gradients of the PSD in log-space are calculated for every individual storm from every inboud or outbound pass of the Van Allen Probes. Then, the superposed epoch transport rates are determined in the similar way as the superposed epoch flux (see Results section above and the Appendix B). Figure 3.7 shows the outward radial transport rate $\dot{L}$ as a function of L^* and superposed epoch days, with different panels showing different fixed first adiabatic invariants, μ. Note that in computing the $\dot{L}$ rates in Figure 3.7 we used the L^* dependence of PSD from the Van Allen Probe data, but used an assumed equivalence between dipole L and L^* in equation (3.1) and in the (*Ozeke et al.*, 2014) D_{LL}.

Figure 3.7 shows that there is a clear structuring of the radial transport rates in μ-L^* space, consistent with the structuring observed in the loss intensity of the flux as a function of energy and L^* (Figure 3.4). Figure 3.7 confirms that populations with different energies (that are equivalent to different μ) are being transported outward with different rates even at the same L^* because of the dynamical development of energy-dependent PSD gradients. Figure 3.7 also demonstrates that the maxima of the PSD profiles for a constant μ moves inward with time, consistent with outward radial diffusion driving the loss. Such behavior is of course associated with the appearance of the outward gradients with $\dot{L}L^{-1} > 0$ at lower L^* at later times during the loss phase as clearly demonstrated in Figure 3.7. Significantly, our analysis shows how the energy dependence of the loss can be explained by only utilizing the outward radial diffusion paradigm. The energy dependence of the loss is often used to

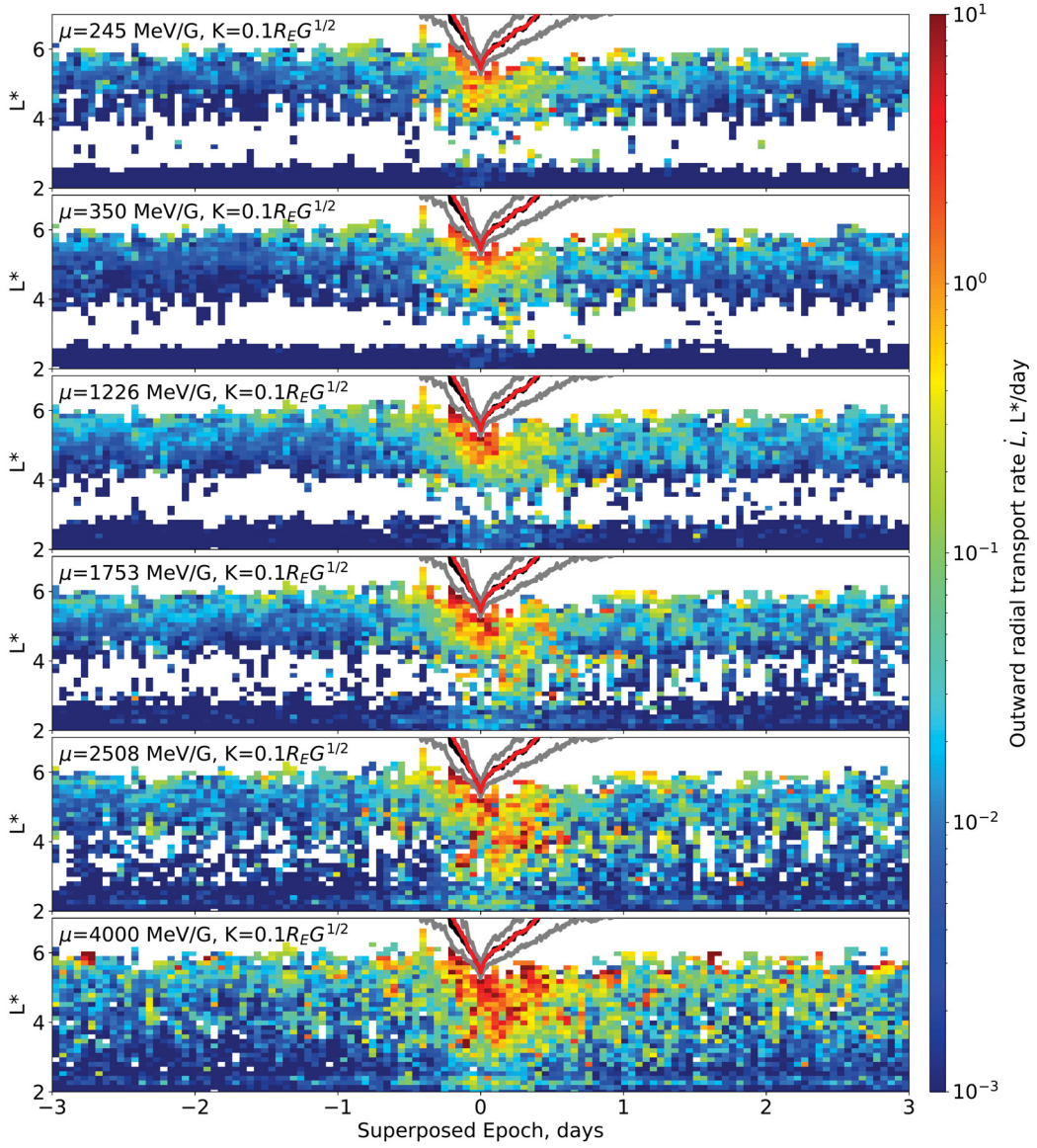

Figure 3.7: Outward radial transport rate, $\dot{L}$. Median superposed epoch outward radial transport rates in units of L^*/day with different first adiabatic invariants, μ, shown in different panels as a function of L^* and superposed epoch. All data present is calculated for the second adiabatic invariant K =0.1 $R_E G^{1/2}$ using *Tsyganenko and Sitnov* (2005) magnetic field model. The mean L^* value of the last closed drift shell across all events is shown with the red line, the black line and two gray lines show the median value and the lower and upper quartiles respectively.

argue in favor of plasma wave-particle scattering into the loss cone. However, our results show that the energy dependence of the loss shown here can instead be naturally explained by outward radial diffusion to a compressed LCDS.

3.3 Discussion and Conclusions

In this chapter, we assess the dynamics of Van Allen radiation belt losses observed during magnetic storms in which the LCDS penetrated to relatively low L^* ($L^* \leq 5.8$). In contrast to some previous superposed epoch studies, where the median flux loss ranged from a factor of 2 to 10 with respect to the pre-storm levels, our results show that low LCDS-related losses can generate much stronger losses and deplete the Van Allen belt electron fluxes by up to two orders of magnitude, depending on energy and L^*. For example, recent results presented by *Turner et al.* (2019) show rapid losses happening over a half-a-day period but with much smaller statistically averaged magnitudes, their median electron flux at most only decreasing by an order of magnitude. Similarly, results by *Murphy et al.* (2018) suggest that total radiation belt content for the relativistic electron population (>0.5 MeV) decreases at most by a factor of 4. This suggests that the classical approach of assessing losses in storms selected using the storm-time disturbance index Dst (or its proxy SYM-H) statistically underestimate the strength of extreme losses.

We show for the first time strong evidence for the repeatability and indeed similarity and repeatability in the characteristics of rapid and strong radiation belt dropouts during intense magnetopause shadowing events. The fractional flux change with respect to the pre-storm levels during the loss is effectively statistically almost identical across the assessed events, differing only with energy and location and independent of pre-storm flux. The self-similarity is confirmed by small deviations in individual storms from the superposed epoch median fractional flux loss and quantified by studying the variability in fractional loss using the quartiles of the observed distribution. Notably, the pre-storm flux levels in the selected storms span approximately two or three orders of magnitude, depending on energy. However, the observed fractional

loss of flux is effectively almost the same (within a factor of approximately 3 between the quartiles) from storm to storm when the LCDS reaches low L^* (here using storms when the minimum LCDS is at $L^* \leq 5.8$). To our knowledge, this is the only study to date that presents such self-similar behavior of the radiation belt electron loss. The self-organisation and repeatability of the loss we show here can be contrasted with previous descriptions of a relative unpredictability of belt response and which is usually attributed to a delicate balance between acceleration and loss processes (e.g., *Reeves et al.*, 2003). Instead, our results show that the magnitude of the losses is in fact rather predictable and repeatable, once examined in terms of the LCDS location as shown previously in four case studies by *Olifer et al.* (2018).

Moreover, we can also explain the dynamical evolution of losses in the heart of the belt ($L^* < 5$) in terms of outward radial transport and particle loss to the LCDS. Analysis of the PSD profiles reveals that the loss is associated with monotonic gradients in PSD which get steeper with time, with losses at high L^* happening first across the L^* range between 3 and 6, with more intense losses happening for higher L^* and μ. This result is equivalent to that obtained for the electron flux, where a very clear structuring of the loss intensity as a function of energy and L^* also exists (c.f., Figure 3.4). The L^* dependence of the loss is caused by the strong power-law dependence of the diffusion coefficients on L-shell (*Brautigam and Albert*, 2000; *Ozeke et al.*, 2014; *Olifer et al.*, 2019), with an energy dependence developing as a result of the radial transport rates in the radial diffusion model depending on the radial PSD gradients at fixed first adiabatic invariants, and thus different energies at fixed L^*.

An important aspect of the observed dynamics is the preference for faster losses to develop at higher μ. How can this be explained by outward radial diffusion? The answer is that the impacts of the magnetopause shadowing are experienced more quickly per unit time at higher μ, as a result of the energy dependence of the electron drift. Just inside the LCDS, higher μ particles have more interactions with the magnetopause per unit time, such that the drift-averaged rate of loss per unit time is larger for higher μ. As a result, the

rate of inward propagation of the loss (equation (3.1)) develops a μ dependence (and an energy dependence at fixed L^*) due to the faster evolving $\partial f/\partial L$ at higher μ at the outer boundary at the LCDS, even if the radial diffusion coefficient, D_{LL}, inside the LCDS is independent of energy at fixed L^*. In other words, the relevant time step for establishing a drift-averaged radial gradient at the LCDS at the outer boundary of the belt, $\frac{\partial f}{\partial L}\big|_{L^*=LCDS}$, is the drift time of the electrons and that is shorter for higher μ.

The resulting self-organization of radiation belt loss under the action of radial diffusion from low L^* to the LCDS acts across a wide range of energies larger than $\sim$0.3 MeV. However, this model may also be able to explain why there is no apparent loss for the lower energies below $\sim$0.3 MeV as well, except in the L^* regions which actually lie outside the LCDS. The drift time of such particles, on relatively high L^* close to the LCDS, is >1 hour; for example, a 150 keV electron at L =6 has a drift period of one hour. As shown in Figure 3.1, although the LCDS penetrates to low L^* below 5.8 in every storm included in our statistics, it does not stay at low L^* for very long. For example, around 75 % of the storms have the LCDS below L^*=6 for <6 hours. For electron energies with drift times on the order of this LCDS penetration timescale, drift-arranged losses and hence the gradients of $\frac{\partial f}{\partial L}\big|_{\mu,L^*=LCDS}$ are quite likely to be smaller. The PSD profiles at these energies do not have enough time to develop strong outward gradients in such cases at the LCDS. Therefore, the outward radial diffusion losses for that population would be expected to be rather slow. Moreover, the electron populations below 300 keV are known to be rapidly replenished at the very beginning of the storm from new source population available from the plasmasheet (e.g., *Jaynes et al.*, 2015; *Reeves et al.*, 2016, and references therein). Such rapid recovery appears to be able to overcome any losses developing at the LCDS. Thus, the only losses for those particles would exist in the domain of direct magnetopause shadowing outside the LCDS, and only at L^* locations where the particle drift time allows the entire drift shell to be emptied during the period of LCDS compression at the magnetopause.

Interestingly, the observed self-similarity of the belt dynamics does not

extend into the recovery and acceleration phase. At that time, flux increases as it is partially or completely replenished, varying by orders of magnitude from storm to storm. This suggests a strong variability of this phase that is being controlled by the availability of the source population, as suggested for example by *Jaynes et al.* (2015), as well as by the strength of the acceleration process itself. Such behavior in the recovery phase is of course also similar to the results presented by *Reeves et al.* (2003) where they suggest, based on geosynchronous observations, that the recovery of the multi-MeV electron population is highly sensitive to the storm conditions and can vary from storm to storm by orders of magnitude. Additionally, the results we present in our Figure 3.3 nicely agree with the results of *Reeves et al.* (2003) where they showed that the MeV electron population usually recovers to levels with an equal probability of being above or below pre-storm levels, depending on the storm.

Overall, our study demonstrates that once characterized in terms of the dynamics of the last closed drift shell, the fast loss of Van Allen belt electrons can not only be explained but also to a large degree predicted as a function of energy and L^*. The processes that are responsible for the loss of electrons can be explained in terms of direct magnetopause shadowing at the LCDS, as well as at lower L^* due to radial diffusion to the compressed magnetopause. This creates a self-organizing system that affects Van Allen belt electron losses in exactly the same manner from storm to storm. The discovery reported here that the fractional flux loss is essentially identical once LCDS dynamics are examined represents a significant advance towards more accurate physics-based radiation belt specification and forecast models. It promises a relatively simple method of defining the electron population which remains at the end of the loss phase in any storm since it appears that the extent of the loss of the pre-storm population can be defined by a factor that depends on energy and L^* and which are connected clearly and repeatably to LCDS dynamics. All radiation belt models consist of the superposition of processes that result in the transport, acceleration, and loss of electrons within the simulation domain. When losses are incorrectly specified in these models, errors will develop either due to the transport and acceleration of phantom particles which should have

been lost or due to an under-representation of flux levels of some populations due to unrealistic extreme losses. Consequently, a more accurate specification of the energy and L^* dependent loss processes using approaches based on the importance of the LCDS dynamics reported here offers an important advance towards significantly improved radiation belt specification and forecast capabilities.

Chapter 4

A Tale of Two Radiation Belts: The Energy-Dependence of Self-Limiting Electron Space Radiation

Based on *Olifer et al.* (2021b) A tale of two radiation belts: The energy-dependence of self-limiting electron space radiation, *Geophysical Research Letters*, 48 (20), doi:10.1029/2021gl095779. The paper was reformated to fit thesis formatting guidelines without any changes to its content.

The flux of energetic electrons in the terrestrial Van Allen belts varies by orders of magnitude during a magnetic storm. Here, we show how the dynamics of these electrons are clearly separated by energy into two distinct populations which are governed by different storm-time behavior. We reveal how self-limiting processes, described theoretically by Kennel and Petschek (1966), govern the energy-dependent dynamics of the electrons. For terrestrial magnetic storms, accelerated electrons with energies below ∼850 keV quickly reach a maximum energy-dependent differential flux level which is almost the same in every storm. Higher energy electrons typically do not reach a limiting flux and instead are governed by the differential impacts of competing acceleration and loss mechanisms. In general, electron fluxes saturate at the Kennel-Petschek limit first at lower energies, impacting higher energies later in the storm. For the most intense storms, the maximum energy at which the fluxes are capped can

also increase.

4.1 Introduction

Despite renewed recent attention, how the physical processes that are active in geospace combine to produce the observed dynamics of the Earth's electron radiation belts remains elusive (e.g., *Li and Hudson*, 2019; *Millan and Thorne*, 2007, and references therein). With increasing appreciation of disruptive or even potentially catastrophic impacts of this space radiation on an ever growing number of satellites (e.g., *Baker et al.*, 1987; *Baker*, 2001; *Reeves*, 2007), the research area is also one of increasing societal importance. The NASA Van Allen Probes mission (*Fox and Burch*, 2014) has provided a unique long-duration data set of unprecedented fidelity with which to probe the elusive processes which control the harshness of this space environment. Here, we statistically show for the first time how self-limiting processes appear to couple the acceleration and loss of a vast portion of the electron population trapped around the Earth, thus generating a remarkable natural limit for electron space radiation.

Specifically, in this letter we show that acceleration and loss associated with chorus wave-particle interactions are strongly coupled in the way theoretically predicted by *Kennel and Petschek* (1966) more than 50 years ago. At lower energies, ∼50-850 keV, the Kennel-Petschek process generates a natural limit to the maximum electron flux in every geomagnetic storm investigated here. Meanwhile, higher energy electrons (>∼850 keV) remain relatively unaffected by the Kennel-Petschek (KP) limit and instead reach varying levels of flux as a result of the differing but often delicate balance between acceleration and loss. The results of this letter clearly show that any experimental or modeling study of the radiation belt dynamics should be performed within the framework of the Kennel-Petschek theory.

4.2 Overview of the Superposed Epoch Analysis

We analyze 70 isolated storms with at least moderate geomagnetic activity (Dst≤ -50 nT) over the course of the entire Van Allen Probes era. The list of events used in this study is presented in Appendix A. The selected storms contain a single decrease of Dst≤ -50 nT over the course of a six-day interval. Such selection allows us to investigate the dynamics of the radiation belt during a typical magnetic storm, whilst removing any impacts in the superposition which arise from compound events. A superposed epoch analysis of the solar wind parameters, resulting Dst index, and the location of last closed drift shell (LCDS) aligned by minimum Dst in each storm are shown in Figure 4.1a-e.

Figure 4.1f-h presents the median response of the superposed epoch flux of the relativistic radiation belt electrons as a function of energy, L^* (*Roederer*, 1970), and superposed epoch again aligned by minimum Dst. Figure 4.1f reveals distinctly different electron dynamics at higher and lower energy at a fixed $L^*= 4.25$. The lower energy electrons ($E <\sim 850$ keV) are quickly accelerated after epoch time zero, rapidly reaching median flux levels almost two orders of magnitude larger than the pre-storm conditions. The higher energy electrons ($E >\sim 850$ keV) are instead rapidly lost from the radiation belt prior to their subsequent recovery to pre-storm levels. Figure 4.1g,h confirm this assessment, and show rapid acceleration of the lower energy population occurs across a wide range of L^* encapsulating the entire outer belt; meanwhile, the loss of the higher energy population is confined to regions above $L^*\approx 3.5$. These dropouts are commonly associated with the magnetopause shadowing losses (e.g., *Turner et al.*, 2012; *Turner and Ukhorskiy*, 2020; *Xiang et al.*, 2017, 2018; *Olifer et al.*, 2018). A similar median radiation belt response was revealed in prior superposed epoch studies. For example, *Turner et al.* (2015); *Bingham et al.* (2018); *Turner et al.* (2019) showed a similar rapid energization of the lower energetic electrons at the beginning of the storm, and the presence of the dropouts prior to recovery for the higher energy particles – results similar to those reported by *Li et al.* (2015) for electrons with energies >1 MeV. These

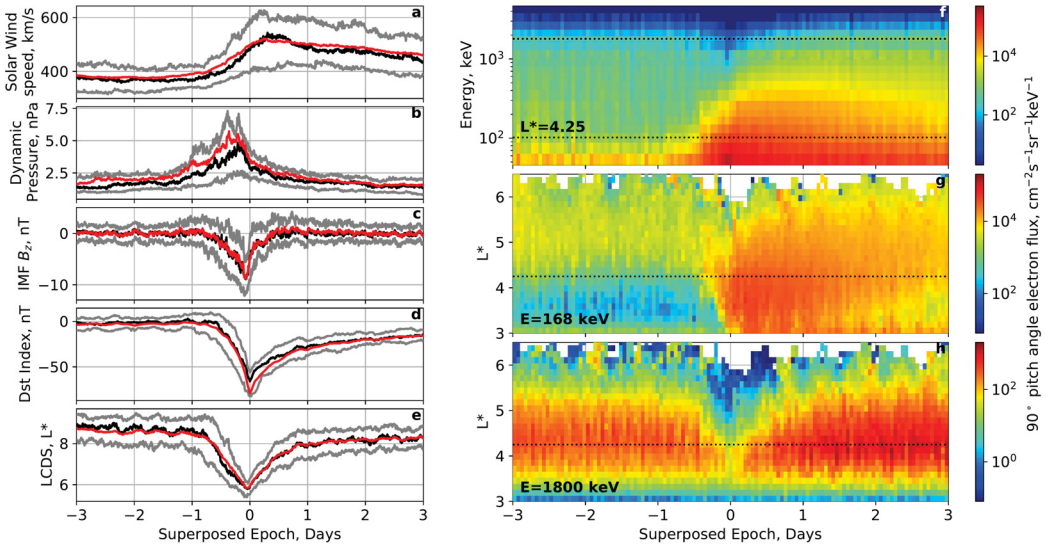

Figure 4.1: Superposed epoch solar wind conditions, geomagnetic indecies, and radiation belt response during the selected events. **a** solar wind speed; **b** dynamic pressure; **c** southward component of the interplanetary magnetic field (IMF); **d** geomagnetic storm-time disturbance index (Dst); **e** L^* of the last closed drift shell (LCDS). Each of these panels shows the mean (red), median (black), and lower and upper quartiles (gray). Superposed epoch **f** median differential electron flux as a function of energy at L^*= 4.25 for a 90° local pitch angle. **g**, **h** median electron flux as a function of L^* at fixed energies of 168 keV and 1800 keV, respectively. Magnetic Electron-Ion Spectrometer (MagEIS) (*Blake et al.*, 2013) and Relativistic Electron-Proton Telescope (REPT) (*Baker et al.*, 2012) data are combined in panels **f-h**. Dotted lines in panels **f-h** correspond to the constant L^* and energies from other panels **f-h**.

losses have also been associated with an effective "hard reset" of the relativistic electrons in the outer belt, from which the characteristics of a newly accelerated population can be studied (*Turner et al.*, 2014). *Reeves et al.* (2016) also discuss similar energy-dependent belt dynamics. Notably, *Murphy et al.* (2018) showed using total radiation belt electron content that the lower energy populations show smaller losses and more intense acceleration, meanwhile the higher energy populations tend to exhibit much larger loss prior to their recovery.

4.3 Investigating Variability of the Electron Fluxes

The superposed epoch analysis also allows a statistical quantification of the variability of the electron fluxes and their dynamics. Figure 4.2 shows the results from this analysis in terms of the median electron fluxes at different energies, locations, and epochs at fixed local 90° pitch angle. The upper and lower quartiles of flux (plotted as error bars) also quantify the level of variability of the electron flux from one storm to the next. Figure 4.2a and Figure 4.2b show that the lower energy electrons are accelerated immediately at the beginning of the recovery phase of the storm, meanwhile, those at higher energies are lost prior to their recovery (c.f., Figure 4.1f-h). Interestingly, the variability of the measured electron flux, as demonstrated by the error bars, shows distinctly different behavior based on energy. At lower energies, the variability drops drastically from about two orders of magnitude to approximately only a factor of two by epoch time zero and later. Meanwhile, the variability of the higher energy electron flux remains at the same level, spanning approximately two orders of magnitude during the entire storm. Note that this is not an instrumental effect since the flux remains below the level of saturation (see e.g., Figure 5 of *Blake et al.* (2013) and Figure 2 of *Baker et al.* (2012)). Notably, the low variability of the seed electron fluxes during the acceleration phase was noted by *Murphy et al.* (2018) and *Turner et al.* (2019). However, the observed effects were not interpreted in the context of the KP limiting process.

This suggests that at lower energies the processes of acceleration and loss

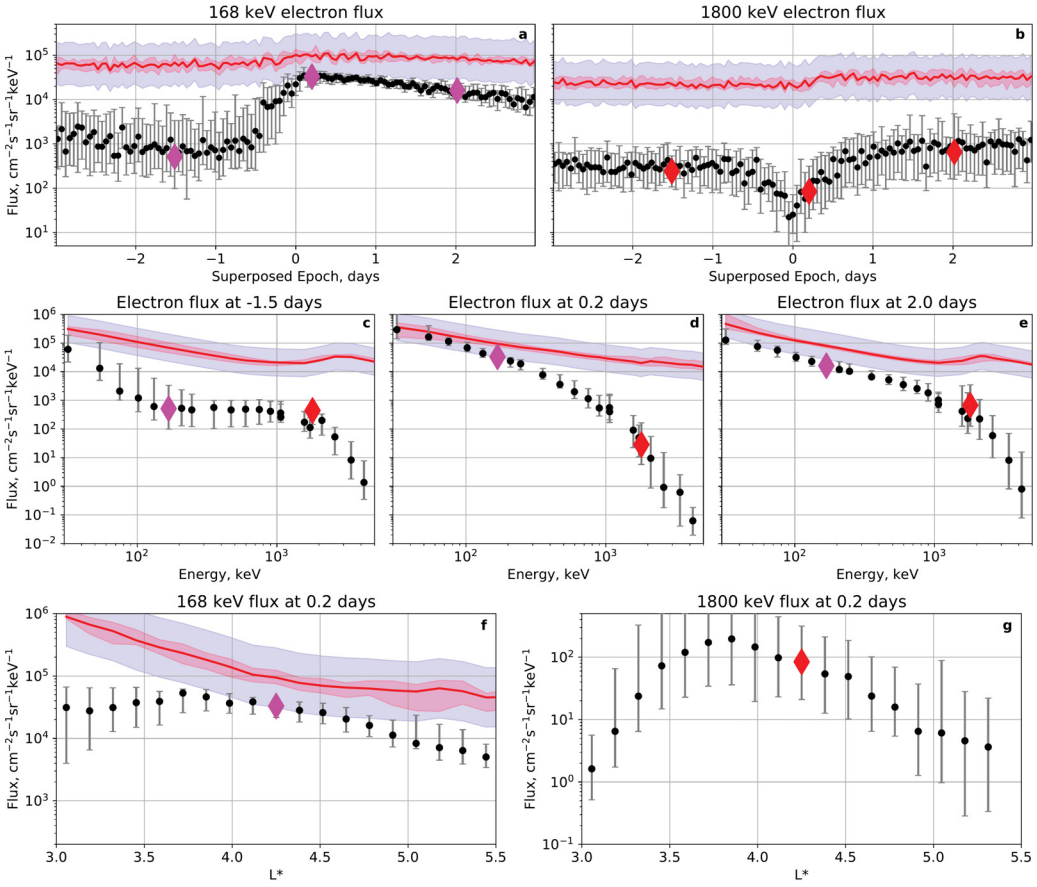

Figure 4.2: Superposed epoch **a-b** electron flux at L^*=4.25 and local 90° pitch angle for two energy channels; **c-e** electron energy spectra at three fixed epoch times at L^*=4.25 and 90° pitch angle; **f-g** electron flux L^* profiles for two fixed energies at epoch time 0.2 days. Diamond markers represent fixed superposed epoch times, energies (168 keV in magenta, 1800 keV in red), and locations used in other panels; median flux is shown with a solid circle, with error bars spanning the flux between the upper and lower quartiles. The median Kennel-Petschek (KP) limit is shown with a red line, with its variability (upper-to-lower quartile) represented as a red shaded region. The blue shaded region represents the original factor of 3 uncertainty assumed by *Kennel and Petschek* (1966).

conspire to produce an almost identical flux, and therefore electron radiation severity at this energy, in the Van Allen belt in every storm! This observed behavior is similar to that predicted by the theoretical model advanced by *Kennel and Petschek* (1966). According to the Kennel-Petschek (KP) theory, once the electron flux reaches a certain threshold, the electron radiation is capped at a maximum flux level. At this flux level, the particle losses arising from scattering into the atmosphere due to interactions with self-generated chorus waves self-limit any further increases in flux. Figure 4.2a-b show the calculated median KP limiting differential flux in red as well as its upper and lower quartiles and model uncertainty. The flux value at the KP limit is determined using the algorithm developed by *Mauk and Fox* (2010) which allows the calculation of the KP limit for a fit to an observed differential energy spectrum (*Mauk*, 2021). This is calculated individually for each storm, and the median and quartiles characterising the variability of the modelled limiting flux level are shown in Figure 4.2. Remarkably, Figure 4.2 shows that the variability of the observed electron flux level from event to event at lower energies drops drastically at the same time as the observed median flux reaches the modelled KP limit, within model uncertainty. Meanwhile, the higher energy electrons remain orders of magnitude below the theoretical KP limit with no apparent changes to the statistical variability of the flux from event to event.

Figure 4.2c-e reveal that the variability of the measured fluxes in different events is very small once the fluxes reach the KP limit. At epoch time 0.2 days, this applies to energies below ∼200 keV (Figure 4.2d); by epoch time 2 days at the end of the acceleration phase this behavior has expanded in energy to reach approximately 500-900 keV (Figure 4.2e). Note that we more accurately determine the domain of influence of the KP limit in the next section. The radial L^* profiles of the electron flux (Figure 4.2f, g) at epoch time 0.2 days further show that the flux of the 168 keV population is at the KP limit within model uncertainty above L^* of 4. Through the storm, the higher energy (e.g., 1800 keV) electron flux remains well below the KP limit, and its variability remains high (large error bars) across the whole of the outer zone.

Notably, the calculation of the KP limit for the differential flux of relativistic

and non-relativistic electrons, developed by *Mauk and Fox* (2010), assumes that the saturated pitch angle distribution can be fitted to a $\sin^{2S}(\alpha)$ function, where α is the pitch angle and S is an anisotropy parameter. For the purposes of this study, similar to the approach adopted by *Mauk and Fox* (2010), we assume that a value of $S = 0.3$ is appropriate at the KP limit. Figure 4.3 shows the superposed epoch evolution of the flux at four energies, and the related anisotropy parameter and full pitch angle distributions derived from Van Allen Probe data at fixed L^*= 4.25. The middle panel of Figure 4.3 shows a rapid increase of the anisotropy parameter S during the acceleration phase after superposed epoch zero. However, electrons with low energies (e.g, electron energies of 168 keV and 354 keV in the first two rows of Figure 4.3), that exhibit a decrease in absolute flux variability as they approach the KP flux limit (Figure 4.3 left column), contemporaneously develop pitch angle distributions that demonstrate a decrease in S that asymptotically approaches S=0.3 after the 90° pitch angle flux reaches the KP limit. Meanwhile, the pitch angle anisotropy parameter for higher energies (e.g., 1800 keV in Figure 4.3 bottom row) remains well above the value of 0.3. It is also evident from the temporal evolution of the pitch angle distribution in the right column of Figure 4.3, that the broadening of the pitch angle spectra during the acceleration phase only occurs at lower energies. Such behavior is consistent with the self-limiting KP theory and also shows that while the low energy 90° pitch angle particles reach the KP limit within hours from the start of the recovery phase, off-equatorial pitch angles at the same energies take anywhere between half a day to two days to fully saturate at the KP limit. Higher energies, however, are associated with longer isotropisation timescales.

4.4 Determining the Energy and Spatial Domains of Kennel-Petschek Influence

In Figure 4.4c we graphically illustrate the overall impact of the KP limit on storm-time energy-dependent belt dynamics by calculating the Pearson correlation coefficient between the difference between the theoretical KP limit

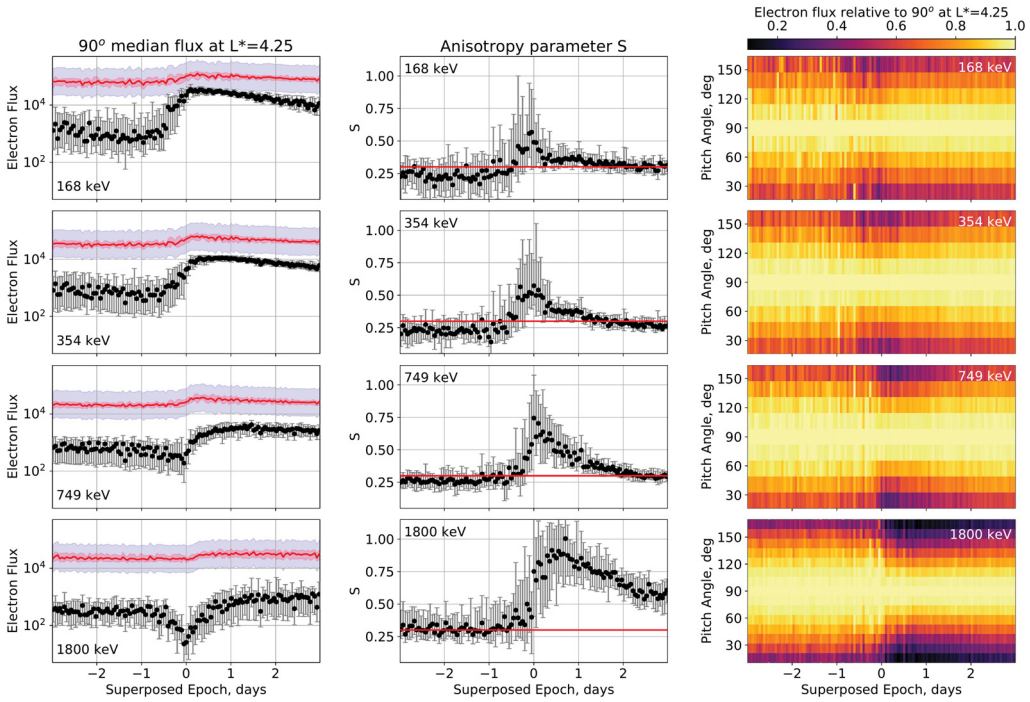

Figure 4.3: (**left column**) Superposed epoch electron flux at L^*=4.25 and 90° pitch angle with the corresponding KP limit in the same format as Figure 4.2**a-b**. (**middle column**) Superposed epoch anisotropy parameter S for the data shown in the left column, black dots represent median values and the error bars represent the interquartile range; the horizontal red line corresponds to the theoretical S=0.3 value assumed for the KP limit calculation. (**right column**) Superposed epoch pitch angle distributions normalized to the 90° flux, again at L^*=4.25 for the same events as in the left and middle columns. All four rows show data for four different fixed energy channels.

and the median flux level (shown in Figure 4.4a) and the variability of the measured fluxes calculated as the distance between the upper and lower quartiles of the distribution (shown in Figure 4.4b). This provides a metric to graphically distinguish between the electrons which are strongly affected by the KP limit, associated with low variability, and those which are not. A strong negative correlation symbolizes that the variability decreases as the flux level gets closer to the theoretical maximum level at the KP limit. Figure 4.4c shows that the energies below ∼850 keV show a very strong negative correlation, with a correlation coefficient of < -0.8, indicating regions where the KP limit drastically affects radiation belt dynamics. The higher energies are instead characterized by a weaker or positive correlation, which represents increases in the median flux values with increases in the flux variability from event to event, thus creating a distinctly different radiation belt response to that observed for the lower energy electrons. This higher energy behavior may be expected due to the high variability of this population from storm to storm, relating to a differential and sometimes delicate balance between acceleration and loss (*Reeves et al.*, 2003; *Turner et al.*, 2019).

Interestingly, Figure 4.4a (see also left column of Figure 4.3) also shows clearly the energy dependence of the time evolution of the median electron fluxes through the course of a storm. Around epoch day 1, the lower energy fluxes at ∼100 keV are already decreasing from their saturation at the KP limit, while higher energies for example around 1 MeV continue to increase. As discussed by *Bortnik and Thorne* (2007) (see also *Summers et al.*, 2002; *Horne et al.*, 2005) this can create an "anchor point" at energies around 500 keV above which electron fluxes are increasing and below which the fluxes are decreasing. According to these authors, this "anchor point" in energy can be interpreted in terms of the separation between the point below which chorus wave-particle interactions dominantly scatter particles into the atmosphere, and above which they accelerate electrons. The results we report here, and as shown in Figure 4.4a, are consistent with these prior observations. However, our analysis reveals more details about energy-dependent radiation belt dynamics within which the Kennel-Petschek limit is crucial. At lower energies, the

electrons are very rapidly capped at the KP limit, preventing further increases, whilst at higher energies the acceleration takes much longer. At the highest energies, however, the fluxes do not have time to reach the KP limit during a storm with a typical duration as seen clearly in Figure 4.2c-e. A significant aspect of this behavior is that particles across a range of energies are inferred to be involved in the generation of chorus waves, involving an energy cascade where electrons with lower energies hit the KP limit first.

It is important to note that the separation between these two different morphological responses of the radiation belt at energies of around 850 keV, as reported here, applies to a typical terrestrial magnetic storm. However, during the most intense and long-lasting storms the KP limit can be reached, but still not exceeded, at somewhat higher energies. This is true both for the results presented by *Mauk and Fox* (2010) during the CRRES era, as well as for the Van Allen Probes era (see Chapter 5 for details). In particular, *Mauk and Fox* (2010) showed that during a "superstorm" event on October 9, 1990, the KP limit was reached by electrons with energies upto around 1 MeV. These results are consistent with those reported by *Zhang et al.* (2021) where they show that the historic maximum flux reached by a 1 MeV electron population during the Van Allen Probes era is consistent with earlier estimations of the KP limit by *Summers and Shi* (2014).

Figure 4.5 extends the Pearson correlation coefficient analysis to different L^* values, and shows that electrons with energies below $\sim$850 keV and L^* values between $\sim$3.5 and $\sim$5.5 show a strong negative correlation (below -0.8), thus revealing a strong influence from the KP self-limiting processes. Such a separation of the radiation belt electron response in terms of energy was hypothesized by *Schulz and Davidson* (1988), and is consistent with the earlier analysis of a single event by *Davidson et al.* (1988); *Mauk and Fox* (2010). Notably, the L^* domain associated with the influence of the KP limit (L^* between $\sim$3.5 and $\sim$5.5) is also commonly quoted as the statistical range of observed chorus wave activity and inferred local acceleration (e.g., *Shprits et al.*, 2008a; *Allison and Shprits*, 2020, respectively). For the benefit of the reader, we also present additional plots in the same format as those shown in

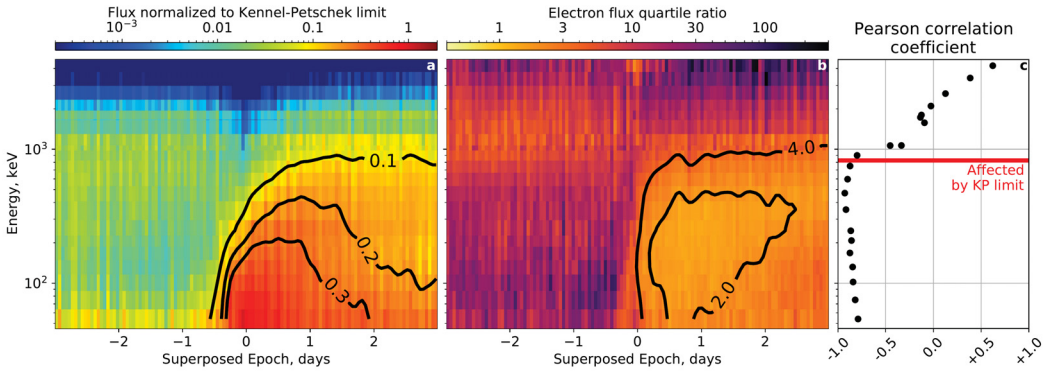

Figure 4.4: Superposed epoch **a** median electron energy spectrum at L^*=4.25 normalized to the respective Kennel-Petschek (KP) limit. The larger the value of this ratio, the closer the median flux to the KP limit. **b**, ratio of the upper to lower quartile flux, small values representing low electron flux variability from event to event. **c**, temporal Pearson correlation coefficient between the data in panels **a** and **b**. Large magnitude negative correlations indicate a strong influence from the KP limit. See text for details.

this chapter but for the full range of the energies, L^* locations, and superposed epoch times at the supplementary material web site `http://www.spacephysics.ca/olifer_etal_2021_grl/`. This allows the reader to investigate the impact of the KP limit on the electron dynamics through an intuitive user interface by selecting from thousands of additional graphs that further validate the overall results presented here.

4.5 Conclusions

In summary, this research reveals how the relativistic electrons show drastically different dynamics in the outer Van Allen radiation belt depending on their energies and location. In particular, and for typical storms, we show how the theoretical *Kennel and Petschek* (1966) limit rapidly controls the dynamics of the electron populations with energies below ∼850 keV between L^* values of ∼3.5 and ∼5.5. Remarkably, this generates a natural limit to the maximum flux level, and quickly caps it at that level, preventing any further increases in flux in almost every storm. Meanwhile, the electrons with higher energy do not show such behavior and in general remain unaffected by the KP limit. For the most intense and long-lasting storms, the maximum energy at which the

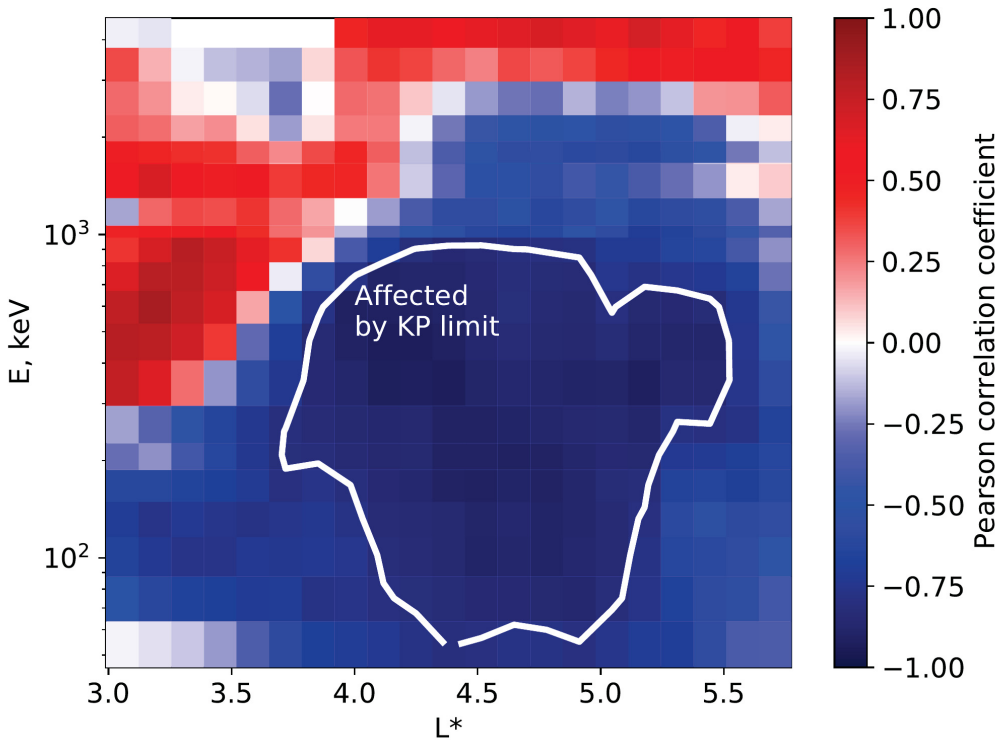

Figure 4.5: Pearson correlation coefficient between the variability of the measured electron fluxes (calculated by the flux difference between the quartiles) and the separation between the mean flux and the theoretical Kennel-Petschek (*Kennel and Petschek*, 1966) limit for different energies and locations. The white line outlines the region with a correlation coefficient of < -0.8. The high negative correlation graphically shows that the variability of the electron fluxes in different storms drops as the electron population gets closer to the KP limit on L^* at the heart of the outer radiation belt.

fluxes are capped by the *Kennel and Petschek* (1966) process can also increase. Nonetheless, the belt response remains divided into two populations separated by energy, lower energies having a flux capped at the KP limit.

It is interesting to consider whether there is a causal relationship between the region of influence of the KP limit shown in Figure 4.5 and the action of local acceleration through wave-particle interactions with lower band chorus waves (e.g., *Reeves et al.*, 2013). However, the fact that chorus waves are excited once the flux reaches the Kennel-Petschek limit does not necessarily imply that chorus waves droves the fluxes up to the KP limit in the first place. In our view, the action of the KP process in limiting and capping the relativistic electron flux is likely agnostic to the process or processes which accelerated the relativistic electron population to that limit in any particular storm in the first place. Nonetheless, once the fluxes reach the KP limit in any energy channel the action of self-organized excitation of chorus waves appears to act to prevent any further increase of fluxes beyond this theoretical maximum in that channel.

Overall, the results of this letter show that it is crucial to assess the influence of the flux-limiting KP process when studying storm-time radiation belt dynamics. For example, by ensuring that the effects of KP limiting processes are included in simulation models and/or acknowledging the possible impacts of related chorus wave generation in analyses of in-situ plasma waves during magnetic storms. Indeed, in terms of the severity of energetic electron flux, it really could either be the best of times, or the worst of times, depending on the electron energy and the influence of the Kennel-Petschek limit.

Chapter 5

A Natural Limit to the Spectral Hardness of Worst-Case Electron Radiation in the Terrestrial Van Allen Belt

Based on *Olifer et al.* (2022a) A natural limit to the spectral hardness of worst-case electron radiation in the terrestrial Van Allen belt, *Journal of Geophysical Research: Space Physics*, doi:10.1029/2022JA030506. The paper was reformated to fit thesis formatting guidelines without any changes to its content.

The flux of relativistic electrons in the terrestrial Van Allen radiation belt can vary by orders of magnitude during a geomagnetic storm. The response is typically assumed to be controlled by an often delicate balance between acceleration and loss processes. Here we analyze all 133 magnetic storms from the NASA Van Allen Probes era. We show how the belts demonstrate a repeatable response which limits not only the worst case flux, but also controls and delivers a limit to the severity of the spectral hardness, consistent with the theory of Kennel and Petschek first developed over 50 years ago. When this theory is extended to relativistic energies, the observed electron flux is seen to reach a naturally limited worst case with a clear energy dependence. Here we show how the Kennel-Petschek theory can explain the evolution and hardening of the electron spectrum during geomagnetic storms. It also introduces an energy-dependent maximum flux limit. This limit is never reached during the

Van Allen Probes era at energies above 2.6 MeV, meanwhile, it is reached within hours at lower energies (∼100 keV) in almost every storm. No current radiation belt models include this effect; without it, they cannot accurately predict the consequent radiation dynamics. Overall, our results demonstrate how this creates a remarkable absolute natural limit to both the spectral hardness and the severity of extreme electron space radiation.

5.1 Introduction

Ever since the discovery of the Van Allen radiation belts around the Earth (*Van Allen and Frank*, 1959), understanding the acceleration and loss processes which are responsible for their complex dynamics, and examining the related radiation hazards, has remained an active and high priority area of research (e.g., *Baker et al.*, 1987, 1994; *Baker*, 2001). From the point of view of radiation impacts on satellite electronics, assessing the worst case fluxes, spectra, and fluence remains of significant interest (e.g., *O'Brien et al.*, 2007; *Horne et al.*, 2018, and references therein). In terms of developing a physical understanding of the processes which shape the electron radiation belts, assessing not only which processes are dominant under specific solar wind driving, but also how they are coupled under extreme conditions, is crucial. Typical radiation belt modeling assumes that the resulting electron fluxes are determined by an often delicate balance between acceleration and loss processes (*Reeves et al.*, 2003). However, over 50 years ago, *Kennel and Petschek* (1966) proposed a theory that suggested that the maximum energetic electron flux might be limited by a self-organized process triggered inside the belts.

The fundamental concept advanced by *Kennel and Petschek* (1966) was that the number of trapped energetic electrons could be capped as a result of the balance which occurs due to the relationship between the growth rate of chorus waves, driven by the pitch angle anisotropy of the energetic electron populations, and the resulting pitch angle scattering which such waves also introduce. Since the wave growth rates increase with increases in electron flux, whilst at the same time increasing the rates of pitch angle diffusion towards

the loss cone, eventually there is a natural limit. At a limiting flux level, which is also commonly referred to as the Kennel-Petschek limit, these processes balance such that any further increases in flux result in additional atmospheric losses. This balance naturally generates not only a capped equatorial flux but also produces an equilibrium with a characteristic asymptotic pitch angle distribution where the rate of transport into the loss cone matches the rate at which new flux is added. We refer the reader to the original paper by *Kennel and Petschek* (1966) for more details.

Overall, therefore, according to the Kennel-Petschek (KP) theory the precipitation loss rates are explicitly connected to levels of the electron flux. Such that, when equatorial flux reaches a maximum level, strong electron cyclotron plasma wave growth would trigger fast scattering in pitch angle. Current studies suggest that fast pitch angle diffusion can occur on timescales as short as the order of 1-hour (e.g., *Thorne et al.*, 2010; *Claudepierre et al.*, 2020). This self-organized process would act to limit any further increases in equatorial flux since these would be counter-balanced by the atmospheric losses arising from pitch angle scattering into the loss cone. The *Kennel and Petschek* (1966) theory was reformulated in terms of differential flux by *Schulz and Davidson* (1988) and extended up to relativistic by energies by *Summers et al.* (2009). Importantly, the original formulation of the KP theory in terms of the integral flux postulated the limiting of the electron population predominantly for electrons with energies ∼10s keV. However, later studies by *Schulz and Davidson* (1988), *Davidson et al.* (1988), and *Mauk and Fox* (2010)examining differential electron flux presented evidence from case studies that higher energy electrons up to ∼1 MeV may also be limited by the KP processes. However, this only occurs when the fluxes at those higher energies are large enough to activate the self-limiting KP process. In part due to the lack of appropriate observational data, relatively little attention has been given to assessing broader applicability and impact of this theory and it has remained largely untested. As a result, no current radiation belt models include such self-limiting effects. In this chapter, we clearly show how the KP process dynamically controls the hardening of the electron flux spectrum up to relativistic energies. In case studies presented

here, we show that this extends up to populations with energies of 2.6 MeV during the Van Allen Probes era.

A recent superposed epoch study by *Olifer et al.* (2021b) has shown that electrons with energies below ∼850 keV are strongly affected by the presence of the Kennel-Petschek limit during geomagnetic storms. The results from *Olifer et al.* (2021b) showed that lower energy electron populations quickly reach the Kennel-Petschek limit during the main phase of the storm, with higher energy electrons successively hitting the KP limit at later times. However, these authors also emphasized that the effects of the Kennel-Petschek limit could also be observed at higher energies during the storms exhibiting the most intense electron acceleration. A more detailed investigation of the impacts of the Kennel-Petschek limit on the dynamics of electrons at relativistic and strongly relativistic energies is the main focus of this chapter.

In this study, we use data from magnetic storms from the entire NASA Van Allen Probes mission (*Mauk et al.*, 2012; *Spence et al.*, 2013) to demonstrate clearly and conclusively that the Kennel-Petschek limit not only creates a natural limit to electron radiation flux in the Van Allen belts, but largely controls the energy and time dependence of the worst case fluxes as well. We reveal how this controls the dynamical evolution of the energy-dependent electron flux and, in particular, controls the evolution of the knee in the electron energy spectrum. We further show that lower energy fluxes (∼10s-100s keV) rapidly reach the Kennel-Petschek limit early during a storm, with slower acceleration at higher energies producing an increasingly hard spectrum. For the most extreme space storms, this can extend in energy up to relativistic energies, whose maximum flux and energy spectral gradient are capped, in remarkable agreement with the Kennel-Petschek theory. For example, and as we show here, the worst case flux for relativistic electrons with energies below 2.6 MeV is capped to a maximum at the Kennel-Petschek limit.

5.2 Data and Methodology

In this study, we analyzed the differential flux from all of the magnetic storms observed during the Van Allen Probes era since their launch in 2012 until the end of their operations in 2019, encapsulating a large portion of the solar cycle 24. In particular, we use the Van Allen Probes differential directional electron flux data provided by the Energetic Particle, Composition, and Thermal Plasma (RBSP-ECT) investigation team (*Spence et al.*, 2013), from the Magnetic Electron-Ion Spectrometer (MagEIS) (*Blake et al.*, 2013) and Relativistic Electron-Proton Telescope (REPT) (*Baker et al.*, 2012) instruments. We focus on examining the maximum electron fluxes observed during storms. We begin by illustrating the impacts of the relativistic Kennel-Petschek limit by presenting an analysis of electron flux from six of the largest events from this epoch. The first five storms chosen are those with the largest enhancements in 2.6 MeV energy electron flux as measured by the Van Allen Probes from September 2012 until January 2019. The sixth storm we present is the widely studied October 2012 storm whose dynamics were presented in detail for example by *Reeves et al.* (2013). In addition to these five strongest 2.6 MeV electron flux events, the October 2012 storm nicely further illustrates the impacts of the Kennel-Petschek limit during an event with a comparatively rapid and intense ultra-relativistic (>2 MeV) electron flux enhancement.

A crucial element of this analysis is an estimate of the limiting electron flux which is predicted by the self-limiting processes described by *Kennel and Petschek* (1966). As outlined above, the principle of the KP limit relies on the self-limiting balance between chorus wave growth and resulting pitch angle transport into the loss cone. Enhancements in electron flux and pitch angle anisotropy drive chorus waves which themselves affect the pitch angle distribution. At the KP limit these processes become balanced, such that wave growth is so strong that the resulting wave-particle interactions result in the fast transport of electrons into the atmosphere and which prevent any further increases in flux. At the KP limit, the result is that flux is capped and the pitch angle distributions are partially isotropised to also reach an asymptotic

state.

In this chapter, we use a technique developed by *Mauk and Fox* (2010) for estimating the KP limit which incorporates the relativistic corrections from *Summers et al.* (2009) and the reformulation of the of the original KP theory in terms of the differential flux from *Schulz and Davidson* (1988). Unlike the original Kennel-Petscheck theory formulation in terms of the intergral flux by *Kennel and Petschek* (1966), *Mauk and Fox* (2010) approach enables investigation of differential characteristics of the limit as a function of minimum resonant energy and consistent with modern satellite measurements. In line with the original KP paper, *Mauk and Fox* (2010) state that the Kennel-Petschek limit for electrons is defined as the electron flux level at which the overall chorus wave amplitude is sustained as the result of ongoing wave growth, including amplitude losses due to wave propagation along the field line. Partial reflection from the ionosphere and additional growth of the reflected wave in the equatorial region are used in the KP theory to establish this asymptotic limit. Mathematically, this can be described using a condition $G \cdot R = 1$, where G is a net gain of whistler wave amplitudes as the waves pass through the magnetic equator and R is the ionospheric reflection coefficient. Typically, R is assumed to be $\sim 5\%$, the value of which we also use in our study. Here we follow the derivation presented by *Mauk and Fox* (2010), such that the above condition can be rewritten as equation (5.1), where γ is the temporal growth rate and V_g is the chorus wave group speed.

$$\gamma(J(E,\alpha)) = \ln G \frac{V_g(\omega)}{LR_E} \approx \frac{3V_g(\omega)}{LR_E}. \tag{5.1}$$

In equation (5.1) the wave growth rate, which depends on the differential electron flux $J(E,\alpha)$, is related to the group speed which itself depends on the wave frequency ω. The KP limit is obtained when equation (5.1) is satisfied for the flux at energy, E, and for the group speed where waves with frequency ω are resonant with electrons at energy E.

In this chapter, we determine the chorus growth rate using the expressions as provided in *Mauk and Fox* (2010) and which were first introduced by *Summers*

et al. (2009) in a modified form of the expressions derived by *Xiao et al.* (1998). It also is important to note that although there are uncertainties in the exact value of R, the resulting limiting flux is only weakly dependent on R, since it depends on the logarithm of $1/R$. The calculation of temporal growth rate γ and the group speed V_g in this chapter, the equatorial magnetic field strength is taken from the *Tsyganenko and Sitnov* (2005) storm-time magnetic field model, and the electron number density is taken from the *Sheeley et al.* (2001) empirical model.

Notably, the wave growth rate γ depends on the anisotropy of the pitch angle distribution. In their paper, *Mauk and Fox* (2010) used observations of the electron pitch angle distributions during strong geomagnetic storms to pick the value of the anisotropy parameter S (related to the pitch angle distribution shape $\sin^{2S}\alpha$). While their analysis showed that the values of S may range from 0.25 during super storms to 0.4 during storms, *Mauk and Fox* (2010) rounded up from $S = 0.25$ to take a value of $S = 0.3$ as an estimated anisotropy parameter of the pitch angle distribution when the electron fluxes reach the KP limit. In this chapter, we also use the value of $S = 0.3$ for calculating the limiting flux values to be consistent with the *Mauk and Fox* (2010) approach, an assumption which we assess in section 5.3.2 of this chapter.

As described by *Summers et al.* (2009) a self-consistent model that involves the generation of the chorus waves in the magnetosphere and their interaction with electrons of different energies is required in order to properly assess the energy spectrum and pitch angle distribution at the KP limit. It is possible that this approach would yield a more accurate energy-dependent anisotropy parameter, one that better describes the shape of the pitch angle distribution at the KP limit. As noted by *Summers et al.* (2009), it may also be appropriate to incorporate oblique wave propagation and and non-linear effects. Nonetheless, progress can be made with approximations. Here we use the *Mauk and Fox* (2010) approach to calculating the KP limit and which involves fitting the observed electron energy spectrum with a kappa distribution, as shown in equation (5.2), and integrating it in momentum coordinates to obtain an estimate of the liming differential flux.

$$J = C\frac{E\left(kT\left(\gamma_1+1\right)+E\right)^{-\gamma_1-1}}{1+\left(E/E_0\right)^{\gamma_2}}, \tag{5.2}$$

where the numerator represents an assumed empirical kappa distribution (a Maxwellian core with a power law tail) for a collisionless plasma and the denominator adds the additional power law tail that is present in the observed spectra for ultra-relativistic populations. E is the electron kinetic energy and C, kT, γ_1, γ_2, and E_0 are fitting parameters which characterise the differential flux, J. In this approach, kT is a characteristic electron temperature of the Maxwellian core in electron-volts. The fitting is performed using numerical techniques present in the scipy package for python. The full Mathematica code that performs this calculation, which was used in our study, is publicly available at *Mauk* (2021). We refer the reader to the original *Mauk and Fox* (2010) paper (their chapter 6) and Chapter 2 of this thesis for a more detailed description of the approach used to derive the KP-limited differential flux.

To verify the broad applicability of the Kennel-Petscheck theory to storms throughout the Van Allen Probes era, we also present a statistical analysis of the maximum electron fluxes reached in all of the 133 geomagnetic storms with Dst<-30 nT to further demonstrate the importance and impact of the Kennel-Petschek limit on electron radiation trapped in the terrestrial Van Allen belts.

5.3 Results

5.3.1 Energy-dependant flux limit during intense storms

Figure 5.1 shows the 2.6 MeV energy differential electron flux at local 90° pitch angle for the three storms with the largest flux in this channel during the Van Allen Probes era. The color plot on the background of each panel shows the radiation belt differential flux response as a function of time and L^*. Here, L^* is the generalized (*Roederer*, 1970) L-shell parameter and approximates an equivalent radial distance of a symmetric electron drift path in Earth radii. For the purposes of this study, we use the *Tsyganenko and Sitnov* (2005) magnetic field model for calculating the L^* at local 90° pitch angle to account for the

storm-time dynamics of the magnetosphere. The behaviour of the electron flux is seen to be very similar for each of these storms. The quiet pre-storm period is followed by loss during the main phase and a subsequent intense enhancement of the differential flux above pre-storm levels. A line plot of the magnitude of electron differential flux in the 2.6 MeV energy channel in the heart of the outer radiation belt at L^*=4.25, and whose magnitude is shown on the right axis of Figure 5.1, provides a quantification of these flux dynamics for the benefit of the reader. Four characteristic times during the course of each storm are selected for flux comparisons against the relativistic Kennel-Petschek limit. In particular, "Pre-storm" marks conditions before the storm where no enhancement or loss has yet occurred. "Start" marks the beginning of the relativistic electron enhancement, as determined by the first time the differential flux at L^*=4.25 in the 2.6 MeV channel is increased. "End" designates the time when the maximum flux during the event in this channel is reached. "Middle" designates the time when the flux level is half-way-through "Start" and "End" levels on the logarithmic scale. The times of these comparisons are marked with vertical lines in each panel. At each of these times we show the measured energy spectra and corresponding relativistic Kennel-Petschek limit in Figure 5.2.

Figure 5.2 shows the evolution of the electron energy spectra for the three geomagnetic storms with the largest 2.6 MeV electron flux during the Van Allen Probes mission. During the pre-storm interval (Figure 5.2a-c; top row) the measured flux across all energy channels stays well-below the Kennel-Petschek limit as expected. However, as soon as the acceleration and flux recovery starts after the period of storm main phase losses (Figure 5.2d-f; second row) the flux at the lower energies immediately and quickly rises to reach but not exceed the Kennel-Petschek limit, within the factor of 3 uncertainty. At higher energies, the fluxes increase such that the highest energies reach the Kennel-Petschek limit later in the storm. This produces a dynamical evolution of the differential energy spectra such that there is a characteristic knee in the spectra at the highest energy which has reached the Kennel-Petschek limit at that time (Figure 5.2g-i; third row). The flux at energies below the knee all

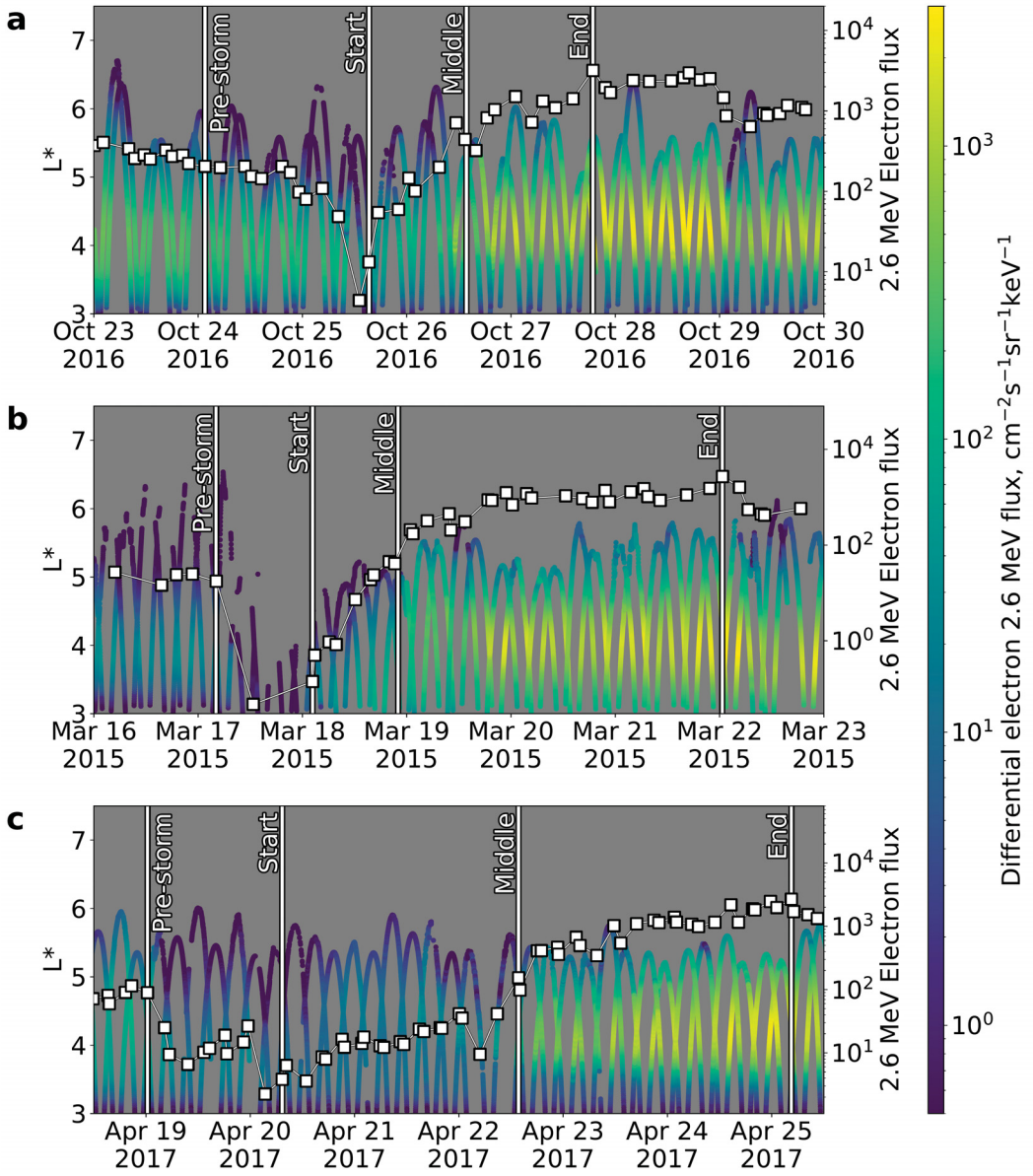

Figure 5.1: 2.6 MeV differential electron flux for local 90° pitch angle during the three geomagnetic storm events with the largest flux reached during the Van Allen Probes era: a, the October 24-31, 2016 geomagnetic storm, b, the March 16-23, 2015 storm, c, April 19-26, 2017 storm. Each panel shows the color plot of the measured differential flux as a function of time and L^*, meanwhile, a white scatter plot shows electron flux in units of $\mathrm{cm}^{-2}\mathrm{s}^{-1}\mathrm{sr}^{-1}\mathrm{keV}^{-1}$ at L^*=4.25 (right axis).

follow and are capped at the Kennel-Petschek limit, whilst the flux at energies above the knee has a steeper spectral slope and lies below the Kennel-Petschek limit. Depending on the intensity and duration of the storm, and the speed

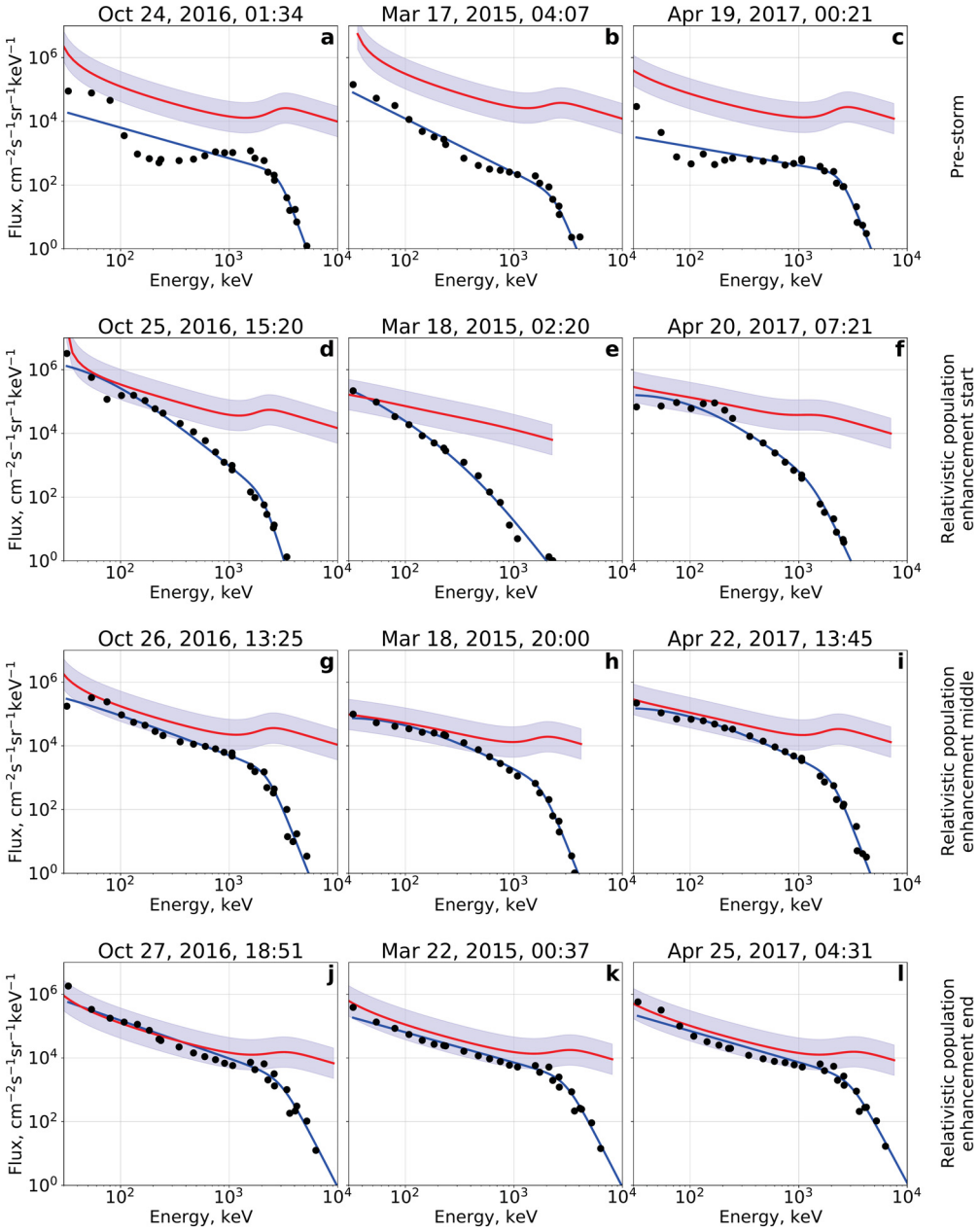

Figure 5.2: Electron flux energy spectra and Kennel-Petschek limits during three geomagnetic storms with intense enhancement of 2.6 MeV electron population. Each column shows one of the storms from Figure 5.1, at the characteristic time (Pre-Storm, Start, Middle, and End) shown in each row. The black scatter plot shows the electron flux measurements, the blue line shows a fit of the relativistic kappa distribution to the spectra. The red line shows the calculated Kennel-Petschek limit and the blue shaded region shows the factor of 3 of uncertainty of the Kennel-Petchek limit (*Kennel and Petschek*, 1966).

of acceleration, the energy where the knee occurs can be higher or lower at any given time during the storm – but during the active acceleration phase the knee moves along the Kennel-Petschek limit towards higher and higher energies with time. Previous results by *Fox et al.* (2006) and *Mauk and Fox* (2010) associated a spectral knee with the Kennel-Petschek limit but did not assess any related dynamics. However, as we show here for the first time, the Kennel-Petschek limit also strongly controls the dynamical evolution of the storm time relativistic electron spectra in an elegant and repeatable manner. Indeed, the spectral shape and the spectral slope evolve in a very characteristic way through the course of the storm.

This result clearly demonstrates, using the examples from the three most severe electron radiation storms in the Van Allen Probes era, that even during the most intense enhancements of the electron population the relativistic particles stay either exactly at the Kennel-Petschek limit or remain below it. The limit is not exceeded. It starts with lower energies reaching the limit first, with higher energies following later. This gradual pressing of the differential flux towards the Kennel-Petschek limit explains the spectral knee, and indeed its temporal evolution towards higher energies during a storm.

Interestingly, and although we have used the shape of the individual storm electron energy spectra to calculate the relativistic Kennel-Petschek limit at every epoch in each storm independently, the limit is not a strong function of the spectral shape. Indeed, the theoretical Kennel-Petschek limit does not appear to change from storm to storm by more than a factor of approximately 2 across all energy channels. This result is consistent with that of *Olifer et al.* (2021b) where the superposed epoch analysis of the limiting flux shows that the Kennel-Petschek limit does not vary by more than a factor of 2 between the upper and lower quartiles within the ensemble of the 70 storms studied. This limit is controlled by the nature of the magnetized plasma and therefore, accordingly to our results, cannot be surpassed by enhancement processes that are acting on timescales longer than the typical timescales of the atmospheric loss, which are usually around 1-hour (*Thorne et al.*, 2010; *Gu et al.*, 2012; *Spasojevic et al.*, 2015; *Ozeke et al.*, 2019). Overall, our results show that there

is an upper limit for the differential electron flux at relativistic and strongly relativistic energies in the Van Allen belts of the Earth.

5.3.2 Impact of the Kennel-Petschek on pitch angle distributions

It is also crucial to investigate the dynamics of electron flux pitch angle distributions (PAD) during these storms, since if the Kennel-Petschek theory is valid it implies that there should be a characteristic signature in the evolution of the PAD as well. In particular, approaching the Kennel-Petschek limit, pitch angle diffusion should evolve PAD towards a more isotropic state.

Figure 5.3 shows the measured PAD of the differential flux for three energy channels during the acceleration periods of the three previously analyzed storms (Figure 5.2) at energies of 597 keV, 1575 keV, and 2100 keV, in comparison with the Kennel-Petschek limit. For easier comparison across different phases of the storms, we show measured PAD normalized to the limiting Kennel-Petschek flux level at 90° pitch angle. The electron PADs are also fitted to $\sin^{2S}\alpha$ dependence, where α is the pitch angle and S is an anisotropy parameter (*Mauk and Fox*, 2010). Both measurements and PAD fits are shown in lines with green, blue, and black colors for the beginning, middle, and end of the acceleration phase, respectively. At the Kennel-Petschek limit the anisotropy parameter appears to approach $S = 0.3$ in good agreement with the assumption made by *Mauk and Fox* (2010). The pitch angle dependence of the Kennel-Petschek limit, corresponding to $S = 0.3$, is shown in red in each panel. As previously, the blue shading shows an assumed uncertainty of plus or minus a factor of three in the Kennel-Petschek limit. For PAD which peak at 90 degrees, the color-coded value of S arising from a fit to the observed PAD is provided numerically at the bottom of each panel in the figure.

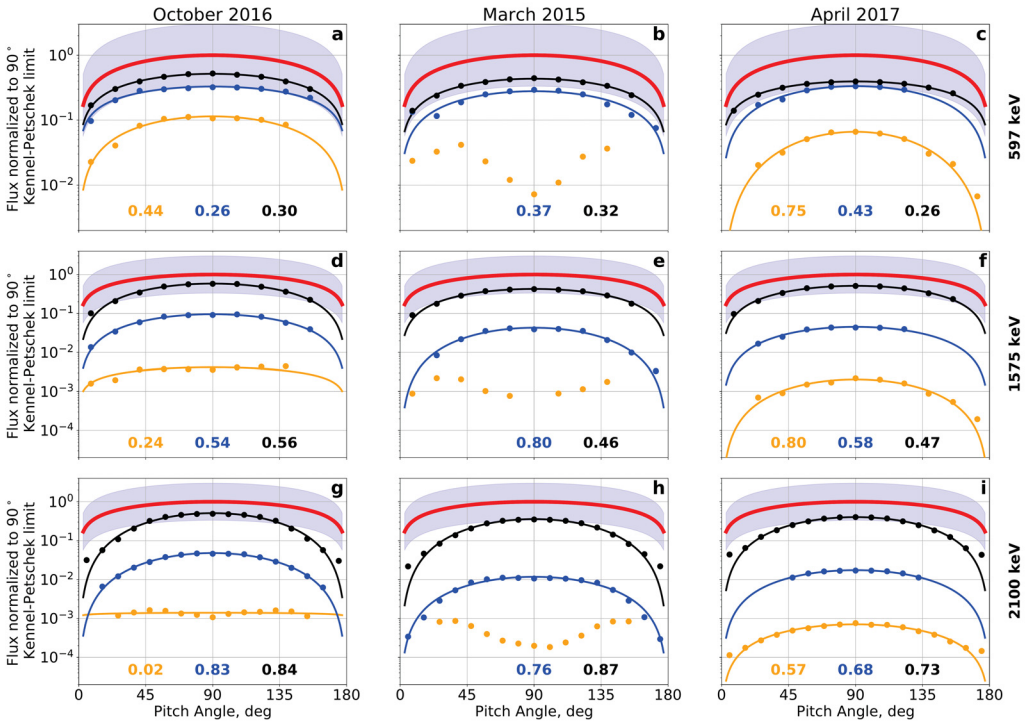

Figure 5.3: Normalized electron flux pitch angle distributions at L^*=4.25 and corresponding Kennel-Petschek limits during the three geomagnetic storms with the most intense electron enhancements at 2.6 MeV energy during the Van Allen Probes era. Each panel shows the evolution of measured electron flux pitch angle distribution (PAD) for different energies during the three storms from Figure 5.2. The flux measurements were normalized to the evaluated Kennel-Petschek limit at 90° pitch angle. a-c, normalized 597 keV electron PAD measured by the MagEIS instrument for three geomagnetic storms with the strongest enhancement of 2.6 MeV population in the Van Allen Probes era. d-f, normalized 1575 keV electron PAD measured by the MagEIS instrument. g-i, normalized 2100 keV electron PAD measured by the REPT instrument. The measured PAD are shown in scatter plot on each panel with orange color representing the time at the start of the acceleration process, the blue representing the middle, and the black representing the end of the 2.6 MeV acceleration phase. PAD's are fitted to a $\sin^{2S}\alpha$ function, where α is the pitch angle, shown in the same color. The fitted anisotropy parameter, S, is presented on the bottom of each panel in the respective color. The distributions at the beginning of the acceleration in the March 2015 storm have a butterfly distribution, thus fits and S values are not shown for those times.

Figure 5.3 shows that for the 597 keV energy channel the electron fluxes across all pitch angles approach the Kennel-Petschek limit, and that the PAD becomes more isotropic to reach a value close to $S = 0.3$ by the end of the

storm. The electron flux PAD of the 1575 keV energy channel at 90° pitch angle is also within a factor of 3 from the estimated limiting flux value. However, the anisotropy parameter at the end of the enhancement remains slightly higher than 0.3. This is perhaps not unexpected since this energy channel is closer to the region separating lower energies at the Kennel-Petschek limit from those high energies that do not reach the limit. At even higher energies in the 2100 keV energy channel, the S-value which is reached by the end of the storm is even higher. The increased anisotropy parameters for the relativistic electron population above 1 MeV might also suggest a possible role for additional precipitation loss processes, for example as a result of scattering of electrons into the atmosphere by electromagnetic ion cyclotron (EMIC) waves which can act on the > 1 MeV electron populations in the magnetosphere (*Meredith*, 2003) and which preferentially scatter lower pitch angle particles into the loss cone (*Shprits et al.*, 2016). However, a study of the impact of chorus and EMIC waves on the electron population in the presence of the Kennel-Petschek limit is beyond the scope of this paper.

5.3.3 Investigating the impact of the Kennel-Petschek limit during additional storms: case-studies and statistics

It is interesting to further investigate how the Kennel-Petschek limit influences the characteristic evolution of the energy spectra in the electron radiation belts during additional storms, to further validate the conclusions drawn from the observations in the three geomagnetic storms presented above. For that purpose, we show a comparison between the observed electron energy spectra and the corresponding Kennel-Petschek limiting fluxes for three additional events in the Supplementary Figures E.5-E.7. The events used here are the October 6-10, 2015, September 26-30, 2016, and October 8-10, 2012 geomagnetic storms – representing the two next most intense radiation belt storms as characterized using 2.6 MeV electron flux enhancement, as well as the October 2012 storm studied by *Reeves et al.* (2013). For these additional storms, very similar strong enhancements of the relativistic flux are again observed, and the flux and

energy spectra are again seen to evolve in the same way and are enhanced only up to the Kennel-Petschek limit.

However, at lower energies, <100 keV, for the October 2012 storm, there is clear evidence of a short time period early in the storm where the Kennel-Petschek limit appears to be exceeded from October 8 2012, 23:40 until October 9, 9:00. Such a feature is not observed at higher energies. Similar behaviour for low energy electrons is occasionally present for short period of time in the other storms analyzed in this paper. However, the times when those populations exceed the limiting flux along are much shorter than observed during October 2012, and are typically only observed along a single orbit of one of the two Van Allen Probes. In our opinion, albeit confined only to these lower energies, this short period corresponds to an interval associated with a rapid and strong direct electron injection from the magnetotail. If the injection occurs on sufficiently short timescales, this can allow the electron population with energies <100 keV to temporarily exceed the Kennel-Petschek limit. This assumption, however, has to be confirmed by additional studies, ideally incorporating multi-point measurements from different satellites that directly observe the evolution of such lower energy electron injection events. Interestingly, however, the interval when the Kennel-Petschek limit is exceeded is short and the differential flux in these channels quickly returns to, and appears to be limited by, the Kennel-Petschek limit.

Notably, and possibly also relevant to our conclusions about the importance of the Kennel-Petschek limit for controlling worst case storm electron fluxes, the October 2012 storm has been reported as one showing signs of local acceleration of the ultra-relativistic population (*Reeves et al.*, 2013). According to *Reeves et al.* (2013), this particular storm was associated with very rapid relativistic electron acceleration associated with strong chorus waves on the electron cyclotron branch. Nonetheless, the differential energy spectra in the heart of the belts appears to be constrained by the Kennel-Petschek limits in exactly the same way as for the other five large radiation storms presented here.

The general validity of the importance of the Kennel-Petschek theory for controlling the worst case electron fluxes in the terrestrial Van Allen belts

is confirmed by performing a statistical analysis of electron fluxes in all 133 geomagnetic storms with a minimum storm time disturbance index (Dst) below -30 nT from the entire Van Allen Probes era from September 2012 until October 2019. Figure 5.4 shows occurrence distributions for the largest electron fluxes reached in five selected energy channels during these geomagnetic storm events and how they are all confined to levels below the calculated Kennel-Petschek limit. The top row of Figure 5.4 shows the occurrence distributions of electron fluxes for different energies with the median and 1st and 99th percentiles of the calculated Kennel-Petschek limit during the times when these fluxes were measured. The lower energy distributions are pressed to the calculated limiting fluxes in the majority of the storms but never exceed them. Such behavior creates strongly asymmetric distributions that fail the normality test due to the large skewness parameter ($|\widetilde{\mu}_3| > 2$). This result shows that the Kennel-Petschek limit is usually reached at some point during the acceleration phase of the storm for electrons with energies below ∼1000 keV. As shown earlier, the lower energy electrons reach this limit much earlier in the storm, within a matter of hours. Higher energies are still influenced by the presence of the limit but are less skewed, with the highest energy channel of 3400 keV being essentially symmetric. These plots also show that the Kennel-Petschek limit derived using the parameters in each storm does not change significantly from event to event. On average it varies from the median by a factor of 2 at most, which is well within a factor of three of model uncertainty identified by Kennel and Petschek in their original paper (*Kennel and Petschek*, 1966). Very significantly, and as a direct consequence, this demonstrates that the Kennel-Petschek limit can be used to assess the worst case relativistic electron radiation levels in the Van Allen belts.

The middle row of Figure 5.4 shows the occurrence distribution of the largest fluxes normalized to the corresponding Kennel-Petschek limit in in each storm. Since in general the KP limit does not vary significantly from storm to storm, the occurrence distribution of the normalized fluxes in the middle row is very similar to that of the absolute fluxes in the top row of Figure 5.4. Both occurrence distributions demonstrate very clearly the role of the Kennel-

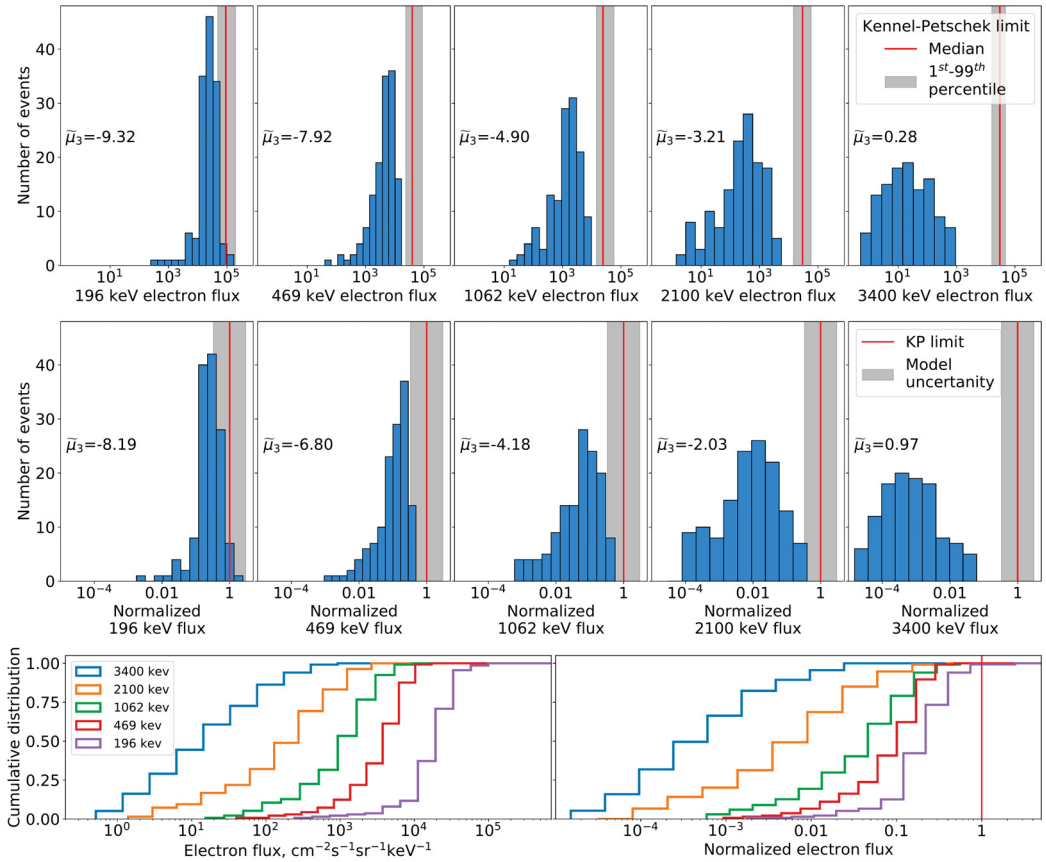

Figure 5.4: Occurrence distributions of the maximum electron flux at L^*=4.25 reached during all 133 geomagnetic storms with Dst<-30 nT during the Van Allen Probes era in comparison to Kennel-Petschek (KP) theory. Top row, occurrence distribution of the maximum electron flux in units of $\mathrm{cm^{-2}s^{-1}sr^{-1}keV^{-1}}$ reached at L^*=4.25 in five selected energy channels during all 133 geomagnetic storms with Dst<-30 nT. The median Kennel-Petschek limit, evaluated independently at the time of maximum flux for each storm, is shown with a red line and the grey area depicts the effective total variation in the KP limit by showing the 1st and 99th percentile in the distribution of these KP limits. Each panel also shows the skewness parameter, $\widetilde{\mu}_3$, which defines the symmetry of the distribution. Distributions with skewness values above or below ± 2 are considered asymmetric. Middle row, occurrence distribution of fluxes normalised to the Kennel-Petschek limit in that event. The red line represents the normalised Kennel-Petschek limit with a value of unity, and the grey area represents the factor of 3 uncertainty in the model. Bottom row, cumulative occurrence distributions of the absolute and normalized maximum fluxes, left and right panels respectively, with different energies shown in different colors.

Petschek theory in controlling the maximum electron flux in the radiation belt within a small uncertainty; not only in the most extreme events presented earlier, but also over the entire distribution of the 133 (Dst<30 nT) storms from the entire seven years of the Van Allen Probes era. Similarly to the distribution of absolute flux values, the skewness parameter of these distributions decreases in absolute value with the increases in energy, reaching an essentially symmetric distribution for the largest energy and where the maximum flux at L^*=4.25 for every single one of these 133 storms remained below the Kennel-Petschek limit. The bottom row of Figure 5.4 shows two cumulative occurrence distributions using the flux and normalized flux distributions from the first two rows in the left and right panels, respectively. It is evident that the electron populations that are drastically affected by the Kennel-Petschek limit show clear signs of a skewed distribution (large absolute values of $\widetilde{\mu}_3$) and where the distributions of maximum flux are capped by the limiting KP flux. At 196 keV, over 89 percent of these 133 storms reach a flux within a factor of 10 of the KP limit. Conversely, by energies of 3400 keV none of these 133 events has a flux which gets within a factor of even 30 of the KP limiting flux, such that the occurrence distributions appear symmetric and unaffected by the KP limit at these higher energies. Overall, this demonstrates unequivocally that the Kennel-Petschek theory explains the worst case fluxes in the Van Allen belts – at least for the storms observed during the seven years of Van Allen Probes era.

5.4 Discussion and Conclusions

It is interesting to speculate whether there is a causal relationship between the period of the flux reaching the Kennel-Petschek limit and the generation of the chorus waves which Reeves et al. implicate in the later relativistic particle acceleration during the October 2012 storm. Indeed, many papers have presented results connecting chorus waves with radiation belt acceleration. However, the fact that chorus wave excitation appears to occur in association with the flux reaching the Kennel-Petschek limit does not necessarily imply that such waves are always the cause of the acceleration which drives the fluxes up

to the Kennel-Petschek limit in the first place. For example, and in contrast to the Reeves et al. conclusion that local acceleration by chorus waves explained the flux enhancement for the October 2012 storm, the data for the March 2015 storm presented in Figure 5.2 are also limited by the Kennel-Petschek process. However, the March 2015 storm is one where the dominant acceleration has been associated with inwards radial diffusion instead. Indeed, *Ozeke et al.* (2019) show that for the March 2015 event inward radial diffusion driven by observed ultra-low frequency (ULF) wave power can accurately reproduce the observed increases in flux (*Ozeke et al.*, 2019).

In our view, the action of the Kennel-Petschek process to limit maximum relativistic electron flux is likely agnostic to the process or processes which accelerated the relativistic electron population to that limit in any particular storm in the first place, whether those processes involve chorus acceleration, ULF wave radial diffusion, or other mechanisms. Of course, once the fluxes reach the Kennel-Petschek limit in any energy channel the action of self-organized excitation of chorus waves appears to act to prevent any further increase of fluxes beyond this theoretical maximum in that channel. The above conclusions are summarized in Figure 5.5 which shows schematically the temporal progression of storm time electron flux, and where flux enhancement is capped once the relativistic electron flux reaches the Kennel-Petschek limit.

The potential impacts of the electron cyclotron waves excited by the Kennel-Petschek process at lower energies on electrons at higher energies also remain to be determined. Certainly, the results presented here suggest that strong radiation belt acceleration events should be associated with the generation of electron cyclotron waves in the inner magnetosphere, for example when the low energy particles hit the Kennel-Petschek limit. Associations between the occurrence of chorus waves and strong radiation belt enhancements have been noted previously. For example, *Li et al.* (2015) noted such an observational relationship, suggesting that the chorus waves were the causal agent explaining the relativistic electron acceleration. However, as noted in subsequent work by *Dimitrakoudis and Mann* (2019), those same intense radiation belt enhancement events can be equally distinguished based on the observed ULF wave power,

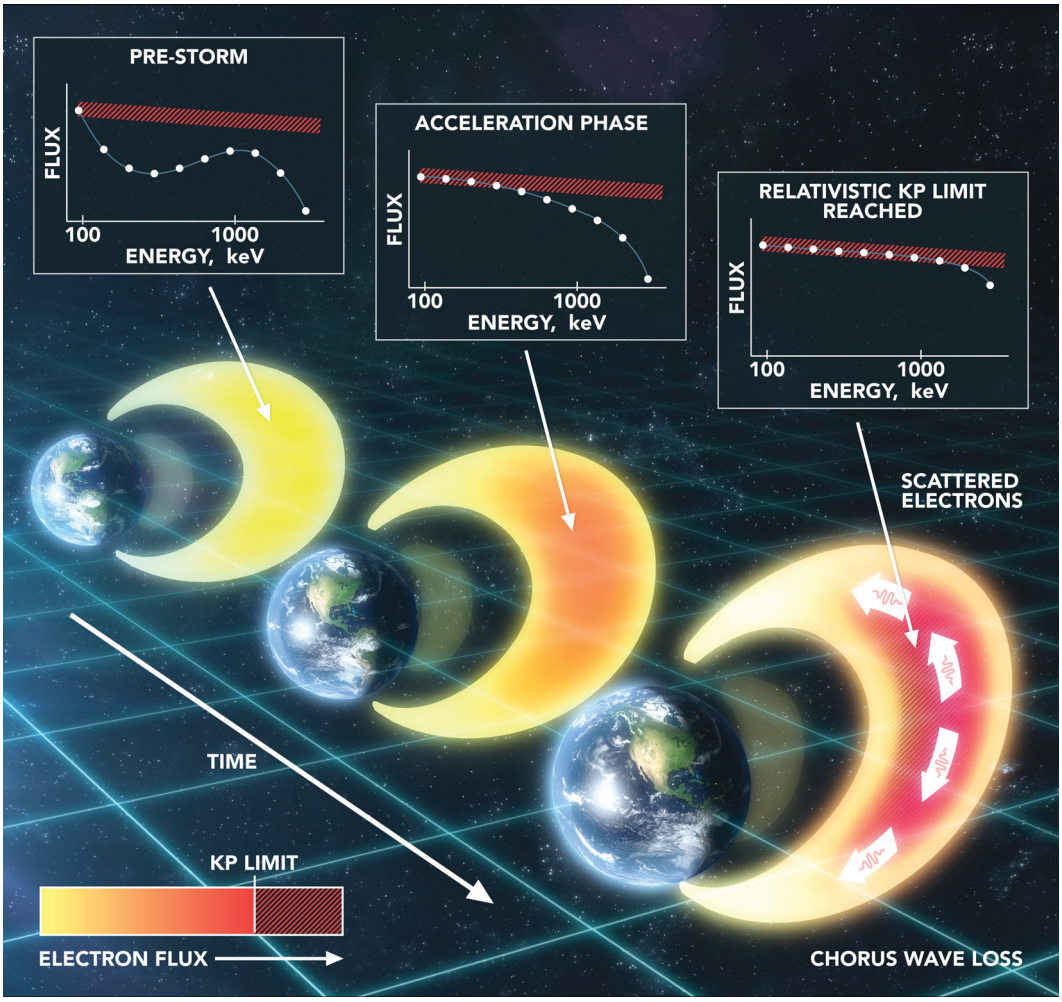

Figure 5.5: Schematic of the time series of electron space radiation reaching its natural limits as defined by the Kennel-Petschek (KP) theory. The figure shows three distinct states of the relativistic electron population inside the Van Allen radiation belts of the Earth during the period of relativistic electron flux enhancement in a geomagnetic storm. The pre-storm phase, with a characteristic S-shaped spectrum, is interrupted by the storm onset that is associated with an initial loss of relativistic electrons which is followed later by an enhancement. The low energy electron population is accelerated to reach the Kennel-Petschek limit first. The higher energies follow later generating an energy spectra with a spectral knee which moves to higher energies over time. Notably, the limiting of the flux levels by the Kennel-Petschek theory is likely independent of the processes which accelerated the electrons to that limit. Nonetheless, as soon as the characteristic Kennel-Petschek levels are reached, the self-organized generation of chorus waves prevents any further increase of fluxes beyond this theoretical maximum. Image credit: Andy Kale `akale@ualberta.ca`

with electron acceleration events also occurring in association with intense ULF waves. Overall, our results imply a potential further complication when trying to identify causality in acceleration pathways.

It is also worthwhile to compare the calculated Kennel-Petschek limits with other historical maxima in relativistic electron flux. During the whole Van Allen Probes era, the maximum flux at L^*=4.25 for the 1.8 MeV energy electron population is $1.9{\cdot}10^4$ $cm^{-2}s^{-1}sr^{-1}keV^{-1}$ on October 27, 2016. Remarkably, the corresponding Kennel-Petschek limit is also $1.9{\cdot}10^4$ $cm^{-2}s^{-1}sr^{-1}keV^{-1}$. Meanwhile, for the 2.6 MeV energy electron population the flux maximum is $3.2{\cdot}10^3$ $cm^{-2}s^{-1}sr^{-1}keV^{-1}$, which also occurs on the same day, with the Kennel-Petschek limit being $2.2{\cdot}10^4$ $cm^{-2}s^{-1}sr^{-1}keV^{-1}$. In other words, at 2.6 MeV the electron flux never reached the Kennel-Petschek limit during the Van Allen Probes era. This result confirms that the limiting flux derived from the Kennel-Petschek theory characterizes the upper limit of the flux of relativistic radiation belt electrons during the Van Allen Probes era, with the electron flux never reaching the Kennel-Petschek limit at energies above 1.8 MeV throughout the entire mission.

Even when comparing to the data from earlier epochs, such as during the Combined Release and Radiation Effects Satellite (CRRES) era from 1990-91 during a much more active solar cycle(*Li et al.*, 2017a), the Kennel-Petschek limit for the relativistic 1472 keV population is above the maximum flux ever measured by CRRES in this channel. For example, $2.4{\cdot}10^3$ $cm^{-2}s^{-1}sr^{-1}keV^{-1}$ was the maximum flux measured by CRRES at L∗=4.25 on March 29, 1991, which can be compared against the theoretical maximum limiting flux of $1.8{\cdot}10^4$ $cm^{-2}s^{-1}sr^{-1}keV^{-1}$. At lower energies, the fluxes seen by CRRES are constrained to maxima at the Kennel-Petschek limit, as was previously shown for a single CRRES pass by *Fox et al.* (2006) and *Mauk and Fox* (2010). For example, *Mauk and Fox* (2010) (their Figure 5) show the electron flux energy spectra from CRRES at *L*-shells 4, 5, and 6 which appear to be consistent with a maximum at the Kennel-Petschek limit for energies below 1 MeV at that instant. Similarly, *Summers et al.* (2009) (their Figure 8) show a similar comparison of the electron flux data from a single pass of CRRES on October

9, 1990, with the data at that instant also apparently showing a maximum at the calculated relativistic Kennel-Petschek limit below 1 MeV. At higher energies above the 1472 keV channel the fluxes remain at least two orders of magnitude below the Kennel-Petschek limit even during the most intense CRRES era storm during this more active solar cycle. Statistical analysis of the radiation environment monitor (IREM) aboard the INTEGRAL spacecraft by *Meredith et al.* (2017) showed evidence for the existence of a limit to the worst case flux at both L^*=4.5 and L^*=6.0, but do not compare their results with the Kennel-Petschek theory. However, as we show here, the energy and L^*-dependence of the maximum flux, and the evolution of the energy spectrum, can both be explained by the Kennel-Petschek theory.

In conclusion, our results use data from the entire Van Allen Probes era to demonstrate the existence of a natural upper limit to the flux of the trapped electron radiation in the Van Allen belts. This limit is created as a result of the natural self-limiting of the flux, arising from a strong scattering of electrons into the atmosphere due to the interaction with chorus plasma waves which are themselves excited from the electron distributions as predicted by *Kennel and Petschek* (1966) over 50 years ago. The relativistic Kennel-Petschek limit, developed by *Summers et al.* (2009), is energy, pitch angle, and L^* dependent. However, for typical electron distributions and parameters appropriate to the geospace environment the variations do not exceed approximately one order of magnitude across the whole of the trapped population of electron radiation. On average, the limiting electron differential flux for relativistic electrons with energies above 500 keV at 90° pitch angles is $\sim 10^4$ $cm^{-2}s^{-1}sr^{-1}keV^{-1}$. In the modern satellite era, the relativistic populations with energies $<\sim$2.6 MeV only reached the Kennel-Petschek limit during the most intense geomagnetic storms. Meanwhile, higher energy fluxes have always stayed below the limit in the Van Allen Probes' era. Verification as to whether the Kennel-Petschek limit applies at even higher energies would require observations during even more intense radiation storms.

Overall, our results have important applications for limiting the potential damage that relativistic and strongly relativistic electron populations can cause

to satellite electronics through deep-dielectric charging during space storms (*Baker et al.*, 1994; *Lai*, 2003; *Catani and Payan*, 2004). Our results imply that the relativistic Kennel-Petschek limit represents a true worst case electron radiation environment that can be used for example in radiation-tolerant satellite design. Even during extreme storms, for example of the size of the Carrington 1859 superstorm event (*Tsurutani*, 2003), our results suggest that the electron radiation fluxes would at worst still be limited to the Kennel-Petschek limit. Space storms of the intensity of the Carrington event have however yet to occur in the modern satellite era. Nonetheless, even if the flux is capped at the Kennel-Petschek limit, the length of the storm would still impact the integrated deep charging effects. However, if the duration of even the most extreme storms is limited to that of typical events, then nature will also limit the worst case fluence as well through the self-organizing process described by *Kennel and Petschek* (1966). As a result, there is a limit to the severity of the electron radiation which can be driven in geospace, nature preventing the development of conditions which are more severe than that. As discussed by *Mauk and Fox* (2010), similar flux limitations likely apply in the radiation belts of the other magnetized planets as well.

Chapter 6

On the Formation of Phantom Electron Phase Space Density Peaks in Single Spacecraft Radiation Belt Data

Based on *Olifer et al.* (2021c) On the formation of phantom electron phase space density peaks in single spacecraft radiation belt data, *Geophysical Research Letters*, 48 (11), doi:10.1029/2020gl092351. The paper was reformated to fit thesis formatting guidelines without any changes to its content.

This chapter examines the rapid losses and acceleration of trapped relativistic and ultrarelativistic electron populations in the Van Allen radiation belt during the September 7-9, 2017, geomagnetic storm. By analyzing the dynamics of the last closed drift shell (LCDS) and the electron flux and phase space density (PSD), we show that the electron dropouts are consistent with magnetopause shadowing and outward radial diffusion to the compressed LCDS. During the recovery phase an in-bound pass of Van Allen Probe A shows an apparent local peak in PSD, but which does not exist. A careful analysis of the multipoint measurements by the Van Allen Probes reveals instead how the apparent PSD peak arises from aliasing monotonic PSD profiles which are rapidly increasing due to acceleration from very fast inwards radial diffusion. In the absence of such multi-satellite conjunctions during fast acceleration events, such peaks might otherwise be associated with local acceleration processes.

6.1 Introduction

Since the discovery of the terrestrially trapped electron radiation in the Van Allen radiation belts (*Van Allen and Frank*, 1959), understanding the processes which govern belt dynamics has remained an active area of research (see e.g., the review by *Millan and Thorne*, 2007, and references therein). A lot of attention has been dedicated to examining the underlying physics of the plasma wave-particle interactions inside the Earth's magnetosphere in pursuit of developing accurate simulation models and potentially predicting Van Allen belt behavior (e.g., *Shprits et al.*, 2008b,a). The processes that cause particle loss and acceleration are those which attract the most attention since in combination they can cause the radiation belt to change drastically on drastically different timescales, ranging from minutes to days and years (e.g., *Mauk et al.*, 2012; *Jaynes et al.*, 2018). The NASA Van Allen Probes mission has collected radiation belt data with unrivaled quality and resolution over its seven years of continuous operation. This mission allowed for the most detailed and complete assessment of radiation belt dynamics to date, and has resulted in multiple ground-breaking discoveries (to list a few *Reeves et al.*, 2013; *Mann et al.*, 2013; *Baker et al.*, 2014; *Mann et al.*, 2016; *Li and Hudson*, 2019). However, assessing radiation belt dynamics on timescales shorter than the orbital period of the Van Allen Probes is challenging due to the lack of high spatio-temporal coverage of a rapidly evolving belt even with the twin Van Allen belt spacecraft.

In this chapter, we analyze a geomagnetic storm that occurred on September 7-9, 2017, and was characterized by an extremely fast radiation belt dropout, followed by a very fast and intense recovery ultimately associated with energization up to ∼10 MeV energies. In addition to explaining the radiation belt dynamics during this event, we show how utilizing the data from a single satellite mission, illustrated here using data from a single Van Allen Probe, can cause misinterpretation of the data during events with fast belt changes on sub-orbital timescales. We show how an apparent local peak in electron phase space density (PSD) observed along the orbit of a single satellite can be caused

by the evolution of a monotonic PSD profile generated by fast inwards radial diffusion. We characterize such a PSD morphology as a "phantom peak" as it exists in appearance only. We are able to disentangle this spatial-temporal ambiguity using multi-point measurements from the two Van Allen Probe spacecraft during this period of very fast acceleration.

6.2 Overview of the September 2017 storm

The overview of the September 2017 storm shown in Figure 6.1 demonstrates that it was a relatively intense geomagnetic storm. It was associated with two periods of decreasing Dst, reaching -142 nT and then -124 nT separated by around 12 hours (cf. Figure 6.1(d)). Figure 6.1(a-c) show solar wind speed, interplanetary magnetic field (IMF), and solar wind dynamic pressure throughout the storm. These plots reveal that the geomagnetic storm started on September 7, 2017, at around 00 UT with an intense increase in the solar wind speed and dynamic pressure and with the southward component of the IMF reaching a minimum of around -10 nT over the next several hours. At around 22 UT on September 7, the IMF turned very strongly southward, reaching the value of -31 nT by 24 UT. This period of strongly southward IMF is also associated with a secondary increase in solar wind speed and dynamic pressure. Finally, at around 12 UT on September 8, there is a secondary decrease in IMF B_z but no substantial changes in other solar wind parameters. Figure 6.1(d) shows the resulting Dst and Kp geomagnetic indices, that are consistent with the characteristics of the driving solar wind, marking the beginning of the storm with an increase in Dst on September 7, and with two subsequent geomagnetically active periods on September 8. Figure 6.1(e) shows the location of the last closed drift shell (LCDS), representative of the interaction of the LCDS with the magnetopause (cf., *Olifer et al.*, 2018). The LCDS dynamics are relatively complex during this event, however, the most significant compressions of the LCDS occurred during the two IMF $B_z < 0$ periods on September 8, reaching L^* values as low as 3.9 and 4.3, respectively.

Figure 6.1(f, g) shows the Van Allen radiation belt response during the

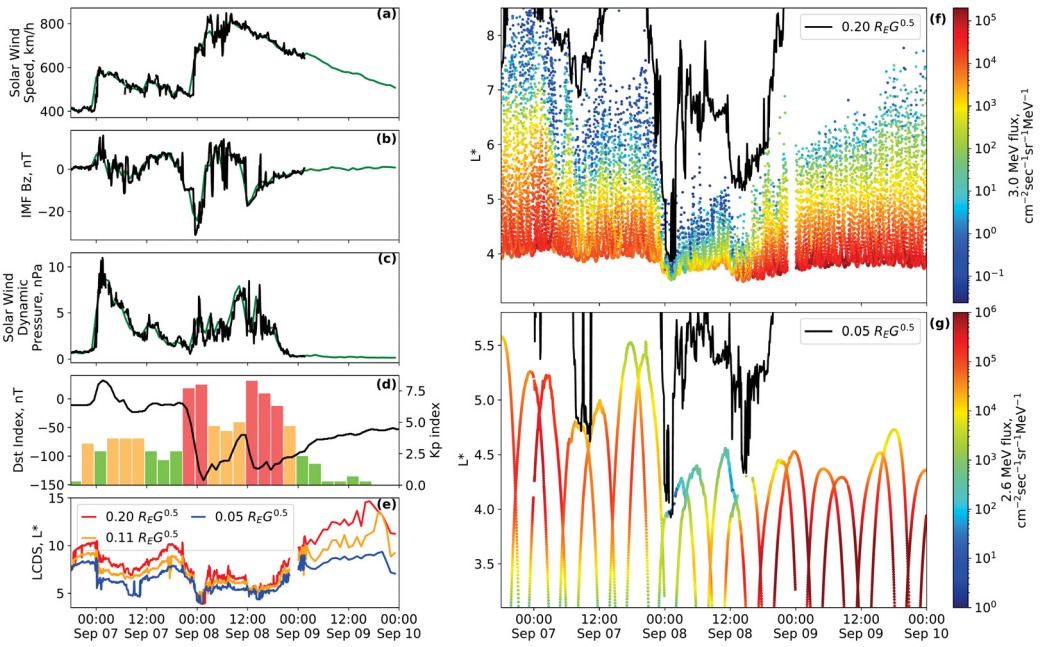

Figure 6.1: An overview of the September 7-9, 2017 geomagnetic storm. (a) solar wind speed, (b) B_z component of the interplanetary magnetic field, (c) solar wind dynamic pressure (5-min data in black, and 1-hr resolution data in green). High-resolution solar wind data is absent for the majority of September 9. (d) Dst index as a line plot and Kp index as a histogram (secondary y-axis). (e) Location of the last closed drift shell (LCDS) in L^* calculated for three different second adiabatic invariants, K, shown in different colours defined in the legend using *Tsyganenko and Sitnov* (2005) geomagnetic model and the LANLGeoMag library (*Henderson et al.*, 2017). (f) 3 MeV electron flux measured by the constellation of Global Positioning System (GPS) satellites (*Morley et al.*, 2017) as a function of time and L^*, overplotted with the LCDS in black. (g) 90° pitch angle 2.6 MeV electron flux measured by the Van Allen Probes (*Baker et al.*, 2012) overplotted with the LCDS.

September 2017 event. In this study, we analyze radiation belt electron flux measurements from the Combined X-ray Dosimeter (*Morley et al.*, 2017, and references therein) on-board 21 Global Positioning System (GPS) satellites (Figure 6.1(f)), as well as from the Relativistic Electron Proton Telescope (REPT) instrument (*Baker et al.*, 2012) on board of the two Van Allen Probes (Figure 6.1(g)). Both datasets show similar storm-time behavior of the trapped radiation, data from the constellation of GPS satellites revealing the electron dynamics with much higher spatio-temporal resolution than the Van Allen Probes (e.g., *Olifer et al.*, 2018, and references therein).

Figure 6.1(f) shows that the beginning of the storm at 3 UT on September 7 is followed by moderate loss at high L^*, and confinement of the radiation belt to $L^*<5.5$. Figure 6.1(g) shows evidence that 2.6 MeV electrons at lower L^* in the heart of the radiation belt are depleted by almost an order of magnitude at this time as well. The strong compression of the LCDS below $L^*=4$ at around 0 UT on September 8 is associated with rapid and intense losses at L^* above the LCDS as revealed in the GPS data, and which are obvious in two subsequent passes of the Van Allen Probes data around that time. The recovery and the replenishment of the belt starts immediately after the loss at $\sim$3 UT on the same day. However, it is interrupted by a second geomagnetically active period at around 12 UT on September 8 that causes some of the newly recovered electron population at L^* around 4-5 to be lost. This period is also associated with the second drop in Dst to -125 nT and the second period of strongly southward IMF B_z reaching -18 nT, increased Kp, and compression of the LCDS (c.f., Figure 1). After the second loss period, the recovery process continues uninterrupted until the radiation belt fluxes reach the pre-storm levels and even exceed them by an order of magnitude or even more at ultrarelativistic energies $>\sim$2 MeV.

6.3 Detailed analysis of radiation belt loss and recovery

To reveal the non-adiabatic effects of wave-particle interactions on the radiation belt electrons we analyze electron phase space density (PSD) over the course of the storm. The electron PSD is calculated using the algorithm (e.g., *Morley et al.*, 2013) for conversion between electron flux measurements and an estimate of electron PSD. The calculations were performed using the *Tsyganenko and Sitnov* (2005) magnetic field model, utilizing electron flux data from the combination of Magnetic Electron Ion Spectrometer (MagEIS) (*Blake et al.*, 2013) and Relativistic Electron Proton Telescope (REPT) (*Baker et al.*, 2012) particle detectors. Such an approach provides access to a wide energy range of electron flux measurements from ∼100 keV to ∼10 MeV and enables the analysis of a wide range of first and second adiabatic invariants even at high L-shells. We update the *Tsyganenko and Sitnov* (2005) magnetic field model every 30 seconds in order to calculate PSD and only consider periods where the model and measured magnetic field magnitudes agree within 10% (see Supplementary Figures E.8 and E.9). In addition, we used the magnetic field measurements from the Electric and Magnetic Field Instrument Suite and Integrated Science (EMFISIS) suite (*Kletzing et al.*, 2013) to validate the *Tsyganenko and Sitnov* (2005) model used in the calculation of PSD and to calculate the first adiabatic invariant. To obtain the electron PSD as a function of the first adiabatic invariant, μ, we perform fitting of the measured electron energy spectrum by a kappa-distribution (*Mauk and Fox*, 2010), meanwhile, the dependence on the second adiabatic invariant, K, is obtained by linearly interpolating the observed pitch angle distributions to obtain the resolution required. Figure 6.2 shows the resulting electron PSD during the loss phase in panels (a, b) and the recovery phase in panels (c, d) for both Van Allen Probes A and B. Here, for the purposes of the detailed analysis which follows, we separate between the periods of dominant loss and recovery at 2:30 UT on September 8, 2017. This is the time when the GPS electron flux data is starting to show signs of recovery in the ultrarelativistic (>2 MeV) energy

channels around L^* of 3.5.

6.3.1 Loss period

Figure 6.2 (panels a, b) show the PSD profiles as a function of L^* observed during the in- and out-bound passes of the Van Allen Probes during the loss phase of the September 2017 geomagnetic storm. As shown earlier in terms of flux, there are two clear periods of strong and fast loss. The first period starts at ∼6 UT on September 7, 2017, during an initial compression of the LCDS. The electron PSD on both probes shows signs of loss. In particular, Van Allen Probes observe decreases of PSD at high L^* commonly associated with the magnetopause shadowing and resulting outward ULF wave transport (orange to green pass in Figure 3a and blue to orange pass in Figure 3b). Significantly, there are signs of a negative radial PSD gradient developing at that time (e.g., *Li et al.*, 2017b; *Zhao et al.*, 2019). The loss is more pronounced on high L, at $L^*>5$, where the PSD drops by more than an order of magnitude from the pre-storm levels. Meanwhile, in the heart of the radiation belt at $L^*\approx4.5$ the radiation belt appears to be only depleted by a factor of around 2. This loss period is followed by a relatively stable period where the radiation belt morphology remains approximately constant, with little overall depletion or recovery, until 0 UT on September 8, 2017. At that time, the LCDS is rapidly compressed into the heart of the radiation belt, reaching $L^*=3.9$. This immediately depletes the electrons at higher L-shells and results in a further very rapid loss, which reaches L^* of around 3.5, and which further depletes the PSD at L^* of around 4.5 by 2-3 orders of magnitude. Notably, the outbound pass of the Van Allen Probe B at 21:52-02:23 UT on September 7-8 (brown color in Figure 6.2b) shows that a steep negative radial gradient has developed along the depleted flux tubes above $L^*=3.8$. The subsequent pass of Van Allen Probe A at 00:55-05:23 UT on September 8 (pink color in Figure 3a) shows how this gradient is flattened by depletion of the PSD between L^* of 3.5 and 4.0. Such behavior of the radiation belt is consistent with losses caused by magnetopause shadowing and enhanced by outward radial diffusion. The timing of the losses, and the PSD profiles observed by Van Allen Probes A and

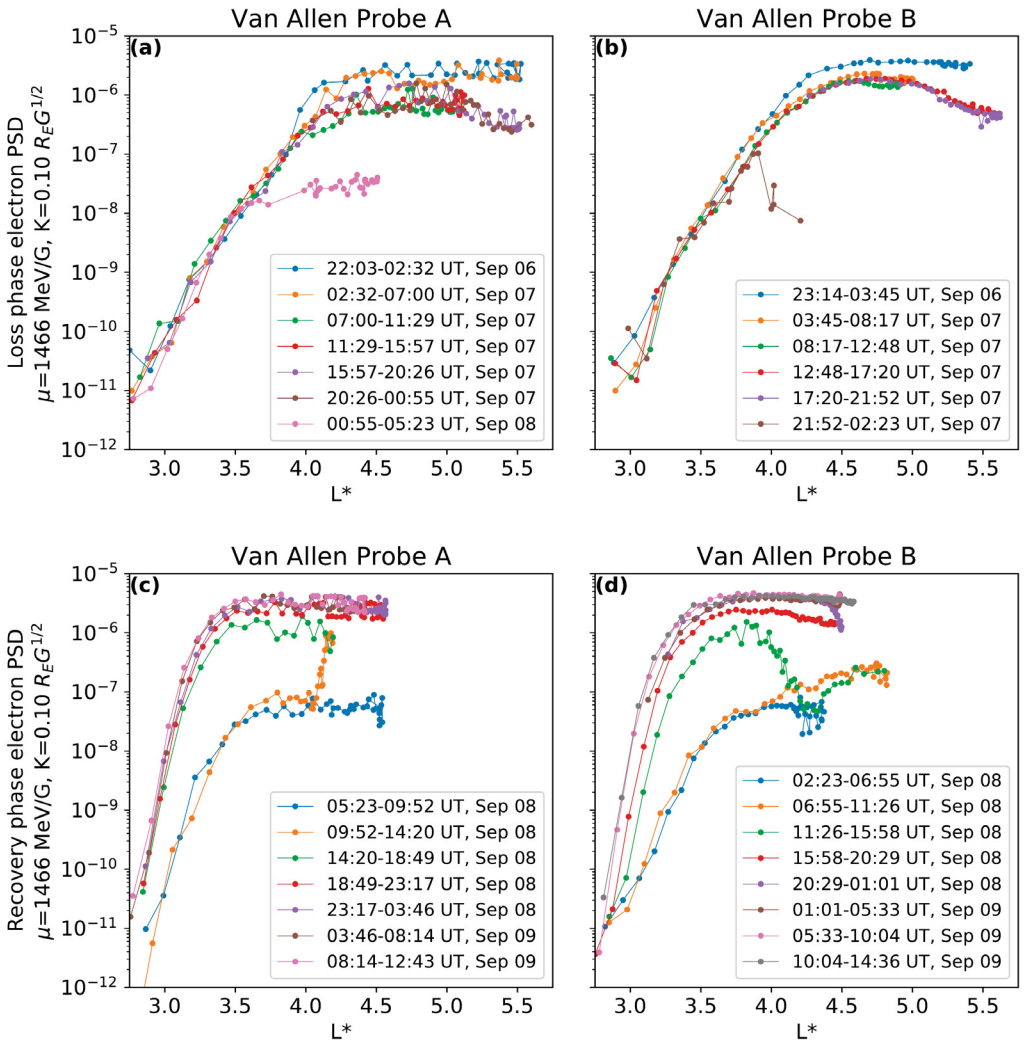

Figure 6.2: Electron phase space density (PSD) as a function of L^*, for fixed μ=1466 MeV/G and K=0.10 $R_E G^{1/2}$. During the pre-storm period, on September 6, this corresponds to energy ∼2.5 MeV at ∼70 degrees equatorial pitch angle at L^*= 4.0. PSD during the loss phase for Van Allen Probe A (panel a) and B (panel b). Different colors represent different inbound and outbound passes of the probes. PSD during the recovery phase for the Van Allen Probe A (panel c) and B (panel d). See text for details.

B, occur at the time of the inwards motion of the LCDS, with the developnment of negative radial PSD gradients further supportive of outwards radial diffusion inside the LCDS (e.g., *Shprits et al.*, 2008b; *Mann et al.*, 2016; *Zhao et al.*, 2019; *Ozeke et al.*, 2020).

The loss on September 8, 2017, is so intense that it depletes the radiation belt over the course of a single Van Allen Probe orbit. By contrast, however, the accompanying spatio-temporal dynamics are resolved in the combined data from the GPS satellite constellation (cf. Figure 6.1f). Overall, the large scale morphology of the radiation belts follows the dynamics of the LCDS. In this way, the results presented here are very similar to those reported by *Olifer et al.* (2018). Olifer et al. assessed the belt dynamics during 4 geomagnetic storms and demonstrated that the very fast and intense losses were associated very closely with the dynamics of the LCDS. Consistent with the conclusions of *Olifer et al.* (2018), the dynamics of the fast loss processes reported here also appear to be controlled by the dynamics of the envelope of the L^* of the LCDS and related magnetopause shadowing. Due to the speed of the loss processes which are operating, the results presented here again demonstrate the value and utility of using data from the constellation of GPS satellites to monitor and diagnose the resulting impacts on the belts.

6.3.2 Recovery and Acceleration Period

We now turn to examine the belt dynamics during the period of belt recovery and dominant acceleration starting around 02:30 UT on September 9, 2017. Unlike the dynamics resolved during the loss interval, the PSD data from the two Van Allen Probes (Figure 6.2, panels c and d) shows rather different behavior along the in- and out-bound satellite passes during this period of dominant acceleration. As we describe in detail below, the different profiles observed by Van Allen Probes A and B demonstrate that the belt morphology is changing very rapidly on the timescale of the satellite traversal through the outer belt. Moreover, a fortuitous conjunction in L^* and time provides the opportunity to resolve the spatio-temporal ambiguity thereby revealing important information about the active acceleration processes. The local peak

in PSD seen by Probe B (11:26-15:58 UT, shown in green in Figure 6.2d) is confined to the L^* range between 3 and 4.25 and such features and belt morphology are usually considered to be suggestive of the signature of local acceleration processes, for example, connected to acceleration by VLF chorus waves (see e.g., *Horne et al.*, 2007; *Shprits et al.*, 2008a; *Reeves et al.*, 2013). However, the observation of a narrow peak in L^* by one probe at the same time as the other probe reveals the increase of PSD at the outer boundary (09:52-14:20 UT, shown in orange in Figure 3c) raises a question about the dominant acceleration processes which are active at this time. In particular, in the analysis presented below, we show how this apparent local peak in PSD can be explained by inward radial transport acting on timescales shorter than the orbital period of Van Allen Probes. This phantom peak is created by a spatio-temporal ambiguity in the PSD data as a function of L^* and time as a result of the orbital motion of the spacecraft during a period of fast acceleration.

Indeed, when combined, the PSD data from Van Allen Probes A and B during the most intense period of the enhancement phase (10-16 UT on September 8, orange and green passes in Figure 3 c and d) reveal that the overall belt evolution is characterized by rapidly evolving positive radial gradients, apparently driven by an external source. Figure 6.3 shows combined PSD data from both probes during the interval of close conjunction in L^*, at fixed first and second adiabatic invariants, μ and K. In each panel, data from the out-bound Probe A and the in-bound Probe B are shown in orange and pink, respectively. Data from passes immediately before and after the fast acceleration are shown as gray dots. The near-simultaneous electron population measurements allows a calculation of the direction of the PSD gradients during the enhancement phase, almost contemporaneously, provided that both probes are located inside the radiation belt with different values of L^*. These gradients are shown with three straight lines connecting data from the two Van Allen Probes at the same time, revealing the local direction of the instantaneous inferred PSD gradient at those times. Note that the profiles are only shown for the period from 13:00 UT until 13:20 UT, as at other times one of the probes is close to the magnetopause and the *Tsyganenko and Sitnov* (2005)

magnetic field model fails to recreate the observed magnetic field at the satellite location, therefore preventing accurate analysis of the PSD as a function of L^* at fixed K. Refer to the Appendix C and Supplementary Figure E.10 for the comparison of the magnetic field measurements from the Van Allen Probes and estimating the location of the magnetopause using the THEMIS (*Angelopoulos*, 2008) satellites. Nonetheless, the analysis of the PSD dynamics is clear – there is an abrupt and very fast acceleration of the electrons associated with steep instantaneous PSD gradients, both inside and outside the probe conjunction region at $L^*\sim3.75$, indicative of acceleration which occurred as a result of fast inwards transport. In the next section, we use a ULF wave radial diffusion model to demonstrate clearly that inward ULF wave radial diffussion caused the rapid acceleration observed in the belt.

6.4 Recreating a phantom local peak in electron PSD by inward radial diffusion

On account of the observed instantaneous positive radial PSD gradients, it is interesting to evaluate the ability of the radial diffusion to recreate the local peak in electron PSD observed in the Van Allen Probe B data. We perform a radial diffusion simulation using initial conditions from the observed pre-acceleration Van Allen probe flux (e.g., lower grey PSD profile in Figure 6.3), using radial diffusion coefficients from the *Ozeke et al.* (2014) Kp parametrization. The boundary conditions are shown in Supplementary Figure E.11 and represent a short loss period, observed by Van Allen Probe B from 11:30 UT until 12:00 UT, which coincides with the inward motion of the LCDS, followed by a sharp assumed enhancement of the outer boundary electron population which acts as a source population for the subsequent inwards radial diffusion. Figure 6.4 shows the instantaneous PSD profiles as a function of L^*, obtained from the radial diffusion simulation, as well as a PSD profile observed by a virtual spacecraft within the simulation domain and which is representative of Van Allen Probe B accounting for its orbital dynamics during the inbound pass. Note that similar behavior is observed for electrons with different μ (cf.

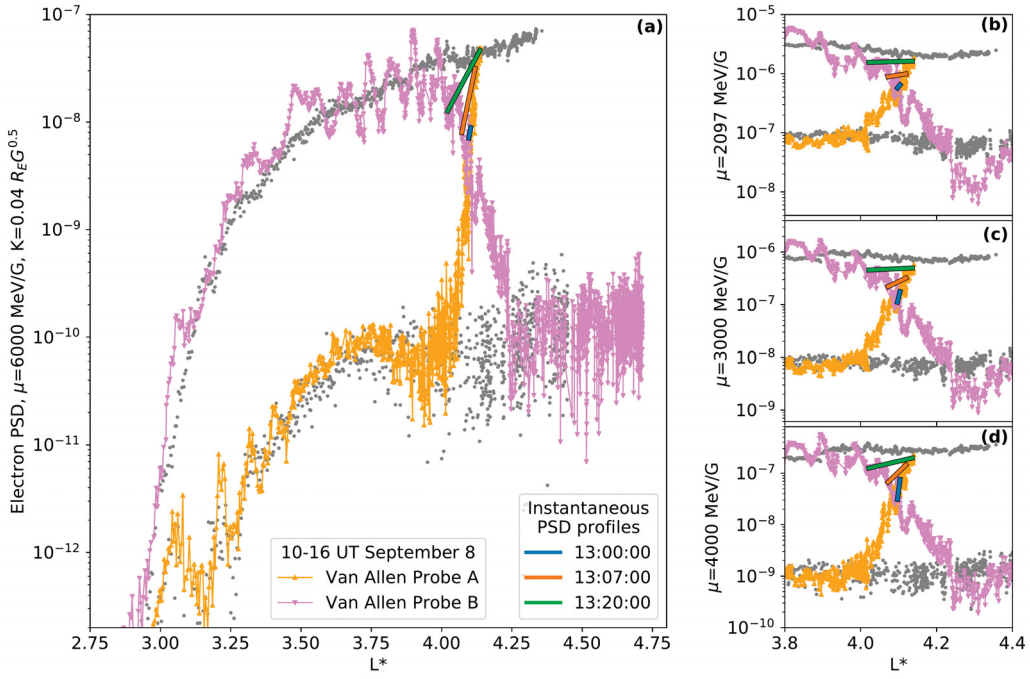

Figure 6.3: (a) Electron PSD along complete in-bound (pink; Probe B) and out-bound (orange; Probe A) passes for μ=6000 MeV/G and K=0.04 $R_E G^{0.5}$. At the time of the conjunction, at L^*=4.0, this corresponds to electron energy of 2.5 MeV and 75° pitch angle. PSD profiles immediately before and immediately after the acceleration are shown in gray scatter plots. Instantaneous local PSD gradients are shown with straight lines connecting data from close to the orbital crossing point in L^* using 20 minutes of data from 13:00 to 13:20 UT. (b-d) PSD profiles as a function of L^* for three other μ values and fixed K=0.04 $R_E G^{0.5}$, in the same format as panel (a).

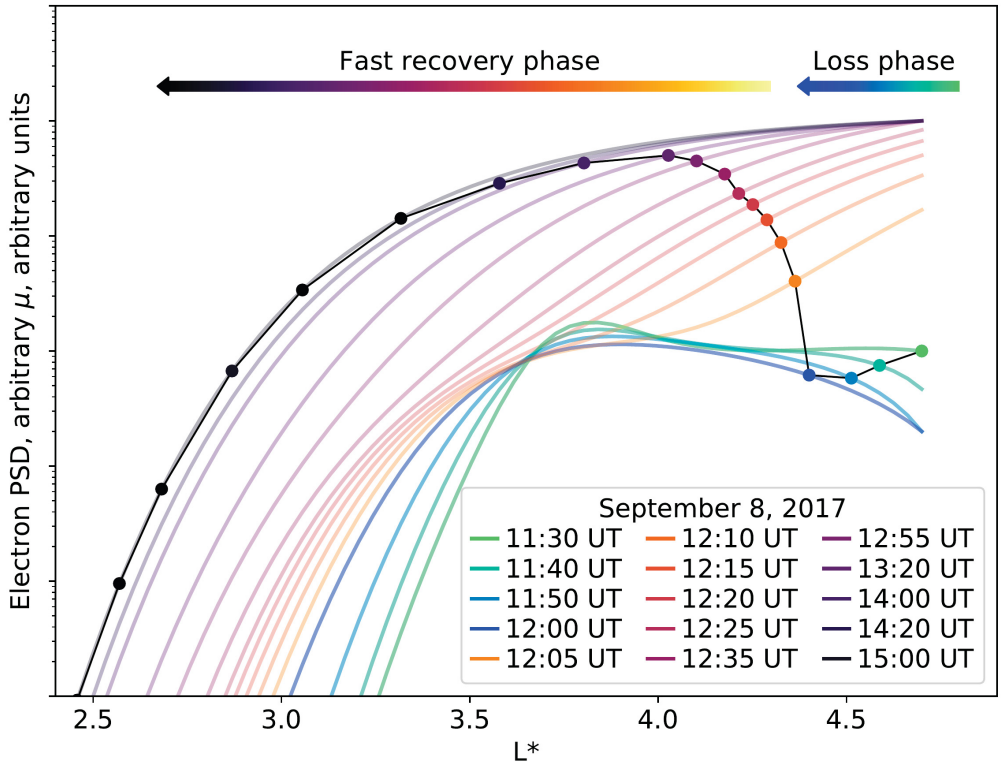

Figure 6.4: Electron phase space density (PSD) profiles as a function of L^* obtained from the radial diffusion simulation of the acceleration phase during September 8, 2017, with measurements from the inbound pass of a virtual Probe B through the simulation shown in solid circles. Colors indicate the time sequence of the simulation PSD profiles, the virtual satellite seeing an apparent local peak in PSD. See text for details.

Figure 6.3), thus the simulation results in Figure 6.4 are representative of the relativistic electron population overall.

Figure 6.4 shows the overall temporal evolution of the electron PSD L^* profile inside the Van Allen radiation belt over the course of the event. PSD profiles during the short loss phase (11:30-12:00 UT) at the beginning of the Van Allen Probe B pass are shown in green-to-blue colors. This time coincides with the time of increased geomagnetic activity and a short compression of the LCDS (c.f., Figure 6.1). Figure 6.3 reveals the loss and a decreasing PSD as Probe B moves inbound from apogee. The same rapid drop in PSD is recreated in Figure 6.4, showing that the negative radial PSD gradient at L^*>4.25, revealed by Van Allen Probe B, is consistent with outward radial

diffusion and magnetopause shadowing. This short loss phase is followed by an intense and rapid acceleration on ∼20 min timescale, which is much shorter than the orbital period of the spacecraft (post 12:00 UT). Figure 6.4 shows the radial PSD profiles during this time in yellow-to-orange-to-purple colors. While the PSD gradients for instantaneous L^* profiles remain directed inward, the orbital movement of Probe B causes it to observe an apparent local L^* peak while the satellite continues its inbound pass and observes levels of PSD which are still increasing. The key point here is that when the belts are evolving under the action of fast acceleration processes, the observation of a single, and not growing, local L^* peak in PSD should not necessarily be automatically associated with a local acceleration process. Indeed, in the example presented here a fortuitous temporal and L^* conjunction between Van Allen Probes A and B reveals that the local L^* peak in PSD is instead generated by the inward motion of the satellite through rising but monotonic PSD L^* profiles as a result of fast inward radial diffusion. Notably and as discussed by *Mann and Ozeke* (2016) (see also *Mann et al.*, 2016), ULF wave radial diffusion can be responsible for the inward radial transport of Van Allen belt elections from a source population at the outer edge into the heart of the belt on timescales much faster than is often thought. As we show here, this can occur on sufficiently short timescales that it complicates the analysis of PSD profiles observed along the trajectory of single satellites in geosynchronous transfer orbits.

6.5 Conclusions

Overall, our findings when analyzing the loss and acceleration of Van Allen radiation belt electrons during the intense geomagnetic storm on September 7-9, 2017 can be summarized by the following points:

1. Analysis of multi-spacecraft electron phase space density (PSD) and high temporal resolution dynamics of the last closed drift shell (LCDS) demonstrates that the observed fast losses can be explained by magnetopause shadowing losses enhanced by outward radial diffusion.

2. An apparent local L^* peak in PSD is observed during the subsequent in-bound pass of Van Allen Probe B during the storm acceleration phase. However, an outbound pass of Van Allen Probe A, at the same time and in conjunction with Probe B, observed a totally different PSD profile as a function of L^* being characterized by a positive radial gradient. A combination of the Van Allen Probes A and B PSD data reveals instantaneous PSD profiles with positive gradients, suggestive of the action of fast inward radial diffusion.

3. A radial diffusion simulation of the acceleration phase during the September 2017 storm shows that the local peak in PSD, observed in the Van Allen Probe B data, is an artifact of the spatio-temporal evolution of the radiation belt, combined with a relatively long orbital period of the satellite.

4. In general, our study shows that the observation of a single local peak in PSD cannot be used to definitively identify the acceleration process that was the cause of the observed radiation belt enhancement, especially during periods of very fast dynamics. While growing local peaks in electron PSD are indicative of the local acceleration, attributing this process as the dominant cause of acceleration in presence of only one, however distinct, peak should be handled with care. Although a peak in electron PSD might be observed in single satellite data during periods of very fast local acceleration acting on sub-orbital timescales, as we show here such a peak can also be produced by fast inward radial diffusion. Careful analysis of ideally multi-point data, together with appropriate modeling, are in our view required when seeking to definitively identify the causative physical processes operating during fast radiation belt enhancements.

Chapter 7

Rapid Acceleration Bursts in the Van Allen Radiation Belt

Based on *Olifer et al.* (2022b) Rapid acceleration bursts in the Van Allen radiation belt

This paper has been sent for review in Nature Communications but despite positive technical reviews was rejected by the editor due to its likely generation of only "specialist interest". To be submitted to an alternative discipline-specific journal.

The Van Allen radiation belts contain relativistic and ultrarelativistic electrons trapped in Earth's magnetic field, which are extremely hazardous for satellites and astronauts. Since their discovery over 60 years ago, the electron dynamics during geomagnetic storms have not yet been fully explained, in part due to limitations of standard satellite missions in both orbit and number of spacecraft. Here we overcome these limitations using a recently-released set of measurements from the Global Positioning System constellation and examine an acceleration event on 26 August 2018. We show that the acceleration of relativistic electrons occurs in two distinct bursts, each dominated by a different acceleration mechanism. Our analysis shows that the first burst intensifies the radiation belt by almost two orders of magnitude in two hours, and is consistent with enhanced radial diffusion. The second burst is likely caused by local wave-particle interactions and delivers an order of magnitude increase in approximately 20 minutes. This work demonstrates how distributed,

operational measurements can be used to resolve phenomena not observable with previous capabilities, and that rapid energization of the radiation belt can occur much faster than previously reported.

7.1 Introduction

Electrons can be trapped and accelerated inside Earth's magnetosphere, creating the dynamic radiation belts (*Van Allen and Frank*, 1959; *Friedel et al.*, 2002), where strong acceleration is often associated with geomagnetic storms (*Murphy et al.*, 2020). The dynamics of the trapped relativistic electron population, with energies from hundreds to thousands of kilo-electronvolts (keV), are of practical interest because of their potentially harmful impact on space-based technology and astronauts (*Baker et al.*, 1994; *Baker*, 2001). The radiation belt also provides a natural laboratory for studying the transport and acceleration of charged particles in magnetic fields (*Li et al.*, 2020). However, the processes dominating these dynamics are still hotly debated (*Shprits et al.*, 2018; *Mann et al.*, 2018): Radiation belt electrons can be accelerated by inward radial transport of a new source population due to interaction with ultra-low frequency (ULF) waves; Electrons can be locally accelerated by interaction with chorus waves, energising lower energy electrons (10-100 keV) and enhancing the relativistic population. From 2012 to 2019, radiation belt dynamics were continuously measured by NASA's flagship, twin-satellite, Van Allen Probes (formerly RBSP) mission (*Mauk et al.*, 2012). However, substantial radiation belt acceleration can occur on time scales much shorter than the half-orbit of Van Allen Probes (<4 hours) (*Olifer et al.*, 2021c), limiting the capability of Van Allen Probes to capture the dynamics of the fastest events. For example, analysis of a fortuitously-timed conjunction between the two Van Allen Probes spacecraft showed that inward radial diffusion can increase radiation belt electron flux by more than two orders of magnitude over a ∼30-minute period (*Olifer et al.*, 2021c). That analysis relied on serendipitous phasing of the acceleration and Van Allen Probes' orbits, showing that there is a need for continuous radiation belt monitoring on much shorter timescales to properly

characterise radiation belt dynamics. This letter focuses on demonstrating such a capability using the recently-released, publicly-available energetic particle data from the Global Positioning System (GPS) constellation (*Morley et al.*, 2017).

Determining the dominant physical processes that drive the radiation belt acceleration generally requires analysing the radiation belt content in terms of phase space density (PSD) as a function of three adiabatic invariants (*Schulz and Lanzerotti*, 1974): μ, the magnetic moment; K, associated with particle bounce motion; and L^* (Roederer's generalised L (*Roederer*, 1970)), associated with the drift motion. When expressed in terms of PSD as a function of these adiabatic invariants, changes in the radiation belt population are produced by non-adiabatic processes, with analysis of the radial profile of PSD constraining the mechanism (*Chen et al.*, 2007a). Obtaining PSD requires observations of differential directional electron flux, and while Van Allen Probes has this capability, the mission cannot provide continuous monitoring of a fixed region in L^*. To mitigate this limitation, we determine the PSD using omnidirectional electron flux from the Combined X-Ray Dosimeter (CXD) data onboard 20 GPS satellites and a *Zhao et al.* (2018) model of pitch angle distribution to acquire the directional flux (further details are presented in the Appendix D, with validation of the method presented in Supplementary Figure E.12). This enables continuous investigation of radiation belt dynamics over a wide range of adiabatic invariant coordinates with an unprecedented ∼10-minute resolution. Here we show that this approach can resolve very fast radiation belt acceleration, revealing short timescale dynamics not observable using Van Allen Probes alone.

7.2 Revealing Very Fast Radiation Belt Acceleration with the GPS Constellation

Figure 7.1 shows geomagnetic conditions and the radiation belt response during the August 25-27, 2018 geomagnetic storm. This storm is characterized by prolonged geomagnetic activity, and the Dst index (a measure of storm strength)

reaches a minimum of −174 nT (Figure 7.1a). As seen in Figure 7.1b-c, the storm contains a radiation belt loss period, depleting the relativistic electron flux by almost two orders of magnitude, from around 18 UT on August 25 to 6 UT on August 26. This is followed by rapid, intense acceleration of the belt leading to electron fluxes exceeding pre-storm levels within ∼6 hours. Due to the phasing of their orbits, Van Allen Probes (Figure 7.1b) only observes the pre-acceleration radiation belt at around 6 UT on August 26 and the post-acceleration belt at around 12 UT, completely missing the main portion of the acceleration. On the other hand, the electron flux data from the GPS satellites (Figure 7.1c) clearly show the progression of the acceleration during that time. It is important to note that this substantial undersampling of the acceleration phase by Van Allen Probes is partly caused by undefined L^* due to the proximity to the last closed drift shell (LCDS).

We now cast this in terms of PSD as a function of μ, K and L^*. Figure 7.1d-e show the PSD obtained from the Van Allen Probes and GPS satellites at fixed first and second adiabatic invariants ($\mu = 1466$ MeV/G, $K = 0.10\ R_E G^{0.5}$) as a function of time and L^*. This population corresponds to 1 MeV electrons at $L^* = 3.6$ during the beginning of the acceleration phase. Similar to the flux, the Van Allen Probes PSD data (Figure 7.1d) reveal that the main portion of the acceleration occurs between 6 and 12 UT on August 26, but the temporal evolution is not resolved. On the other hand, the GPS PSD (Figure 7.1e) enables continuous examination of the dynamics within the heart of the radiation belt ($3.5 \leq L^* \leq 4.0$) during the acceleration period. Notably, a significant amount of GPS data at high L^* cannot be converted to PSD(μ,K,L^*) because the selected K are not measured by the GPS satellites at those locations. Nonetheless, Figure 7.1e reveals the acceleration progression in greater detail. The GPS data show that substantial acceleration occurs around 6-8 UT on August 26. After this initial acceleration the PSD stays relatively constant for almost 4 hours, until the secondary acceleration at 12 UT. This is shown more clearly in Figure 7.2 where the evolution in PSD profiles is marked for select intervals. Because the acceleration is rapid, intense, and transient, we refer to these periods of acceleration as "acceleration bursts".

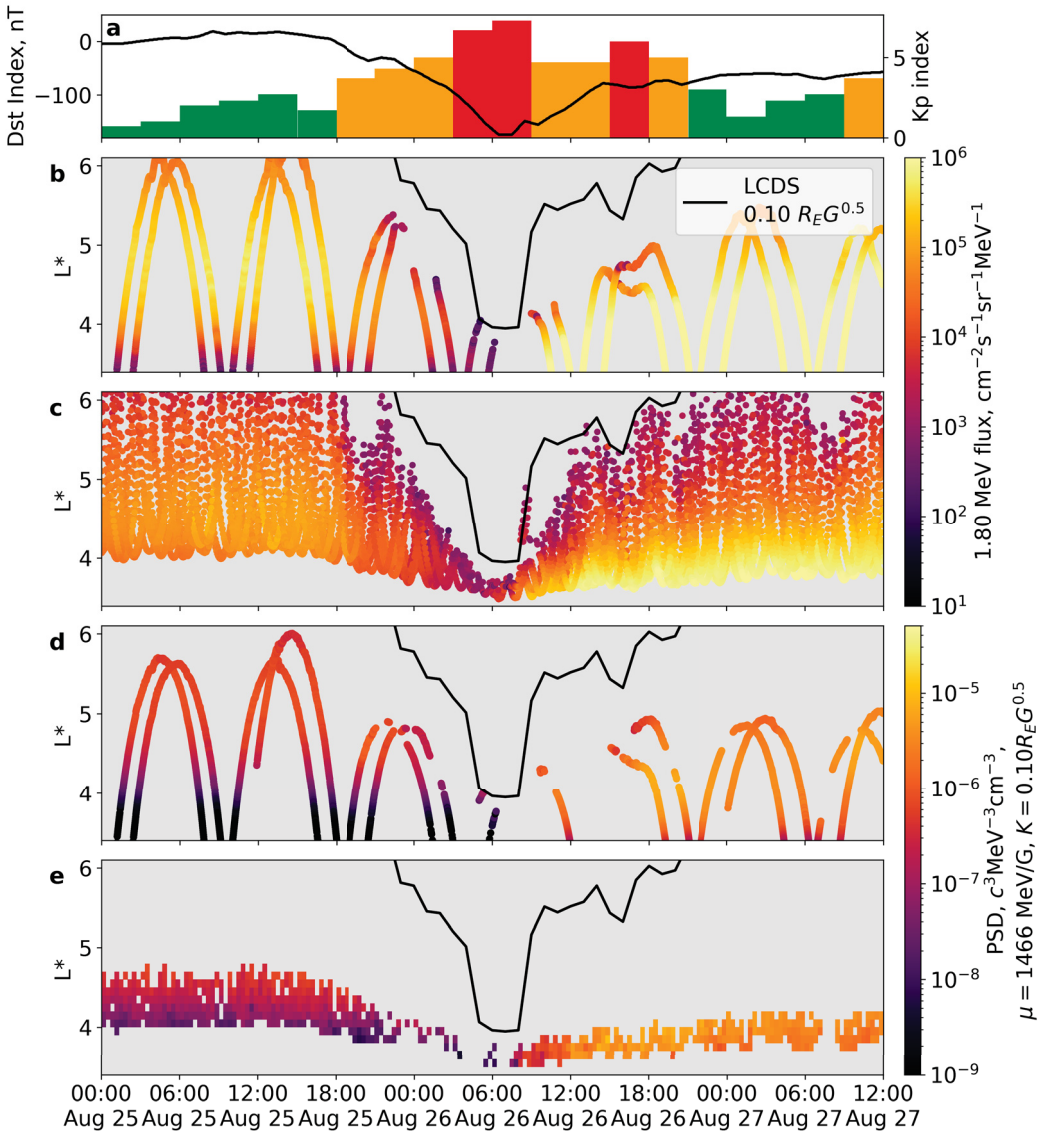

Figure 7.1: Geomagnetic conditions and radiation belt response during the August 2018 geomagnetic storm. **a**, disturbance storm time index, Dst, (line plot, left y-axis) and Planetary K-index, Kp, (histogram plot, right y-axis). **b** and **c** show 1.8 MeV electron flux measurements by the Van Allen Probes and GPS spacecraft respectively, **d** and **e** electron PSD for fixed first and second adiabatic invariants (μ =1466 MeV/G, $K = 0.1\ R_E G^{0.5}$) obtained from the Van Allen Probes and GPS constellation respectively. Panels **b-e** show flux or PSD as a function of time and Roederer L^* parameter (*Roederer*, 1970) calculated for the *Tsyganenko and Sitnov* (2005) magnetic field model. The black lines overlaid on panels **b-e** show the last closed drift shell (c.f, *Albert et al.*, 2018), calculated using the LANLGeoMag (*Henderson et al.*, 2017) library.

Radial profiles of GPS PSD data, shown in Figure 7.2, clearly reveal that the acceleration during the August 2018 storm occurs in two distinct bursts. By contrast, Van Allen Probes only capture the combined effect of the two acceleration bursts. The initial burst starts at around 6:00 UT as revealed by the GPS satellites and lasts for ∼2.5 hours until 8:40 UT. During this time the radiation belt population is gradually increased by almost two orders of magnitude, as revealed by the GPS PSD profiles at 7:40 and 8:00 UT. At this time, both Van Allen Probes are outside the last closed drift shell and do not measure the trapped population. After this initial acceleration burst the radial PSD profiles remain largely unchanged until 11:50 UT, illustrated by non-rising PSD profiles from GPS as well as an inward pass by the RBSP-B at the time of its conjunction with GPS (11:30 UT). Following three hours of stability, a very rapid increase in PSD is observed as the radiation belt electrons are accelerated by almost an order of magnitude over the next 20 minutes. This is highlighted by a sharp increase in GPS PSD profiles from 11:50 to 12:10 UT in Figure 7.2 and confirmed by the subsequent pass by RBSP-B, showing that PSD increases across a wide range of L^*.

We also evaluated the radiation belt dynamics at different energies across this interval. Supplementary Figure E.13 and E.14 show the PSD(L^*) profiles for $\mu = 501$ MeV/G and $\mu = 2508$ MeV/G, for fixed $K = 0.1\ R_E/G^{0.5}$ (in the same format as Figure 7.2). These electron populations correspond to 0.5 MeV and 2 MeV at $L^* = 3.6$ respectively. Supplementary Figure E.14 shows that the acceleration of the 2508 MeV/G electrons progressed in a similar manner to that of 1466 MeV/G, revealing two distinct acceleration bursts around 6 UT and 12 UT on August 26 (cf., Figure 7.2). Supplementary Figure E.13 shows only one acceleration burst for the lower energy population at around 6 UT, consistent with the timing of the first acceleration burst for the two higher energies. After the initial acceleration burst, the lower energy electrons remain approximately constant.

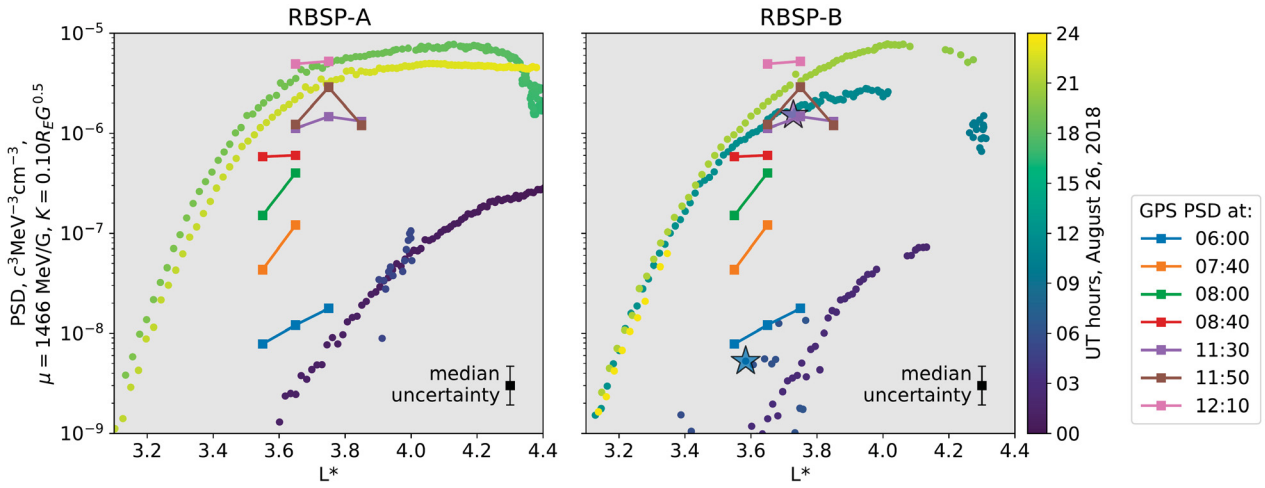

Figure 7.2: Electron phase space density (PSD) profiles during the acceleration phase of the August 2018 geomagnetic storm. The electron PSD profiles obtained from the Van Allen Probes data are shown with a scatter plot in both panels (RBSP-A on the left and RBSP-B on the right). Due to the orbital movement of the spacecraft, the Van Allen Probe PSD are color-coded by UT on August 26, 2018. The PSD profiles evaluated from the GPS satellites are shown with line plots, duplicated in both panels, during the first (06:00-08:40 UT) and second (11:50-12:10 UT) acceleration bursts. The star markers represent the times of conjunction between RBSP-B and GPS at 06:00 UT and 11:30 UT. The median uncertainty indicates size of the median error across all GPS instruments and measurement times (see Methods section for details).

7.3 Probing the Origin of the Acceleration Bursts

To evaluate whether ULF wave radial diffusion is the dominant cause of the radiation belt acceleration during this event, we infer the radial diffusion coefficients, D_{LL}, from the GPS PSD profiles following (*Schulz and Lanzerotti*, 1974) and compare them to the D_{LL} obtained from both ULF wave ground-based observations (*Ozeke et al.*, 2009) and from empirical models (*Ozeke et al.*, 2014; *Lejosne*, 2020). Figure 7.3 shows the obtained D_{LL} during the two acceleration bursts. During the first acceleration burst, the D_{LL} obtained from the GPS PSD are consistent with ground-based observations to within reported levels of variability during storm times (*Olifer et al.*, 2019; *Sandhu et al.*, 2021). The GPS-driven D_{LL} also show a clear structuring in μ, with lower μ (and thus lower energy) having larger D_{LL}. This is consistent with the radial diffusion coefficients obtained from the ground-based ULF wave observations for this event, as well as prior simulation studies (*Li et al.*, 2016, 2017a). Conversely, during the second acceleration burst, the GPS-driven D_{LL} at higher μ (1466 MeV/G and 2508 MeV/G) are more than two orders of magnitude larger than those expected from ground-based observations or empirical models.

The analysis of D_{LL} obtained directly from the GPS PSD (Figure 7.3) clearly shows that only the first acceleration burst is likely to be driven by inward radial diffusion; the second acceleration burst appears inconsistent with radial diffusion as a dominant mechanism. Local acceleration by wave-particle interactions (*Reeves et al.*, 2013) is a likely candidate for the dominant process at that time. Figure 7.4 shows elevated chorus wave activity around the time of the second burst measured by the Onboard Frequency Analyzer (OFA) instrument onboard the Arase spacecraft (*Kasahara et al.*, 2018; *Miyoshi et al.*, 2018; *Matsuoka et al.*, 2018), which itself follows a substorm onset measured at geosynchronous orbit (Supplementary Figure E.15). During the second acceleration burst (c.f., Supplementary Figure E.14), energies above ∼1 MeV are energised significantly, while the lower energy electrons (∼0.5 MeV) are not. Acceleration of predominantly higher energies is consistent with "anchor

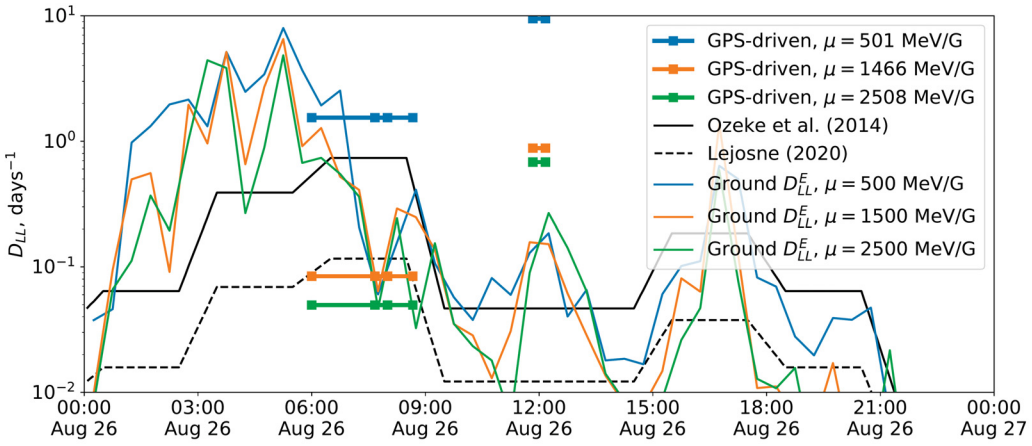

Figure 7.3: Radial diffusion coefficients during the acceleration phase of the August 2018 geomagnetic storm. Radial diffusion coefficients (D_{LL}) derived from the GPS PSD radial profiles are shown with horizontal lines for the first and second acceleration bursts. D_{LL} was calculated separately for three values of the first adiabatic invariant, μ. D_{LL} was estimated by integrating PSD profiles in Figure 7.2 and Supplementary Figure E.13 and E.14 using the approach introduced by *Schulz and Lanzerotti* (1974). For comparison, we also show the electric field component of event-specific radial diffusion coefficients D_{LL}^E, estimated from the network of ground magnetometers and mapping of the horizontal magnetic field component using *Ozeke et al.* (2009) approach. These are shown for the same set of μ by the solid colored lines covering the full span of the plot. The black lines show D_{LL} calculated using the Kp-dependent empirical models of *Ozeke et al.* (2014) (solid line) and *Lejosne* (2020) (dashed line).

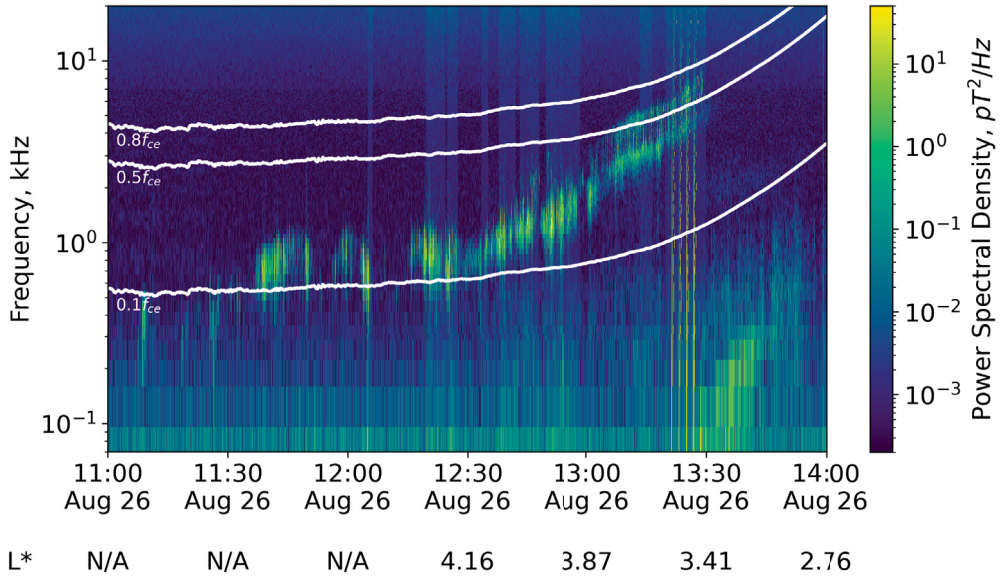

Figure 7.4: Magnetic field power spectral density measured by Arase satellite during the second acceleration burst. Power spectral data is obtained from the Onboard Frequency Analyzer (OFA) instrument and is shown as a function of time and frequency. White lines outline the frequency bands of upper ($0.8f_{ce}$-$0.5f_{ce}$) and lower ($0.5f_{ce}$-$0.1f_{ce}$) chorus, where f_{ce} is the electron cyclotron frequency. The secondary x-axis shows the L^* of Arase satellite for the local 90° pitch angle at the corresponding times. Note that prior to 12 UT the L^* parameter is undefined.

point" theory (*Summers et al.*, 2002; *Horne et al.*, 2005), which states that the lower energy electrons ($<\sim$0.8 MeV) provide the source population for the acceleration while also generating chorus waves, resulting in the acceleration of electrons up to ultra-relativistic energies.

7.4 Conclusions

This study reveals how observations of the Van Allen radiation belt by the GPS constellation can simultaneously provide continuous monitoring, reveal very fast radiation belt dynamics, and enable identification of the dominant physical mechanisms driving them. Although the energetic particle sensors on GPS are operational environment monitors, the large number (> 20) on orbit brings unique scientific capabilities. This is clearly exemplified here using the August 2018 geomagnetic storm. The GPS satellite data reveal a clear separation of the

acceleration into two distinctly different bursts, the first lasting ∼2 hours and the second ∼20 minutes, while Van Allen Probes only measure their combined effect. Without constellation measurements the acceleration would not have been resolved into the two bursts, potentially leading to incorrect physical interpretation.

By calculating radial diffusion coefficients directly from the GPS PSD data, we have shown that inward radial diffusion was a dominant driver of the first acceleration burst that last for two hours, increasing the whole radiation belt population by almost two orders of magnitude. Meanwhile, the second acceleration burst was likely caused by local wave-particle interaction increasing relativistic (>1 MeV) electron PSD by an order of magnitude over 20 minutes. Resolving fast PSD dynamics across an extended interval has previously not been possible, leading to incomplete understanding of rapid radiation belt acceleration. Even as new science missions aim to probe the radiation belts with highly-capable instruments (*Miyoshi et al.*, 2018; *Blum et al.*, 2020), we foresee a critical role for GPS in the future of radiation belt science.

Chapter 8

Thesis Summary and Future Work

The analysis presented in this thesis focuses on investigating the dynamics of the Earth's radiation belt electrons during geomagnetic storms. By performing statistical and event-specific analyses, we have shown in Chapters 3 that the storm-time behavior of various radiation belt populations may be much more repeatable and similar from one storm to the next than previously thought. In particular, during the geomagnetic storms with low values of the last closed drift shell (LCDS) which are expected to be dominated by magnetopause shadowing losses, the relativistic electron population with energies below 600 keV appears to be depleted by the same factor (with respect to the pre-storm conditions) in every studied geomagnetic storm. The fractional amount of the loss depends on energy and location, but it appears repeatable and consistent with the outward loss of particles into the solar wind. This advance promises further improvements to radiation belt loss models, perhaps to be incorporated using empirical methods.

On the other hand, the flux of the lower energy electrons is predominantly enhanced during the beginning of the storm. Importantly and as shown in Chapter 4, it is enhanced to the same level in every storm geomagnetic storm that we investigated in our superposed epoch analysis. This level is energy and location-dependent and is consistent with the theoretical model by *Kennel and Petschek* (1966) that describes a natural maximum flux level in a magnetosphere where any increases in the electron flux are balanced out by the precipitation

loss induced by the chorus wave growth, which in turn depends on the amount of electron flux in the magnetosphere. By additionally analyzing six events with the largest flux of the 2.6 MeV electron population in Chapter 5, we have also shown that the *Kennel and Petschek* (1966) theory may apply to relativistic or strongly relativistic electrons as well. Indeed, the Kennel-Petschek theory elegantly explains the evolution and hardening of the electron spectrum during those geomagnetic storms and defines a natural maximum flux for the terrestrially trapped electron space radiation.

The final part of this thesis in Chapters 6 and 7 also focuses on investigating very fast acceleration processes that may occur in the radiation belts of the Earth. By analyzing the September 2017 geomagnetic storm, in Chapter 6, we showed that an apparent local peak in electron phase space density (PSD), which is classically associated with the local acceleration and which was observed in the PSD data from one of the two Van Allen Probes along its outbound trajectory, does not actually exist. A careful analysis of the multipoint measurements by the Van Allen Probes reveals instead how the apparent PSD peak arises from aliasing monotonic PSD profiles which are rapidly increasing due to acceleration from very fast inwards radial diffusion. If analyses of multi-satellite measurements are not employed in geomagnetic storms with similarly fast acceleration, such measurement artifacts might otherwise be misinterpreted as being representative of, and responsible for, such acceleration.

To resolve such possible misinterpretations in Chapter 7 we have developed for the first time an algorithm for estimating the electron PSD from electron flux data measured by the constellation of Global Positioning System (GPS) satellites. By examining a very fast acceleration event on 26 August 2018, we have shown that the acceleration of relativistic electrons occurred in two distinct bursts, each dominated by a different physical acceleration mechanism. ULF wave radial diffusion seemingly dominated during the first acceleration burst, meanwhile, the second one is likely caused by local acceleration by chorus waves. The analysis that we presented here reveals radiation belt dynamics at an unprecedented 10-minute temporal resolution, which allows

for such very fast dynamics to be resolved for the first time. Our work clearly demonstrates how distributed, measurements can be used to resolve phenomena not readily observable with previous capabilities, and that rapid energization of the radiation belt can occur on timescales much faster than previously reported.

All of the results presented here could be used for the further development of advanced physics-based forecasting models of the near-Earth radiation environment through their incorporation into data drivel models or for the development of improved radiation specification models for designing radiation-hard space infrastructure.

The results presented in this Ph.D. thesis provide a number of avenues for future research. For example, the impact of self-limiting processes on the nature of the dynamics and resulting morphology of the radiation belts, and which appears to be active in almost every geomagnetic storm, demands further investigation. In particular, analyzing data not only from the satellites in the inner magnetosphere but also from low Earth orbit during times of magnetic conjunction between them can provide insight into the role of the Kennel-Petschek limit for driving particle precipitation into the atmosphere. The underlying effects of the resulting enhanced precipitation on the Earth's atmosphere and climate can also be assessed over the course of such a study. Importantly, this topic is also in line with the scientific questions which are to be answered by a number of future international space missions. For example, The Radiation Impacts on Climate and Atmospheric Loss Satellite (RADICALS) mission led by the University of Alberta (launches in 2026-2027) and the NASA Geospace Dynamics Constellation (GDC) mission (launches in 2027) are designed to explicitly address the impacts of radiation and coupling to the Earth's atmosphere arising from the processes in geospace by measuring the electron precipitation and the electron dynamics in the coupled magnetosphere-ionosphere-atmosphere system at previously unseen resolutions.

Bibliography

Akasofu, S. I., and S. Chapman (1973), Solar-terrestrial physics, *Quarterly Journal of the Royal Meteorological Society*, *99*(422), 793–793, doi:10.1002/qj.49709942230.

Albert, J. M., R. S. Selesnick, S. K. Morley, M. G. Henderson, and A. C. Kellerman (2018), Calculation of last closed drift shells for the 2013 GEM radiation belt challenge events, *Journal of Geophysical Research: Space Physics*, doi:10.1029/2018ja025991.

Alken, P., E. Thebault, C. D. Beggan, H. Amit, J. Aubert, J. Baerenzung, T. N. Bondar, W. J. Brown, S. Califf, A. Chambodut, A. Chulliat, G. A. Cox, C. C. Finlay, A. Fournier, N. Gillet, A. Grayver, M. D. Hammer, M. Holschneider, L. Huder, G. Hulot, T. Jager, C. Kloss, M. Korte, W. Kuang, A. Kuvshinov, B. Langlais, J.-M. Leger, V. Lesur, P. W. Livermore, F. J. Lowes, S. Macmillan, W. Magnes, M. Mandea, S. Marsal, J. Matzka, M. C. Metman, T. Minami, A. Morschhauser, J. E. Mound, M. Nair, S. Nakano, N. Olsen, F. J. Pavon-Carrasco, V. G. Petrov, G. Ropp, M. Rother, T. J. Sabaka, S. Sanchez, D. Saturnino, N. R. Schnepf, X. Shen, C. Stolle, A. Tangborn, L. Toffner-Clausen, H. Toh, J. M. Torta, J. Varner, F. Vervelidou, P. Vigneron, I. Wardinski, J. Wicht, A. Woods, Y. Yang, Z. Zeren, and B. Zhou (2021), International geomagnetic reference field: the thirteenth generation, *Earth, Planets and Space*, *73*(1), doi:10.1186/s40623-020-01288-x.

Allison, H. J., and Y. Y. Shprits (2020), Local heating of radiation belt electrons to ultra-relativistic energies, *Nature Communications*, *11*(1), doi:10.1038/s41467-020-18053-z.

Angelopoulos, V. (2008), The THEMIS mission, *Space Science Reviews*, *141*(1-4), 5–34, doi:10.1007/s11214-008-9336-1.

Baker, D. (2000), The occurrence of operational anomalies in spacecraft and their relationship to space weather, *IEEE Transactions on Plasma Science*, *28*(6), 2007–2016, doi:10.1109/27.902228.

Baker, D., R. Belian, P. Higbie, R. Klebesadel, and J. Blake (1987), Deep dielectric charging effects due to high-energy electrons in earth's outer magnetosphere, *Journal of Electrostatics*, *20*(1), 3 – 19, doi:10.1016/0304-3886(87)90082-9.

Baker, D. N. (2001), Satellite anomalies due to space storms, in *Space Storms and Space Weather Hazards*, pp. 285–311, Springer Netherlands, doi:10.1007/978-94-010-0983-6_11.

Baker, D. N., S. Kanekal, J. B. Blake, B. Klecker, and G. Rostoker (1994), Satellite anomalies linked to electron increase in the magnetosphere, *Eos, Transactions American Geophysical Union*, *75*(35), 401–405, doi:10.1029/94EO01038.

Baker, D. N., S. G. Kanekal, X. Li, S. P. Monk, J. Goldstein, and J. L. Burch (2004), An extreme distortion of the Van Allen belt arising from the Halloween solar storm in 2003, *Nature*, *432*, 878.

Baker, D. N., S. G. Kanekal, V. C. Hoxie, S. Batiste, M. Bolton, X. Li, S. R. Elkington, S. Monk, R. Reukauf, S. Steg, J. Westfall, C. Belting, B. Bolton, D. Braun, B. Cervelli, K. Hubbell, M. Kien, S. Knappmiller, S. Wade, B. Lamprecht, K. Stevens, J. Wallace, A. Yehle, H. E. Spence, and R. Friedel (2012), The relativistic electron-proton telescope (REPT) instrument on board the radiation belt storm probes (RBSP) spacecraft: Characterization of earth's radiation belt high-energy particle populations, *Space Science Reviews*, *179*(1-4), 337–381, doi:10.1007/s11214-012-9950-9.

Baker, D. N., A. N. Jaynes, V. C. Hoxie, R. M. Thorne, J. C. Foster, X. Li, J. F. Fennell, J. R. Wygant, S. G. Kanekal, P. J. Erickson, W. Kurth, W. Li, Q. Ma, Q. Schiller, L. Blum, D. M. Malaspina, A. Gerrard, and L. J. Lanzerotti (2014), An impenetrable barrier to ultrarelativistic electrons in the Van Allen radiation belts, *Nature*, *515*(7528), 531–534, doi:10.1038/nature13956.

Baumjohann, W., and R. A. Treumann (1996), *Basic Space Plasma Physics*, Imperial College Press, doi:10.1142/p015.

Bingham, S. T., C. G. Mouikis, L. M. Kistler, A. J. Boyd, K. Paulson, C. J. Farrugia, C. L. Huang, H. E. Spence, S. G. Claudepierre, and C. Kletzing (2018), The outer radiation belt response to the storm time development of seed electrons and chorus wave activity during cme and cir driven storms, *Journal of Geophysical Research: Space Physics*, *123*(12), 10,139–10,157, doi:https://doi.org/10.1029/2018JA025963.

Blake, J. B., P. A. Carranza, S. G. Claudepierre, J. H. Clemmons, W. R. Crain, Y. Dotan, J. F. Fennell, F. H. Fuentes, R. M. Galvan, J. S. George, M. G. Henderson, M. Lalic, A. Y. Lin, M. D. Looper, D. J. Mabry, J. E. Mazur, B. McCarthy, C. Q. Nguyen, T. P. O'Brien, M. A. Perez, M. T. Redding, J. L. Roeder, D. J. Salvaggio, G. A. Sorensen, H. E. Spence, S. Yi, and M. P. Zakrzewski (2013), The magnetic electron ion spectrometer (MagEIS) instruments aboard the radiation belt storm probes (RBSP) spacecraft, *Space Science Reviews*, *179*(1-4), 383–421, doi:10.1007/s11214-013-9991-8.

Blum, L., L. Kepko, D. Turner, C. Gabrielse, A. Jaynes, S. Kanekal, Q. Schiller, J. Espley, D. Sheppard, L. Santos, J. Lucas, and S. West (2020), The GTOSat CubeSat: scientific objectives and instrumentation, in *Micro- and Nanotechnology Sensors, Systems, and Applications XII*, edited by M. S. Islam and T. George, SPIE, doi:10.1117/12.2556268.

Bortnik, J., and R. Thorne (2007), The dual role of ELF/VLF chorus waves in the acceleration and precipitation of radiation belt electrons, *Journal of Atmospheric and Solar-Terrestrial Physics*, *69*(3), 378–386, doi:10.1016/j.jastp.2006.05.030.

Brautigam, D. H., and J. M. Albert (2000), Radial diffusion analysis of outer radiation belt electrons during the october 9, 1990, magnetic storm, *Journal of Geophysical Research: Space Physics*, *105*(A1), 291–309, doi:10.1029/1999ja900344.

Brito, T. V., and S. K. Morley (2017), Improving empirical magnetic field models by fitting to in situ data using an optimized parameter approach, *Space Weather*, *15*(12), 1628–1648, doi:10.1002/2017sw001702.

Carver, M., S. K. Morley, and A. Stricklan (2020), Gps constellation energetic particle measurements, in *2020 IEEE Aerospace Conference*, pp. 1–10, doi:10.1109/AERO47225.2020.9172652.

Catani, J., and D. Payan (2004), Electrostatic behaviour of materials in a charging space environment, in *Proceedings of the 2004 IEEE International Conference on Solid Dielectrics, 2004. ICSD 2004.*, IEEE, doi:10.1109/icsd.2004.1350582.

Chen, Y., G. D. Reeves, and R. H. Friedel (2007a), The energization of relativistic electrons in the outer Van Allen radiation belt, *Nature Physics*, *3*(9), 614–617.

Chen, Y., R. H. W. Friedel, G. D. Reeves, T. E. Cayton, and R. Christensen (2007b), Multisatellite determination of the relativistic electron phase space density at geosynchronous orbit: An integrated investigation during geomagnetic storm times, *Journal of Geophysical Research: Space Physics*, *112*(A11), n/a–n/a, doi:10.1029/2007ja012314.

Claudepierre, S. G., Q. Ma, J. Bortnik, T. P. O'Brien, J. F. Fennell, and J. B. Blake (2020), Empirically estimated electron lifetimes in the earth's radiation belts: Comparison with theory, *Geophysical Research Letters*, *47*(3), e2019GL086,056, doi:https://doi.org/10.1029/2019GL086056, e2019GL086056 10.1029/2019GL086056.

Cunningham, G. S., V. Loridan, J.-F. Ripoll, and M. Schulz (2018), Neoclassical diffusion of radiation-belt electrons across very LowL-shells, *Journal of Geophysical Research: Space Physics*, *123*(4), 2884–2901, doi:10.1002/2017ja024931.

Davidson, G. T., P. C. Filbert, R. W. Nightingale, W. L. Imhof, J. B. Reagan, and E. C. Whipple (1988), Observations of intense trapped electron fluxes at synchronous altitudes, *Journal of Geophysical Research: Space Physics*, *93*(A1), 77–95, doi:https://doi.org/10.1029/JA093iA01p00077.

Dimitrakoudis, S., and I. R. Mann (2019), On the close correspondence between storm time ULF wave power and the POES VLF chorus wave amplitude proxy, *Geophysical Research Letters*, *46*(4), 1947–1955, doi:10.1029/2018gl081317.

Dungey, J. W. (1961), Interplanetary magnetic field and the auroral zones, *Physical Review Letters*, *6*(2), 47–48, doi:10.1103/physrevlett.6.47.

Elkington, S. R., and T. E. Sarris (2016), The role of Pc-5 ULF waves in the radiation belts: Current understanding and open questions, in *Waves, Particles, and Storms in Geospace*, edited by G. Balasis, I. A. Daglis, and I. R. Mann, chap. 4, pp. 80–101, Oxford University Press, Oxford, doi:10.1093/acprof:oso/9780198705246.001.0001.

Fox, N., and J. L. Burch (Eds.) (2014), *The Van Allen Probes Mission*, Springer US, doi:10.1007/978-1-4899-7433-4.

Fox, N. J., B. H. Mauk, and J. B. Blake (2006), Role of non-adiabatic processes in the creation of the outer radiation belts, *Geophysical Research Letters*, *33*(18), n/a–n/a, doi:10.1029/2006gl026598.

Friedel, R., G. Reeves, and T. Obara (2002), Relativistic electron dynamics in the inner magnetosphere – a review, *Journal of Atmospheric and Solar-Terrestrial Physics*, *64*(2), 265 – 282, doi:https://doi.org/10.1016/S1364-6826(01)00088-8, sTEP-Results, Applications and Modelling Phase (S-RAMP).

Garrett, H., and A. Whittlesey (2000), Spacecraft charging, an update, *IEEE Transactions on Plasma Science*, *28*(6), 2017–2028, doi:10.1109/27.902229.

Glatzmaier, G. A., and P. H. Roberts (1995), A three-dimensional convective dynamo solution with rotating and finitely conducting inner core and mantle, *Physics of the Earth and Planetary Interiors*, *91*(1-3), 63–75, doi:10.1016/0031-9201(95)03049-3.

Golub, L. (2010), *The solar corona*, Cambridge University Press, Cambridge, UK New York.

Gu, X., Y. Y. Shprits, and B. Ni (2012), Parameterized lifetime of radiation belt electrons interacting with lower-band and upper-band oblique chorus waves, *Geophysical Research Letters*, *39*(15), doi:10.1029/2012gl052519.

Henderson, M., S. Morley, J. Niehof, and B. Larsen (2017), drsteve/LANLGeoMag: LANLGeoMag v.1.5.15-alpha, doi:10.5281/zenodo.1133782.

Horne, R. B., R. M. Thorne, Y. Y. Shprits, N. P. Meredith, S. A. Glauert, A. J. Smith, S. G. Kanekal, D. N. Baker, M. J. Engebretson, J. L. Posch, M. Spasojevic, U. S. Inan, J. S. Pickett, and P. M. E. Decreau (2005), Wave acceleration of electrons in the Van Allen radiation belts, *Nature*, *437*(7056), 227–230, doi:10.1038/nature03939.

Horne, R. B., R. M. Thorne, S. A. Glauert, N. P. Meredith, D. Pokhotelov, and O. Santolík (2007), Electron acceleration in the Van Allen radiation belts by fast magnetosonic waves, *Geophysical Research Letters*, *34*(17), doi:10.1029/2007gl030267.

Horne, R. B., M. W. Phillips, S. A. Glauert, N. P. Meredith, A. D. P. Hands, K. A. Ryden, and W. Li (2018), Realistic worst case for a severe space weather event driven by a fast solar wind stream, *Space Weather*, *16*(9), 1202–1215, doi:10.1029/2018sw001948.

Hudson, M. K., D. N. Baker, J. Goldstein, B. T. Kress, J. Paral, F. R. Toffoletto, and M. Wiltberger (2014), Simulated magnetopause losses and Van Allen Probe flux dropouts, *Geophysical Research Letters*, *41*(4), 1113–1118, doi:10.1002/2014gl059222.

Hudson, M. K., J. Paral, B. T. Kress, M. Wiltberger, D. N. Baker, J. C. Foster, D. L. Turner, and J. R. Wygant (2015), Modeling CME-shock-driven storms in 2012-2013: MHD test particle simulations, *Journal of Geophysical Research: Space Physics*, *120*(2), 1168–1181, doi:10.1002/2014ja020833.

Hundhausen, A. J. (1995), The solar wind, in *Introduction to Space Physics*, edited by M. G. Kivelson and C. T. Russell, Cambridge atmospheric and space science series, chap. 4, pp. 91–128, Cambridge University Press, Cambridge.

Jaynes, A. N., D. N. Baker, H. J. Singer, J. V. Rodriguez, T. M. Loto'aniu, A. F. Ali, S. R. Elkington, X. Li, S. G. Kanekal, S. G. Claudepierre, J. F. Fennell, W. Li, R. M. Thorne, C. A. Kletzing, H. E. Spence, and G. D. Reeves (2015), Source and seed populations for relativistic electrons: Their roles in radiation belt changes, *Journal of Geophysical Research: Space Physics*, *120*(9), 7240–7254, doi:10.1002/2015ja021234.

Jaynes, A. N., A. F. Ali, S. R. Elkington, D. M. Malaspina, D. N. Baker, X. Li, S. G. Kanekal, M. G. Henderson, C. A. Kletzing, and J. R. Wygant (2018), Fast diffusion of ultrarelativistic electrons in the outer radiation belt: 17 march 2015 storm event, *Geophysical Research Letters*, *45*(20), doi:10.1029/2018gl079786.

Kasahara, Y., Y. Kasaba, H. Kojima, S. Yagitani, K. Ishisaka, A. Kumamoto, F. Tsuchiya, M. Ozaki, S. Matsuda, T. Imachi, Y. Miyoshi, M. Hikishima, Y. Katoh, M. Ota, M. Shoji, A. Matsuoka, and I. Shinohara (2018), The Plasma Wave Experiment (PWE) on board the Arase (ERG) satellite, *Earth, Planets and Space*, *70*(1), doi:10.1186/s40623-018-0842-4.

Kennel, C. F., and H. E. Petschek (1966), Limit on stably trapped particle fluxes, *Journal of Geophysical Research*, *71*(1), 1–28, doi:10.1029/jz071i001p00001.

Kilpua, E. K. J., A. Balogh, R. von Steiger, and Y. D. Liu (2017), Geoeffective properties of solar transients and stream interaction regions, *Space Science Reviews*, *212*(3-4), 1271–1314, doi:10.1007/s11214-017-0411-3.

Kivelson, M. G. (1995), Pulsations and magnetohydrodynamic waves, in *Introduction to Space Physics*, edited by M. G. Kivelson and C. T. Russell, Cambridge atmospheric and space science series, chap. 11, pp. 330–355, Cambridge University Press, Cambridge.

Kletzing, C. A., W. S. Kurth, M. Acuna, R. J. MacDowall, R. B. Torbert, T. Averkamp, D. Bodet, S. R. Bounds, M. Chutter, J. Connerney, D. Crawford, J. S. Dolan, R. Dvorsky, G. B. Hospodarsky, J. Howard, V. Jordanova, R. A. Johnson, D. L. Kirchner, B. Mokrzycki, G. Needell, J. Odom, D. Mark, R. Pfaff, J. R. Phillips, C. W. Piker, S. L. Remington, D. Rowland, O. Santolik, R. Schnurr, D. Sheppard, C. W. Smith, R. M. Thorne, and J. Tyler (2013), The Electric and Magnetic Field Instrument Suite and Integrated Science (EMFISIS) on RBSP, *Space Science Reviews*, *179*(1-4), 127–181, doi:10.1007/s11214-013-9993-6.

Knipp, D. J., B. J. Fraser, M. A. Shea, and D. F. Smart (2018), On the little-known consequences of the 4 august 1972 ultra-fast coronal mass ejecta: Facts, commentary, and call to action, *Space Weather*, *16*(11), 1635–1643, doi:https://doi.org/10.1029/2018SW002024.

Koskinen, H. E. J., and E. K. J. Kilpua (2022), *Physics of Earth's Radiation Belts*, Springer International Publishing, doi:10.1007/978-3-030-82167-8.

Lai, S. (2003), A critical overview on spacecraft charging mitigation methods, *IEEE Transactions on Plasma Science*, *31*(6), 1118–1124, doi:10.1109/tps.2003.820969.

Lai, S. T. (2012), *Fundamentals of Spacecraft Charging*, Princeton University Press, doi:10.1515/9781400839094.

Landau, L., and E. Lifshitz (1976), The canonical equations, in *Mechanics*, pp. 131–167, Elsevier, doi:10.1016/b978-0-08-050347-9.50012-5.

Lee, J., K. Min, and K. Kim (2013), Characteristic dimension of electromagnetic ion cyclotron wave activity in the magnetosphere, *Journal of Geophysical Research: Space Physics*, *118*(4), 1651–1658, doi:10.1002/jgra.50242.

Lejosne, S. (2020), Electromagnetic radial diffusion in the Earth's radiation belts as determined by the solar wind immediate time history and a toy model for the electromagnetic fields, *Journal of Geophysical Research: Space Physics*, *125*(6), e2020JA027,893, doi:https://doi.org/10.1029/2020JA027893, e2020JA027893 2020JA027893.

Li, W., and M. Hudson (2019), Earth's Van Allen radiation belts: From discovery to the Van Allen Probes era, *Journal of Geophysical Research: Space Physics*, *124*(11), 8319–8351, doi:https://doi.org/10.1029/2018JA025940.

Li, W., R. M. Thorne, J. Bortnik, D. N. Baker, G. D. Reeves, S. G. Kanekal, H. E. Spence, and J. C. Green (2015), Solar wind conditions leading to efficient radiation belt electron acceleration: A superposed epoch analysis, *Geophysical Research Letters*, *42*(17), 6906–6915, doi:10.1002/2015gl065342.

Li, W., Q. Ma, J. Bortnik, and R. M. Thorne (2020), *Recent Advances in Understanding Radiation Belt Electron Dynamics Due to Wave–Particle Interactions*, chap. 12, pp. 207–229, American Geophysical Union (AGU), doi:10.1002/9781119509592.ch12.

Li, Z., M. Hudson, J. Paral, M. Wiltberger, and D. Turner (2016), Global ULF wave analysis of radial diffusion coefficients using a global MHD model for the 17 March 2015 storm, *Journal of Geophysical Research: Space Physics*, *121*(7), 6196–6206, doi:10.1002/2016ja022508.

Li, Z., M. Hudson, M. Patel, M. Wiltberger, A. Boyd, and D. Turner (2017a), ULF wave analysis and radial diffusion calculation using a global MHD model for the 17 March 2013 and 2015 storms, *Journal of Geophysical Research: Space Physics*, *122*(7), 7353–7363, doi:10.1002/2016ja023846.

Li, Z., M. Hudson, M. Patel, M. Wiltberger, A. Boyd, and D. Turner (2017b), Ulf wave analysis and radial diffusion calculation using a global MHD model for the 17 March 2013 and 2015 storms, *Journal of Geophysical Research: Space Physics*, *122*(7), 7353–7363, doi:https://doi.org/10.1002/2016JA023846.

Loewe, C. A., and G. W. Prölss (1997), Classification and mean behavior of magnetic storms, *Journal of Geophysical Research: Space Physics*, *102*(A7), 14,209–14,213, doi:10.1029/96ja04020.

Mann, I., L. Ozeke, S. Morley, K. Murphy, S. Claudepierre, D. Turner, D. Baker, I. Rae, A. Kale, D. Milling, A. Boyd, H. Spence, H. Singer, S. Dimitrakoudis, I. Daglis, and F. Honary (2018), Reply to 'The dynamics of Van Allen belts revisited', *Nature Physics*, *14*(2), 103–104, doi:10.1038/nphys4351.

Mann, I. R., and L. G. Ozeke (2016), How quickly, how deeply, and how strongly can dynamical outer boundary conditions impact Van Allen radiation belt morphology?, *Journal of Geophysical Research: Space Physics*, *121*(6), 5553–5558, doi:10.1002/2016ja022647.

Mann, I. R., E. A. Lee, S. G. Claudepierre, J. F. Fennell, A. Degeling, I. J. Rae, D. N. Baker, G. D. Reeves, H. E. Spence, L. G. Ozeke, R. Rankin, D. K. Milling, A. Kale, R. H. W. Friedel, and F. Honary (2013), Discovery of the action of a geophysical synchrotron in the Earth's Van Allen radiation belts, *Nature Communications*, *4*(1), doi:10.1038/ncomms3795.

Mann, I. R., L. G. Ozeke, K. R. Murphy, S. G. Claudepierre, D. L. Turner, D. N. Baker, I. J. Rae, A. Kale, D. K. Milling, A. J. Boyd, H. E. Spence, G. D. Reeves, H. J. Singer, S. Dimitrakoudis, I. A. Daglis, and F. Honary (2016), Explaining the dynamics of the ultra-relativistic third Van Allen radiation belt, *Nature Physics*, *12*(10), 978–983, doi:10.1038/nphys3799.

Matsuoka, A., M. Teramoto, R. Nomura, M. Nosé, A. Fujimoto, Y. Tanaka, M. Shinohara, T. Nagatsuma, K. Shiokawa, Y. Obana, Y. Miyoshi, M. Mita, T. Takashima, and I. Shinohara (2018), The ARASE (ERG) magnetic field investigation, *Earth, Planets and Space*, *70*(1), doi:10.1186/s40623-018-0800-1.

Mauk, B. H. (2021), Software for "Radiation Belts of the Solar System", doi:10.5281/zenodo.4782323.

Mauk, B. H., and N. J. Fox (2010), Electron radiation belts of the solar system, *Journal of Geophysical Research: Space Physics*, *115*(A12), n/a–n/a, doi:10.1029/2010ja015660.

Mauk, B. H., N. J. Fox, S. G. Kanekal, R. L. Kessel, D. G. Sibeck, and A. Ukhorskiy (2012), Science Objectives and Rationale for the Radiation Belt Storm Probes Mission, *Space Science Reviews*, *179*(1-4), 3–27, doi:10.1007/s11214-012-9908-y.

McComas, D. J., H. A. Elliott, N. A. Schwadron, J. T. Gosling, R. M. Skoug, and B. E. Goldstein (2003), The three-dimensional solar wind around solar maximum, *Geophysical Research Letters*, *30*(10), n/a–n/a, doi:10.1029/2003gl017136.

McIlwain, C. E. (1966), Magnetic coordinates, *Space Science Reviews*, *5*(5), 585–598.

Meredith, N. P. (2003), Statistical analysis of relativistic electron energies for cyclotron resonance with EMIC waves observed on CRRES, *Journal of Geophysical Research*, *108*(A6), doi:10.1029/2002ja009700.

Meredith, N. P., R. B. Horne, I. Sandberg, C. Papadimitriou, and H. D. R. Evans (2017), Extreme relativistic electron fluxes in the earth's outer radiation belt: Analysis of integral irem data, *Space Weather*, *15*(7), 917–933, doi:10.1002/2017SW001651.

Millan, R., and R. Thorne (2007), Review of radiation belt relativistic electron losses, *Journal of Atmospheric and Solar-Terrestrial Physics*, *69*(3), 362–377, doi:https://doi.org/10.1016/j.jastp.2006.06.019, global Aspects of Magnetosphere-Ionosphere Coupling.

Miyoshi, Y., I. Shinohara, T. Takashima, K. Asamura, N. Higashio, T. Mitani, S. Kasahara, S. Yokota, Y. Kazama, S.-Y. Wang, S. W. Y. Tam, P. T. P. Ho, Y. Kasahara, Y. Kasaba, S. Yagitani, A. Matsuoka, H. Kojima, Y. Katoh, K. Shiokawa, and K. Seki (2018), Geospace exploration project ERG, *Earth, Planets and Space*, *70*(1), doi:10.1186/s40623-018-0862-0.

Morley, S. K., R. H. W. Friedel, E. L. Spanswick, G. D. Reeves, J. T. Steinberg, J. Koller, T. Cayton, and E. Noveroske (2010), Dropouts of the outer electron radiation belt in response to solar wind stream interfaces: global positioning system observations, *Proceedings of the Royal Society of London A: Mathematical, Physical and Engineering Sciences*, *466*(2123), 3329–3350, doi:10.1098/rspa.2010.0078.

Morley, S. K., M. G. Henderson, G. D. Reeves, R. H. W. Friedel, and D. N. Baker (2013), Phase Space Density matching of relativistic electrons using the Van Allen Probes: REPT results, *Geophysical Research Letters*, *40*(18), 4798–4802, doi:10.1002/grl.50909.

Morley, S. K., J. P. Sullivan, M. G. Henderson, J. B. Blake, and D. N. Baker (2016), The Global Positioning System constellation as a space weather monitor: Comparison of electron measurements with Van Allen Probes data, *Space Weather*, *14*(2), 76–92, doi:10.1002/2015sw001339.

Morley, S. K., J. P. Sullivan, M. R. Carver, R. M. Kippen, R. H. W. Friedel, G. D. Reeves, and M. G. Henderson (2017), Energetic particle data from the Global Positioning System constellation, *Space Weather*, *15*(2), 283–289, doi:10.1002/2017sw001604.

Morley, S. K., T. V. Brito, and D. T. Welling (2018), Measures of model performance based on the log accuracy ratio, *Space Weather*, *16*(1), 69–88, doi:https://doi.org/10.1002/2017SW001669.

Murphy, K. R., C. E. J. Watt, I. R. Mann, I. J. Rae, D. G. Sibeck, A. J. Boyd, C. F. Forsyth, D. L. Turner, S. G. Claudepierre, D. N. Baker, H. E. Spence, G. D. Reeves, J. B. Blake, and J. Fennell (2018), The global statistical response of the outer radiation belt during geomagnetic storms, *Geophysical Research Letters*, *45*(9), 3783–3792, doi:10.1002/2017gl076674.

Murphy, K. R., I. R. Mann, D. G. Sibeck, I. J. Rae, C. Watt, L. G. Ozeke, S. G. Kanekal, and D. N. Baker (2020), A framework for understanding and quantifying the loss and acceleration of relativistic electrons in the outer radiation belt during geomagnetic storms, *Space Weather*, *18*(5), e2020SW002,477, doi:10.1029/2020SW002477.

O'Brien, T. P., J. F. Fennell, J. L. Roeder, and G. D. Reeves (2007), Extreme electron fluxes in the outer zone, *Space Weather*, *5*(1), n/a–n/a, doi:10.1029/2006sw000240.

Olifer, L. (2019), On the signatures of magnetopause shadowing losses in the Van Allen radiation belts of the earth, Master's thesis, University of Alberta.

Olifer, L., I. R. Mann, S. K. Morley, L. G. Ozeke, and D. Choi (2018), On the role of last closed drift shell dynamics in driving fast losses and Van Allen radiation belt extinction, *Journal of Geophysical Research: Space Physics*, doi:10.1029/2018JA025190.

Olifer, L., I. R. Mann, L. G. Ozeke, I. J. Rae, and S. K. Morley (2019), On the relative strength of electric and magnetic ULF wave radial diffusion during the march 2015 geomagnetic storm, *Journal of Geophysical Research: Space Physics*, *124*(4), 2569–2587, doi:10.1029/2018ja026348.

Olifer, L., I. R. Mann, L. G. Ozeke, S. G. Claudepierre, D. N. Baker, and H. E. Spence (2021a), On the similarity and repeatability of fast radiation belt loss: Role of the last closed drift shell, *Journal of Geophysical Research: Space Physics*, *126*(11), doi:10.1029/2021ja029957.

Olifer, L., I. R. Mann, A. Kale, B. H. Mauk, S. G. Claudepierre, D. N. Baker, H. E. Spence, and L. G. Ozeke (2021b), A tale of two radiation belts: The energy-dependence of self-limiting electron space radiation, *Geophysical Research Letters*, *48*(20), doi:10.1029/2021gl095779.

Olifer, L., I. R. Mann, L. G. Ozeke, S. K. Morley, and H. L. Louis (2021c), On the formation of phantom electron phase space density peaks in single spacecraft radiation belt data, *Geophysical Research Letters*, *48*(11), doi:10.1029/2020gl092351.

Olifer, L., I. R. Mann, S. G. Claudepierre, D. N. Baker, H. E. Spence, and L. G. Ozeke (2022a), A natural limit to the spectral hardness of worst-case electron radiation in the terrestrial Van Allen belt, *Journal of Geophysical Research: Space Physics*, doi:10.1029/2022JA030506.

Olifer, L., S. K. Morley, L. G. Ozeke, I. R. Mann, M. Kalliokoski, M. Henderson, R. Niyazov, and A. Hoover (2022b), Rapid acceleration bursts in the Van Allen radiation belt, *Prepared for publication*.

Ozeke, L., I. Mann, S. Dufresne, L. Olifer, S. Morley, S. Claudepierre, K. Murphy, H. Spence, D. Baker, and A. Degeling (2020), Rapid outer radiation belt flux dropouts and fast acceleration during the March 2015 and 2013 storms: The role of ULF wave transport from a dynamic outer boundary, *Journal of Geophysical Research: Space Physics*, doi:10.1029/2019ja027179.

Ozeke, L. G., I. R. Mann, and I. J. Rae (2009), Mapping guided Alfvén wave magnetic field amplitudes observed on the ground to equatorial electric field amplitudes in space, *Journal of Geophysical Research: Space Physics*, *114*(A1), n/a–n/a, doi:10.1029/2008ja013041.

Ozeke, L. G., I. R. Mann, K. R. Murphy, J. I. Rae, and D. K. Milling (2014), Analytic expressions for ULF wave radiation belt radial diffusion coefficients, *Journal of Geophysical Research: Space Physics*, *119*(3), 1587–1605, doi:10.1002/2013JA019204, 2013JA019204.

Ozeke, L. G., I. R. Mann, K. R. Murphy, A. W. Degeling, S. G. Claudepierre, and H. E. Spence (2018), Explaining the apparent impenetrable barrier to ultra-relativistic electrons in the outer Van Allen belt, *Nature Communications*, *9*(1), doi:10.1038/s41467-018-04162-3.

Ozeke, L. G., I. R. Mann, S. G. Claudepierre, M. Henderson, S. K. Morley, K. R. Murphy, L. Olifer, H. E. Spence, and D. N. Baker (2019), The March 2015 superstorm revisited: Phase space density profiles and fast ULF wave diffusive transport, *Journal of Geophysical Research: Space Physics*, *124*(2), 1143–1156, doi:10.1029/2018ja026326.

Parker, E. N. (1958), Dynamics of the interplanetary gas and magnetic fields., *The Astrophysical Journal*, *128*, 664, doi:10.1086/146579.

Priest, E. R. (1982), *Solar Magnetohydrodynamics*, Springer Netherlands, doi:10.1007/978-94-009-7958-1.

Priest, E. R. (1995), The Sun and its magnetohydrodynamics, in *Introduction to Space Physics*, edited by M. G. Kivelson and C. T. Russell, Cambridge atmospheric and space science series, chap. 3, pp. 58–89, Cambridge University Press, Cambridge.

Reeves, G. D. (2007), Radiation belt storm probes: A new mission for space weather forecasting, *Space Weather*, *5*(11), n/a–n/a, doi:10.1029/2007sw000341.

Reeves, G. D., K. L. McAdams, R. H. W. Friedel, and T. P. O'Brien (2003), Acceleration and loss of relativistic electrons during geomagnetic storms, *Geophysical Research Letters*, *30*(10), doi:10.1029/2002gl016513.

Reeves, G. D., H. E. Spence, M. G. Henderson, S. K. Morley, R. H. W. Friedel, H. O. Funsten, D. N. Baker, S. G. Kanekal, J. B. Blake, J. F. Fennell, S. G. Claudepierre, R. M. Thorne, D. L. Turner, C. A. Kletzing, W. S. Kurth, B. A. Larsen, and J. T. Niehof (2013), Electron acceleration in the heart of the Van Allen radiation belts, *Science*, *341*(6149), 991–994, doi:10.1126/science.1237743.

Reeves, G. D., R. H. W. Friedel, B. A. Larsen, R. M. Skoug, H. O. Funsten, S. G. Claudepierre, J. F. Fennell, D. L. Turner, M. H. Denton, H. E. Spence, J. B. Blake, and D. N. Baker (2016), Energy-dependent dynamics of keV to MeV electrons in the inner zone, outer zone, and slot regions, *Journal of Geophysical Research: Space Physics*, *121*(1), 397–412, doi:10.1002/2015ja021569.

Rodger, C. J., M. A. Clilverd, J. C. Green, and M. M. Lam (2010), Use of POES SEM-2 observations to examine radiation belt dynamics and energetic electron precipitation into the atmosphere, *Journal of Geophysical Research: Space Physics*, *115*(A4), n/a–n/a, doi:10.1029/2008ja014023.

Roederer, J. G. (1970), *Dynamics of Geomagnetically Trapped Radiation*, Springer Berlin Heidelberg, doi:10.1007/978-3-642-49300-3.

Russell, C. (1995), Brief history of solar terrestrial physics, in *Introduction to Space Physics*, edited by M. Kivelson and C. Russell, Cambridge atmospheric and space science series, chap. 1, pp. 1–26, Cambridge University Press, Cambridge.

Sandhu, J. K., I. J. Rae, J. R. Wygant, A. W. Breneman, S. Tian, C. E. J. Watt, R. B. Horne, L. G. Ozeke, M. Georgiou, and M.-T. Walach (2021), ULF wave driven radial diffusion during geomagnetic storms: A statistical analysis of Van Allen Probes observations, *Journal of Geophysical Research: Space Physics*, *126*(4), doi:10.1029/2020ja029024.

Sawyer, D. M., and J. I. Vette (1976), AP-8 trapped proton environment for solar maximum and solar minimum, *NASA STI/Recon Technical Report N*, *77*.

Schulz, M., and G. T. Davidson (1988), Limiting energy spectrum of a saturated radiation belt, *Journal of Geophysical Research*, *93*(A1), 59, doi:10.1029/ja093ia01p00059.

Schulz, M., and L. J. Lanzerotti (1974), *Particle Diffusion in the Radiation Belts*, Springer Berlin Heidelberg, doi:10.1007/978-3-642-65675-0.

Schwenn, R. (2006), Space weather: The solar perspective, *Living Reviews in Solar Physics*, *3*, doi:10.12942/lrsp-2006-2.

Sheeley, B. W., M. B. Moldwin, H. K. Rassoul, and R. R. Anderson (2001), An empirical plasmasphere and trough density model: CRRES observations, *Journal of Geophysical Research: Space Physics*, *106*(A11), 25,631–25,641, doi:10.1029/2000ja000286.

Shprits, Y. Y., R. M. Thorne, R. Friedel, G. D. Reeves, J. Fennell, D. N. Baker, and S. G. Kanekal (2006), Outward radial diffusion driven by losses at magnetopause, *Journal of Geophysical Research*, *111*(A11), doi:10.1029/2006ja011657.

Shprits, Y. Y., N. P. Meredith, and R. M. Thorne (2007), Parameterization of radiation belt electron loss timescales due to interactions with chorus waves, *Geophysical Research Letters*, *34*(11), doi:10.1029/2006GL029050, l11110.

Shprits, Y. Y., D. A. Subbotin, N. P. Meredith, and S. R. Elkington (2008a), Review of modeling of losses and sources of relativistic electrons in the outer radiation belt II: Local acceleration and loss, *Journal of Atmospheric and Solar-Terrestrial Physics*, *70*(14), 1694–1713, doi:10.1016/j.jastp.2008.06.014.

Shprits, Y. Y., S. R. Elkington, N. P. Meredith, and D. A. Subbotin (2008b), Review of modeling of losses and sources of relativistic electrons in the outer radiation belt I: Radial transport, *Journal of Atmospheric and Solar-Terrestrial Physics*, *70*(14), 1679–1693, doi:10.1016/j.jastp.2008.06.008.

Shprits, Y. Y., A. Y. Drozdov, M. Spasojevic, A. C. Kellerman, M. E. Usanova, M. J. Engebretson, O. V. Agapitov, I. S. Zhelavskaya, T. J. Raita, H. E. Spence, D. N. Baker, H. Zhu, and N. A. Aseev (2016), Wave-induced loss of ultra-relativistic electrons in the Van Allen radiation belts, *Nature Communications*, *7*, 12,883, doi:10.1038/ncomms12883.

Shprits, Y. Y., R. B. Horne, A. C. Kellerman, and A. Y. Drozdov (2018), The dynamics of Van Allen belts revisited, *Nature Physics*, *14*(2), 102–103, doi:10.1038/nphys4350.

Smirnov, A. G., M. Berrendorf, Y. Y. Shprits, E. A. Kronberg, H. J. Allison, N. A. Aseev, I. S. Zhelavskaya, S. K. Morley, G. D. Reeves, M. R. Carver, and F. Effenberger (2020), Medium energy electron flux in earth's outer radiation belt (merlin): A machine learning model, *Space Weather*, *18*(11), e2020SW002,532, doi:https://doi.org/10.1029/2020SW002532, e2020SW002532 10.1029/2020SW002532.

Spasojevic, M., Y. Y. Shprits, and K. Orlova (2015), Global empirical models of plasmaspheric hiss using Van Allen probes, *Journal of Geophysical Research: Space Physics*, *120*(12), 10,370–10,383, doi:10.1002/2015ja021803.

Spence, H. E., G. D. Reeves, D. N. Baker, J. B. Blake, M. Bolton, S. Bourdarie, A. A. Chan, S. G. Claudepierre, J. H. Clemmons, J. P. Cravens, S. R. Elkington, J. F. Fennell, R. H. W. Friedel, H. O. Funsten, J. Goldstein, J. C. Green, A. Guthrie, M. G. Henderson, R. B. Horne, M. K. Hudson, J.-M. Jahn, V. K. Jordanova, S. G. Kanekal, B. W. Klatt, B. A. Larsen, X. Li, E. A. MacDonald, I. R. Mann, J. Niehof, T. P. O'Brien, T. G. Onsager, D. Salvaggio, R. M. Skoug, S. S. Smith, L. L. Suther, M. F. Thomsen, and R. M. Thorne (2013), Science goals and overview of the radiation belt storm probes (RBSP) energetic particle, composition, and thermal plasma (ECT) suite on NASA's Van Allen probes mission, *Space Science Reviews*, *179*(1-4), 311–336, doi:10.1007/s11214-013-0007-5.

Summers, D., and R. Shi (2014), Limiting energy spectrum of an electron radiation belt, *Journal of Geophysical Research: Space Physics*, *119*(8), 6313–6326, doi:https://doi.org/10.1002/2014JA020250.

Summers, D., C. Ma, N. P. Meredith, R. B. Horne, R. M. Thorne, D. Heynderickx, and R. R. Anderson (2002), Model of the energization of outer-zone electrons by whistler-mode chorus during the October 9, 1990 geomagnetic storm, *Geophysical Research Letters*, *29*(24), 27–1–27–4, doi:10.1029/2002gl016039.

Summers, D., R. Tang, and R. M. Thorne (2009), Limit on stably trapped particle fluxes in planetary magnetospheres, *Journal of Geophysical Research: Space Physics*, *114*(A10), n/a–n/a, doi:10.1029/2009ja014428.

Thorne, R. M., E. J. Smith, R. K. Burton, and R. E. Holzer (1973), Plasmaspheric hiss, *Journal of Geophysical Research*, *78*(10), 1581–1596, doi:10.1029/JA078i010p01581.

Thorne, R. M., B. Ni, X. Tao, R. B. Horne, and N. P. Meredith (2010), Scattering by chorus waves as the dominant cause of diffuse auroral precipitation, *Nature*, *467*(7318), 943–946, doi:10.1038/nature09467.

Tsurutani, B. T. (2003), The extreme magnetic storm of 1–2 september 1859, *Journal of Geophysical Research*, *108*(A7), doi:10.1029/2002ja009504.

Tsyganenko, N. A., and M. I. Sitnov (2005), Modeling the dynamics of the inner magnetosphere during strong geomagnetic storms, *Journal of Geophysical Research: Space Physics*, *110*(A3), doi:10.1029/2004JA010798, a03208.

Tu, W., Z. Xiang, and S. K. Morley (2019), Modeling the magnetopause shadowing loss during the June 2015 dropout event, *Geophysical Research Letters*, *46*(16), 9388–9396, doi:10.1029/2019gl084419.

Turner, D. L., and A. Y. Ukhorskiy (2020), Outer radiation belt losses by magnetopause incursions and outward radial transport: new insight and outstanding questions from the Van Allen probes era, in *The Dynamic Loss of Earth's Radiation Belts*, pp. 1–28, Elsevier, doi:10.1016/b978-0-12-813371-2.00001-9.

Turner, D. L., Y. Shprits, M. Hartinger, and V. Angelopoulos (2012), Explaining sudden losses of outer radiation belt electrons during geomagnetic storms, *Nature Physics*, *8*(3), 208–212, doi:10.1038/nphys2185.

Turner, D. L., V. Angelopoulos, S. K. Morley, M. G. Henderson, G. D. Reeves, W. Li, D. N. Baker, C.-L. Huang, A. Boyd, H. E. Spence, S. G. Claudepierre, J. B. Blake, and J. V. Rodriguez (2014), On the cause and extent of outer radiation belt losses during the 30 september 2012 dropout event, *Journal of Geophysical Research: Space Physics*, *119*(3), 1530–1540, doi:10.1002/2013ja019446.

Turner, D. L., T. P. O'Brien, J. F. Fennell, S. G. Claudepierre, J. B. Blake, E. K. J. Kilpua, and H. Hietala (2015), The effects of geomagnetic storms on electrons in Earth's radiation belts, *Geophysical Research Letters*, *42*(21), 9176–9184, doi:https://doi.org/10.1002/2015GL064747.

Turner, D. L., E. K. J. Kilpua, H. Hietala, S. G. Claudepierre, T. P. O'Brien, J. F. Fennell, J. B. Blake, A. N. Jaynes, S. Kanekal, D. N. Baker, H. E. Spence, J.-F. Ripoll, and G. D. Reeves (2019), The response of Earth's electron radiation belts to geomagnetic storms: Statistics from the Van Allen Probes era including effects from different storm drivers, *Journal of Geophysical Research: Space Physics*, *124*(2), 1013–1034, doi:10.1029/2018JA026066.

Ukhorskiy, A. Y., Y. Y. Shprits, B. J. Anderson, K. Takahashi, and R. M. Thorne (2010), Rapid scattering of radiation belt electrons by storm-time EMIC waves, *Geophysical Research Letters*, *37*(9), n/a–n/a, doi:10.1029/2010gl042906.

Usanova, M. E., and I. R. Mann (2016), Understanding the role of emic waves in radiation belt and ring current dynamics: Recent advances, *Waves, particles, and storms in geospace: A complex interplay*, pp. 244–276.

Usanova, M. E., A. Drozdov, K. Orlova, I. R. Mann, Y. Shprits, M. T. Robertson, D. L. Turner, D. K. Milling, A. Kale, D. N. Baker, S. A. Thaller, G. D. Reeves, H. E. Spence, C. Kletzing, and J. Wygant (2014), Effect of EMIC waves on relativistic and ultrarelativistic electron populations: Ground-based and Van Allen probes observations, *Geophysical Research Letters*, *41*(5), 1375–1381, doi:10.1002/2013gl059024.

Van Allen, J. A., and L. A. Frank (1959), Radiation around the earth to a radial distance of 107400 km., *Nature*, *183*(430), doi:10.1038/183430a0.

Vette, J. I. (1991), The AE-8 trapped electron model environment, *NASA STI/Recon Technical Report N*, *92*.

Walsh, B. M., D. G. Sibeck, Y. Nishimura, and V. Angelopoulos (2013), Statistical analysis of the plasmaspheric plume at the magnetopause, *Journal of Geophysical Research: Space Physics*, *118*(8), 4844–4851, doi:10.1002/jgra.50458.

Walt, M. (1994), *Introduction to Geomagnetically Trapped Radiation*, Cambridge University Press, doi:10.1017/cbo9780511524981.

Wang, D., Y. Y. Shprits, I. S. Zhelavskaya, F. Effenberger, A. M. Castillo, A. Y. Drozdov, N. A. Aseev, and S. Cervantes (2020), The effect of plasma boundaries on the dynamic evolution of relativistic radiation belt electrons, *Journal of Geophysical Research: Space Physics*, *125*(5), doi:10.1029/2019ja027422.

Webb, D. F., and T. A. Howard (2012), Coronal mass ejections: Observations, *Living Reviews in Solar Physics*, *9*, doi:10.12942/lrsp-2012-3.

Xiang, Z., W. Tu, X. Li, B. Ni, S. K. Morley, and D. N. Baker (2017), Understanding the mechanisms of radiation belt dropouts observed by Van Allen probes, *Journal of Geophysical Research: Space Physics*, *122*(10), 9858–9879, doi:10.1002/2017ja024487.

Xiang, Z., W. Tu, B. Ni, M. G. Henderson, and X. Cao (2018), A statistical survey of radiation belt dropouts observed by Van Allen probes, *Geophysical Research Letters*, doi:10.1029/2018gl078907.

Xiao, F., R. M. Thorne, and D. Summers (1998), Instability of electromagnetic R-mode waves in a relativistic plasma, *Physics of Plasmas*, *5*(7), 2489–2497, doi:10.1063/1.872932.

Yu, Y., J. Koller, S. Zaharia, and V. Jordanova (2012), L* neural networks from different magnetic field models and their applicability, *Space Weather*, *10*(2), doi:10.1029/2011sw000743.

Zhang, K., X. Li, H. Zhao, Z. Xiang, L. Y. Khoo, W. Zhang, B. Hogan, and M. A. Temerin (2021), Upper limit of electron fluxes observed in the radiation belts, *Journal of Geophysical Research: Space Physics*, *126*(1), doi:10.1029/2020ja028511.

Zhao, H., R. H. W. Friedel, Y. Chen, G. D. Reeves, D. N. Baker, X. Li, A. N. Jaynes, S. G. Kanekal, S. G. Claudepierre, J. F. Fennell, J. B. Blake, and H. E. Spence (2018), An empirical model of radiation belt electron pitch angle distributions based on Van Allen probes measurements, *Journal of Geophysical Research: Space Physics*, *123*(5), 3493–3511, doi:10.1029/2018ja025277.

Zhao, H., D. Baker, X. Li, D. Malaspina, A. Jaynes, and S. Kanekal (2019), On the acceleration mechanism of ultrarelativistic electrons in the center of the outer radiation belt: A statistical study, *Journal of Geophysical Research: Space Physics*, *124*(11), 8590–8599, doi:https://doi.org/10.1029/2019JA027111.

Appendix A

Lists of Events Selected for the Superposed Epoch Analysis

Table A.1: List of zero epochs, used in the statistical superposed epoch study, with the respective minimal last closed drift shell (LCDS) location in each storm over the course of six days.

Date	**UTC**	**Minimal LCDS**
2012-10-01	2:25:00	5.023
2012-10-13	9:00:00	5.309
2012-11-01	11:55:00	5.309
2013-01-17	18:20:00	5.319
2013-03-01	10:05:00	5.430
2013-03-17	10:00:00	4.906
2013-05-01	7:15:00	5.797
2013-05-18	2:45:00	5.775
2013-06-01	6:30:00	5.002
2013-06-07	2:40:00	5.639
2013-06-29	11:25:00	5.285
2013-07-06	6:30:00	5.544
2013-07-10	11:55:00	5.578
2013-07-14	15:10:00	5.561
2013-08-04	21:35:00	5.637
2013-10-02	5:00:00	4.696
2013-10-08	22:40:00	5.385
2013-12-08	3:30:00	5.106
2013-12-25	13:35:00	5.685
2014-02-27	21:25:00	5.109
2014-04-12	6:00:00	5.697
2014-04-30	12:15:00	5.661
2014-05-08	8:35:00	5.604
2014-06-08	5:50:00	5.205
2014-09-12	22:20:00	5.316
2014-12-22	4:30:00	5.348
2015-01-26	10:00:00	5.564
2015-02-02	2:30:00	5.391
2015-02-17	22:05:00	5.566
2015-03-17	15:05:00	4.320
2015-05-06	16:10:00	5.505
2015-06-08	6:55:00	5.211
2015-07-04	21:20:00	5.348
2015-07-11	4:05:00	5.502
2015-07-23	7:40:00	5.759

Date	**UTC**	**Minimal LCDS**
2015-10-07	16:10:00	5.171
2015-10-18	9:15:00	5.764
2015-11-03	8:50:00	5.603
2015-11-07	7:20:00	5.367
2015-12-14	18:00:00	5.213
2015-12-20	8:10:00	4.715
2016-02-16	17:05:00	5.703
2016-03-06	19:20:00	5.022
2016-04-07	21:15:00	5.673
2016-04-13	0:35:00	5.619
2016-06-05	14:20:00	5.557
2016-07-20	4:45:00	5.301
2016-08-03	10:35:00	5.490
2016-08-23	20:30:00	5.652
2016-10-13	12:15:00	4.858
2016-10-25	12:50:00	5.695
2016-11-10	17:00:00	5.784
2017-03-01	12:20:00	5.748
2017-03-27	10:00:00	5.577
2017-04-04	7:10:00	5.733
2017-04-20	4:15:00	5.775
2017-05-20	9:20:00	5.707
2017-07-16	11:25:00	5.254
2017-08-04	10:30:00	5.756
2017-08-31	11:55:00	5.575
2017-09-28	7:45:00	5.729
2017-12-04	18:45:00	5.668
2018-03-10	4:20:00	5.763
2018-04-20	9:10:00	4.923
2018-05-05	16:55:00	5.762
2018-08-26	8:25:00	4.767
2018-09-10	22:15:00	5.757
2019-01-31	21:05:00	5.450
2019-06-08	17:40:00	5.484

Table A.2: List of zero epochs, used in the statistical superposed epoch study, with the respective minimal Dst index in each storm over the course of six days.

Date	**UTC**	**Minimal Dst, nT**
2012-10-01	4:25:00	-122
2012-11-01	20:25:00	-65
2012-11-14	7:25:00	-108
2013-01-17	22:00:00	-53
2013-01-26	22:30:00	-51
2013-03-01	10:30:00	-55
2013-03-17	20:30:00	-132
2013-03-29	17:00:00	-61
2013-04-24	18:25:00	-50
2013-05-01	18:25:00	-67
2013-05-18	4:30:00	-57
2013-05-25	6:00:00	-54
2013-06-01	8:20:00	-119
2013-06-07	5:20:00	-73
2013-06-29	1:25:00	-98
2013-07-06	18:25:00	-79
2013-07-14	23:00:00	-73
2013-08-27	21:20:00	-54
2013-10-02	7:20:00	-67
2013-10-09	1:00:00	-62
2013-12-08	8:30:00	-66
2014-04-12	9:00:00	-81
2014-04-30	9:25:00	-64
2014-08-27	18:25:00	-80
2014-09-12	23:30:00	-75
2014-11-10	17:30:00	-57
2014-11-16	7:00:00	-50
2014-12-22	5:30:00	-51
2015-02-18	0:15:00	-64
2015-02-24	7:15:00	-56
2015-03-02	8:30:00	-54
2015-03-17	22:30:00	-223
2015-04-16	23:25:00	-79
2015-06-08	8:30:00	-73
2015-06-23	4:30:00	-204

Date	**UTC**	**Minimal Dst, nT**
2015-07-05	5:00:00	-67
2015-07-13	15:25:00	-61
2015-07-23	7:30:00	-63
2015-08-27	20:20:00	-92
2015-09-20	15:25:00	-75
2015-10-07	22:25:00	-124
2015-12-20	22:30:00	-155
2016-01-01	0:00:00	-110
2016-01-20	16:25:00	-93
2016-03-06	21:30:00	-98
2016-04-02	23:00:00	-56
2016-04-07	21:30:00	-60
2016-05-08	8:00:00	-83
2016-08-03	10:30:00	-51
2016-08-23	21:30:00	-74
2016-09-29	9:30:00	-66
2016-10-13	17:25:00	-104
2016-11-10	17:20:00	-57
2017-03-01	21:30:00	-61
2017-03-27	14:30:00	-74
2017-04-22	16:00:00	-50
2017-05-28	7:30:00	-125
2017-07-16	15:30:00	-72
2017-08-31	11:30:00	-50
2017-09-08	1:30:00	-142
2017-09-28	6:30:00	-76
2017-10-14	5:30:00	-57
2018-03-18	21:25:00	-50
2018-04-20	9:30:00	-66
2018-05-06	1:25:00	-56
2018-08-26	6:30:00	-174
2018-09-11	10:20:00	-60
2018-10-07	21:00:00	-53
2018-11-05	5:30:00	-53
2019-08-05	20:00:00	-53

Appendix B

Two-Dimensional Superposed Epoch Analysis: Approaches and Methodology

B.1 Superposed Epoch Analysis of the Van Allen Probe Data

Performing a superposed epoch analysis of the flux data from the Van Allen Probes is more complicated than just averaging over events at different times. The Van Allen Probe orbits constrain the observations of the trapped radiation as a function of position and time, such that the position (L^*) of the satellite is, of course, dependent on time itself. Thus, we performed the superposed analysis by mapping the observations of the flux onto a grid. Passes of both Van Allen Probes A and B were discretized over a fixed L^*-epoch grid, with epoch time defined relative to the time of minimum LCDS in each storm. Note that for a single event, some of the cells remain empty because the satellites do not pass through them, due to their orbital coverage. In this case, these cells are ignored when calculating superposed epoch values across the selected events. In particular, for this study, we used a grid with 120 cells in the superposed epoch ranging from -3 to 3 days, and with 50 cells in L^* ranging from 1 to 7.5. This creates a relatively even observational coverage with each cell containing $\sim$32 storms (Supplementary Figure E.3). Also, note that during epoch time zero, because of the decrease in L^* along the Van Allen Probe orbits due to the storm-time variations in magnetic fields, there is a decrease to < 15 storms

for L^* ranges above 5.5 which was further filtered to neglect measurements outside the LCDS.

B.2 Fitting of Flux Cross-Sections

The function used for fitting the normalized flux for constant L^* and energy (cf. Figure 3.3, 3.4 in the main text) is shown in equation (B.1),

$$\log_{10} f(t) = \begin{cases} (A - b_1) \exp\left\{-\frac{(t-t_0)^2}{2\sigma_1^2}\right\} + b_1, & \text{if } t < t_0, \\ (A - b_2) \exp\left\{-\frac{(t-t_0)^2}{2\sigma_2^2}\right\} + b_2, & \text{otherwise,} \end{cases} \tag{B.1}$$

where A, b_1, b_2, t_0, σ_1, and σ_2 are fit parameters, t is the superposed epoch time, and f is the electron flux, normalized to the pre-storm level. The fitting was performed using the numerical `curve_fit` routine, available in the `scipy` python package. Additionally, this routine provides the fitting uncertainties for all of the parameters: δA, δb_1, δb_2, $\delta \mu$, $\delta \sigma_1$, and $\delta \sigma_2$.

The value 10^{-A}, obtained from fitting the logarithm of normalized flux, defines by how much the initial pre-storm flux is greater than the minimum flux reached by the end of the loss phase. It is the value plotted in Figure 4 as a function of L^* and fixed energy. The parameter t_0 defines the epoch time when the loss ends. At that time the flux reached its minima and starts recovering. In addition, epoch times of the beginning and end of the loss are estimated using quantities $t_0 - 3\sigma_1$ and t_0 respectively. Both of those values are plotted in Figure 5.

B.3 Median Flux Phase Space Density Calculation

The general approach for calculating phase space density (PSD) from the directional differential electron flux measurements has been described in a number of prior studies (*Mann et al.*, 2018; *Ozeke et al.*, 2019). In this study, we used a number of assumptions to try to ensure that the PSD, in particular when obtained from the superposed epoch analysis flux shown in Figure 6, remained statistically well-behaved. In particular, we performed interpolation

between MagEIS and REPT energy channels to obtain PSD at constant first adiabatic invariants, and investigated only low second invariants. As was discussed in the main text, the pre-storm phase is mostly characterized by constant flux. Meanwhile, during the loss phase, the dynamics are most well-characterized by the fractional flux loss. Thus, first, we perform a calculation of the well-behaved pre-storm PSD from the median pre-storm flux (top row of Supplementary Figure E.4). Second, we calculate the relative PSD change from the median fractional flux during the loss phase (middle row of Supplementary Figure E.4). And finally, we modify the pre-storm PSD by the calculated relative PSD to obtain phase space density L^* trace during the active storm times (bottom row of Supplementary Figure E.4). This approach allows us to work with a well-behaved PSD derived from the self-similar flux dynamics as represented by the statistical median flux.

Appendix C

Magnetic Field Model Validation During the September 2017 Geomagnetic Sotrm

This supplementary information provides an overview of the magnetic field measurement data from NASA Van Allen Probes mission in comparison with the *Tsyganenko and Sitnov* (2005) magnetic field model. This comparison is crucial for evaluating the validity of the conversion from the measured electron flux (as a function of the location, energy, and pitch angle) to electron phase space density (PSD) as a function of the three adiabatic invariants μ, K, and L^*. We also use data from the THEMIS-D satellite (*Angelopoulos*, 2008) to determine the location of the magnetopause from particle detector data and hence further validate the importance of magnetopause shadowing for radiation belt loss and the significance of the location of the last closed drift shell (LCDS) for the storm-time radiation belt dynamics during storm recovery phase.

Figure 4 of the main paper shows the two measured PSD profiles as a function of L^* for fixed μ and K observed by Van Allen Probes A and B. It also shows the instantaneous PSD gradients inferred from the satellite data at different L^* at the same time. These gradients are shown for the period from 13:00 UT until 13:20 UT on September 8, 2017. During this time, the measured magnetic field is in good (<10% difference in magnitude) agreement with the *Tsyganenko and Sitnov* (2005) magnetic field model and the Van Allen Probes

are sufficiently apart to infer the PSD gradients. However, outside of the aforementioned time slot, the Van Allen Probes are close to the magnetopause and boundary layer currents, which causes a disagreement with the magnetic field model. Figures E.8 and E.9 provide an overview of the magnetic fields observed by the satellites around that time. Hence, only the instantaneous gradients are only shown for the valid time period from 13:00 UT until 13:20 UT.

Figure E.8 shows three components of the magnetic field in the GSM coordinate system measured by the Van Allen Probe A during its outbound pass. Figure E.8 also shows the absolute value of the measured magnetic field vector as well as that from the *Tsyganenko and Sitnov* (2005) magnetic field model. Note that the measured magnetic field is in good agreement with the one from the model until 13:40 UT on September 8. However, the PSD data for Probe A at the value of second adiabatic invariant K =0.04 $R_E G^{0.5}$ assessed in this study exists only until 13:20 UT, because at later times the particles with K =0.04 $R_E G^{0.5}$ mirror below the satellite.

Similarly, Figure E.9 shows the measured and modeled magnetic field for Van Allen Probe B during its inbound pass. As the satellite moves inwards, it leaves the boundary Chapman-Ferraro layer at 12:45 UT, which is evident by the decrease in the absolute value of the magnetic field. At 12:45 UT the L^* values of both Van Allen Probes are the same (difference in L^* is <0.1), therefore it is hard to infer the directionality of the PSD gradients until the time past their crossing in L^* crossing, i.e., only after 13:00 UT.

To verify that the Van Allen Probes are indeed close to the magnetopause at the assessed times, we show a summary of THEMIS-D satellite measurements in Figure E.10. THEMIS-D crosses the magnetopause around 13:00 UT on September 8, 2017, which is evident in the magnetic field and the particle flux data from the satellite. Interestingly, this is the time of rapid last closed drift shell (LCDS) compression (cf. Figure 1 of the main paper). At the time of the magnetopause crossing by the THEMIS-D satellite at around 13:00 UT, which is also the time of the Van Allen Probe conjunction, its L^* location is 4.3 (according to *Tsyganenko and Sitnov*, 2005, magnetic field model for K =0.04 $R_E G^{0.5}$). This suggests that the magnetic field model

underestimates the extent of the rapid magnetopause compression and is not capable to invalidate the PSD data at that time. Such observations further strengthen the selected timeslot of 13:00-13:20 used in the analysis of the PSD gradients in the main paper.

Appendix D

Estimating Electron Phase Space Density from the GPS Electron Flux Data

D.1 Global Positioning System phase space density data

The Combined X-Ray Dosimeter (CXD) is a wide-angle (approximately hemispheric) energetic charged particle detector that measures the radiation environment in medium-Earth orbit (*Morley et al.*, 2016). The central look direction of the detector is towards the Earth. As the GPS satellites carry no magnetometer and CXD does not provide a directionally-resolved measurement, the publicly released data product provides omnidirectional electron flux data and not directional flux (*Morley et al.*, 2017). The omnidirectional flux provided by CXD, $J_{\mathrm{GPS}}(E)$, can be expressed as an integral of the flux of all particles, averaged over all solid angles:

$$J_{\mathrm{GPS}}(E) = \frac{1}{4\pi}\int\int d\Omega j\left(E,\alpha\right) = \int_0^{\pi/2} j\left(E,\alpha\right)\sin\alpha d\alpha,$$

where $j\left(E,\alpha_{eq}\right)$ if the directional differential electron flux, assumed symmetric around magnetic equator and $d\Omega$ is a solid angle element. We can rewrite this equation for J_{GPS} in terms of the equatorial pitch angle α_{eq}:

$$J_{\mathrm{GPS}}(E) = \frac{B}{B_{eq}}\int_0^{\alpha_{90}} j\left(E,\alpha_{eq}\right)\frac{\sin\alpha_{eq}\cos\alpha_{eq}}{\sqrt{1-\frac{B}{B_{eq}}\sin^2\alpha_{eq}}}d\alpha_{eq},$$

where B and B_{eq} are the magnetic field strengths at the satellite and the magnetic equator respectively and $\alpha_{90} = \arcsin\left(\sqrt{\frac{B_{eq}}{B}}\right)$ is the equatorial pitch angle that corresponds to the local 90° pitch angle.

The CXD omnidirectional flux has previously been cross-calibrated against data from the Van Allen probes, showing that the data from both missions are consistent for energies up to ∼4 MeV (*Morley et al.*, 2016). Higher energies could not be adequately cross-calibrated due to the absence of significant flux at higher energies during the set of physical conjunctions used for calibration. In this work we use electron flux data from 20 GPS satellites: vehicles ns53-ns59 and ns61-ns73 (see *Carver et al.*, 2020, for satellite information). To ensure the high quality of the differential flux data used for the PSD calculations, we first discard bad data using the "`dropped_data`" flag from the GPS data set. We further exclude data where the spectral forward model does not adequately reproduce the count rates in the first five energy channels using the criterion given in *Smirnov et al.* (2020). This quality flag is biased to exclude lower fluxes in addition to inadequate fits and is therefore overly conservative.

To evaluate the electron phase space density (PSD), the directional differential electron flux is needed. Here, we use the pitch angle distribution (PAD) model of *Zhao et al.* (2018) to simulate the shape of the PAD, $\tilde{j}\left(E, \alpha_{eq}\right)$, at the GPS satellites. This model is corrected by normalizing it by the GPS measurements, thus, ensuring that both model and observations are consistent with each other. The absolute value of the directional differential flux j can be represented as $j\left(E, \alpha_{eq}\right) = N(E)\tilde{j}\left(E, \alpha_{eq}\right)$, where $N(E)$ is a normalization coefficient that can depend on energy. By substituting this relation into equation above, we can determine the normalization coefficient $N(E)$ for a modeled $\tilde{j}$, and therefore estimate $j\left(E, \alpha_{eq}\right)$ using the following formula:

$$j(E, \alpha_{eq}) = \frac{J_{\mathrm{GPS}}(E)}{\frac{B}{B_{eq}} \int_0^{\alpha_{90}} \tilde{j}\left(E, \alpha_{eq}\right) \frac{\sin\alpha_{eq}\cos\alpha_{eq}}{\sqrt{1-\frac{B}{B_{eq}}\sin^2\alpha_{eq}}} d\alpha_{eq}} \cdot \tilde{j}\left(E, \alpha_{eq}\right).$$

This provides an estimation of directional differential electron flux, enabling calculation of PSD. In case of the *Zhao et al. (2018)* (*Zhao et al.*, 2018) model used in this study, the integral can be solved analytically.

Once $j(E, \alpha_{eq})$ has been derived, we calculate the PSD in adiabatic invariant coordinates, $f_{GPS}(\mu, K)$, following the method outlined by *Morley et al.* (2013), as applied to Van Allen Probes data by *Olifer et al.* (2021c). In brief, Liouville's theorem states that phase space density is conserved along dynamical trajectories, and is given by:

$$f(E, \alpha) = \frac{j(E, \alpha)}{p^2}$$

where p is the relativistic momentum of the particle. For instruments that have directionally-resolved measurements the conversion from $f(E, \alpha)$ to $f(\mu, K)$ typically relies on fitting or interpolation from the measurements to the desired adiabatic invariants. However, for the GPS data we pre-selected the values of K and because we obtain $j(E, \alpha)$ through application of a PAD model we simply evaluate the PAD model at the α corresponding to the desired K at each time step. The adiabatic invariant calculations are dependent on a magnetic field model, and for this work we use the *Tsyganenko and Sitnov* (2005) model.

D.2 Van Allen Probes phase space density data and comparison to GPS

We use Van Allen Probes directional electron flux data from the magnetic electron ion spectrometer (MagEIS) *Blake et al.* (2013) and relativistic electron-proton telescope (REPT) (*Baker et al.*, 2012) charged particle instruments to calculate phase space density, $f_{RBSP}(\mu, K, L^*)$. Therefore we can omit the pitch angle distribution modeling step described for the GPS data processing. The procedure largely follows *Morley et al.* (2013) and has been used to calculate PSD from the Van Allen Probes for previous work *Olifer et al.* (2021c). The second and third adiabatic invariants – K and L^* are calculated using the *Tsyganenko and Sitnov* (2005) model. We used the magnetic field measurements from the Electric and Magnetic Field Instrument Suite and Integrated Science (EMFISIS) suite (*Kletzing et al.*, 2013) to calculate the first adiabatic invariant.

To ensure that the calculation of PSD using the omnidirectional electron flux from CXD is sufficiently accurate, we performed phase space density matching

(*Chen et al.*, 2007b; *Morley et al.*, 2013). That is, where we have valid PSD, $f(\mu, K, L^*)$, from both satellites we expect that f_{GPS} should equal f_{RBSP}. Supplementary Fig. 1 shows that the evaluated GPS PSD is in good agreement with that of the Van Allen Probes across the three adiabatic invariants used in this study. Nonetheless, a relatively small systematic bias – of a factor of two at most – exists for the particle populations with energies above 1 MeV. When compared, the GPS PSD tend to be smaller than those from the Van Allen Probes at higher energies. For an accurate comparison between the two datasets, we correct for this energy-dependent bias in the GPS PSD dataset such that it minimizes the magnitude of the symmetric signed percentage bias (*Morley et al.*, 2018).

D.3 Estimating Uncertainties in PSD calculation

In general, the uncertainty in the estimated PSD values is a combination of the measured flux uncertainty and the uncertainties related to the magnetic field model. However, for the purposes of this study, we assume the uncertainty in the flux measurement is small compared to the uncertainty arising from the use of a magnetic field model in estimating the adiabatic invariants (cf., *Reeves et al.*, 2013). Error propagation allows us to estimate the absolute uncertainty, $\Delta f(\mu, K, L^*)$, using partial derivatives of $\log_e f$ and individual uncertainties in μ, K, and L^* as per the following formula:

$$\frac{\Delta f}{f} = \sqrt{\left(\frac{\partial \log_e f}{\partial \mu}\Delta\mu\right)^2 + \left(\frac{\partial \log_e f}{\partial K}\Delta K\right)^2 + \left(\frac{\partial \log_e f}{\partial L^*}\Delta L^*\right)^2}.$$

Note that this equation assumes individual uncertainties in μ, K, and L^* to be Gaussian. Uncertainty related to K has not yet been evaluated in the literature, and therefore we neglect this term in our present error analysis.

The error in μ is related to the uncertainty of the estimated magnetic field strength at the location of the satellite (*Morley et al.*, 2013). *Brito and Morley* (2017) estimated this error to be around 4% by comparing the modeled and measured magnetic fields from a variety of spacecraft missions. As the GPS

satellites do not make in situ magnetic field measurements we use this result and set the error in μ to be 4%. While not exact, this assumption allows us to evaluate the order of magnitude of the related uncertainty in f that would vary depending on the $\frac{\partial \log_e f}{\partial \mu}$ gradient.

The error in L^* can be estimated using the method of *Chen et al.* (2007b). The relative uncertainty in f can be estimated by comparing PSD from different GPS satellites or with those from RBSP and utilizing equation

$$\frac{\partial \log_e f}{\partial L^*} \Delta L^* = \frac{R-1}{R+1},$$

where $R = \exp |\log_e f_i - \log_e f_j|$ and f_i and f_j are the PSD from two different satellites for the same adiabatic coordinates and time. This approach for calculating uncertainties provides an estimation of error in PSD for every satellite and time. Fig. 2 shows the median error across all 20 GPS spacecraft used in this study and times shown in the legend on the right.

D.4 Estimating Radial Diffusion Coefficients D_{LL} from GPS PSD Data

Using the GPS satellites we are able to accurately resolve radiation belt dynamics (i.e., $f(\mu, K, L^*)$), on timescales of minutes, over a limited range of L^*. Availability of such measurements allows us to evaluate the radial diffusion coefficients, D_{LL}, directly from the particle measurements. Notably, calculation of the D_{LL} coefficients on such short timescales has, to our knowledge, not previously been reported. Here it is made possible by the constellation of GPS satellites providing good coverage of adiabatic coordinate space at each time, essentially giving near-continuous monitoring of a limited range of drift shells.

The radial diffusion coefficient can be estimated using a quadrature equation first described by *Schulz and Lanzerotti* (1974):

$$D_{LL} \equiv D_n L^n = \left\{ F(t_2) - F(t_1) + \frac{t_2 - t_1}{\tau} \right\} \cdot \left\{ \int_{t_1}^{t_2} \left[\left(\frac{n-2}{L} \right) \frac{\partial F}{\partial L} + \frac{\partial^2 F}{\partial L^2} + \left(\frac{\partial F}{\partial L} \right)^2 \right] dt \right\}^{-1},$$

where $F \equiv \log_e f$; D_n is the normalization of the radial diffusion coefficient that does not depend on L; n is the order of L dependence of the D_{LL} coefficient

(typically ranging from 6 to 8); t_1 and t_2 are the fixed moments in time between which the calculation of the D_{LL} coefficient is performed; and τ is the lifetime of the particle which can typically describe additional loss, or acceleration, processes in a reduced diffusion equation. In this study we use an empirical characterization of the electron lifetime $\tau = 5/Kp$ (*Shprits et al.*, 2006). By numerically calculating gradients of F and integrating them over a range of times, we can estimate D_{LL} coefficients during the storm. For this work L in the equation for calculating D_{LL} coefficients can be considered equivalent to L^* (see also the discussion in *Cunningham et al.*, 2018).

Appendix E

Supplementary Figures

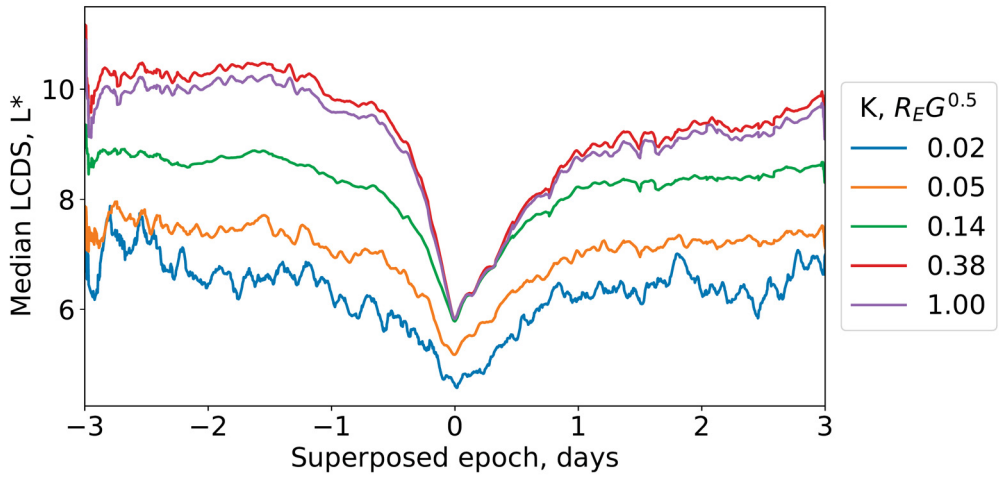

Figure E.1: Superposed epoch analysis of the median LCDS location at different second adiabatic invariants K, obtained from the full calculation by the LANLGeoMag library (*Henderson et al.*, 2017) for every storm.

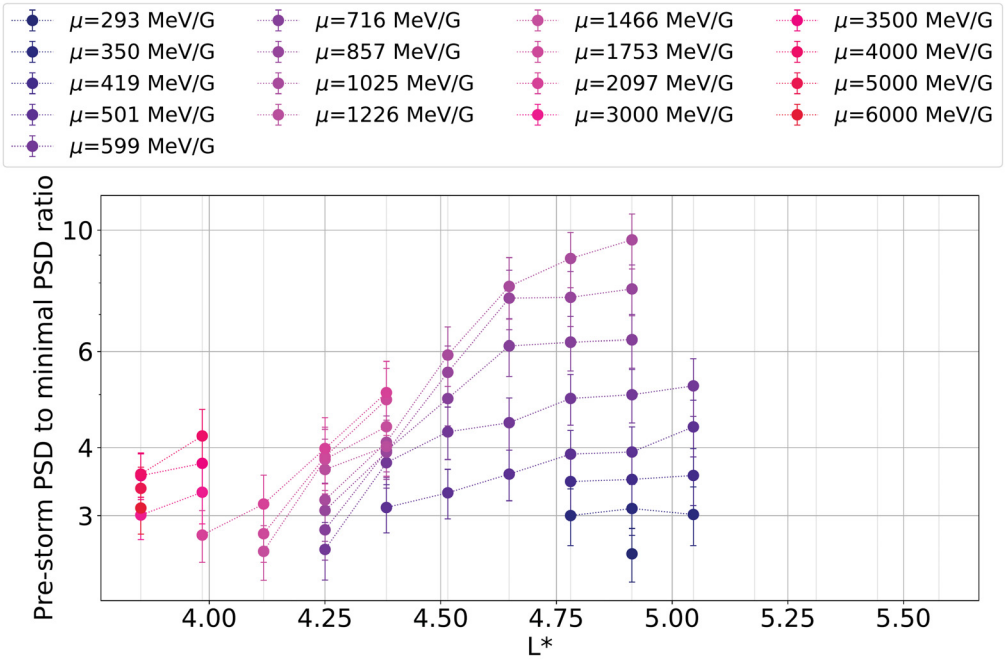

Figure E.2: The intensity of the fractional phase space density (PSD) loss for different μ as a function of L^* in the Van Allen radiation belt. Different first adiabatic invariants, μ, are shown in different colors, the second adiabatic invariant K is fixed at 0.1 $R_E G^{0.5}$. The error bars were obtained from the least-squares numerical fitting of the fractional PSD with a double-sided Gaussian (see main text for details).

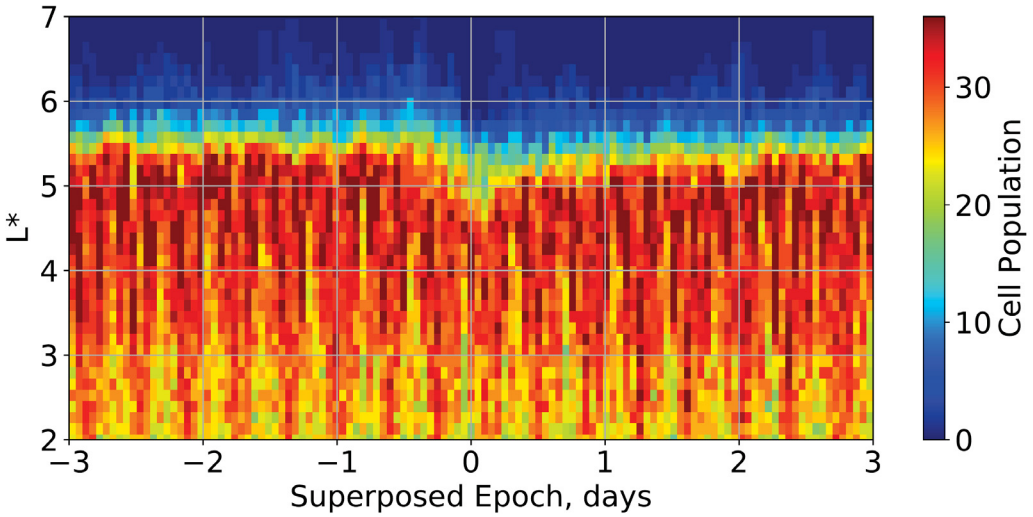

Figure E.3: Number of storms that contributed to each cell in the 2D superposed epoch analysis. The number of events per cell which was used when determining the median flux in the superposed epoch analysis is shown as a function of L^* and epoch day by the color bar. Note that the average cell coverage for the L^* range from 3 to 5 is 32 storms per cell with a standard deviation of 3. The grid used in this study contains 120 cells in the superposed epoch ranging from -3 to 3 days and with 50 cells in L^* ranging from 1 to 7.5.

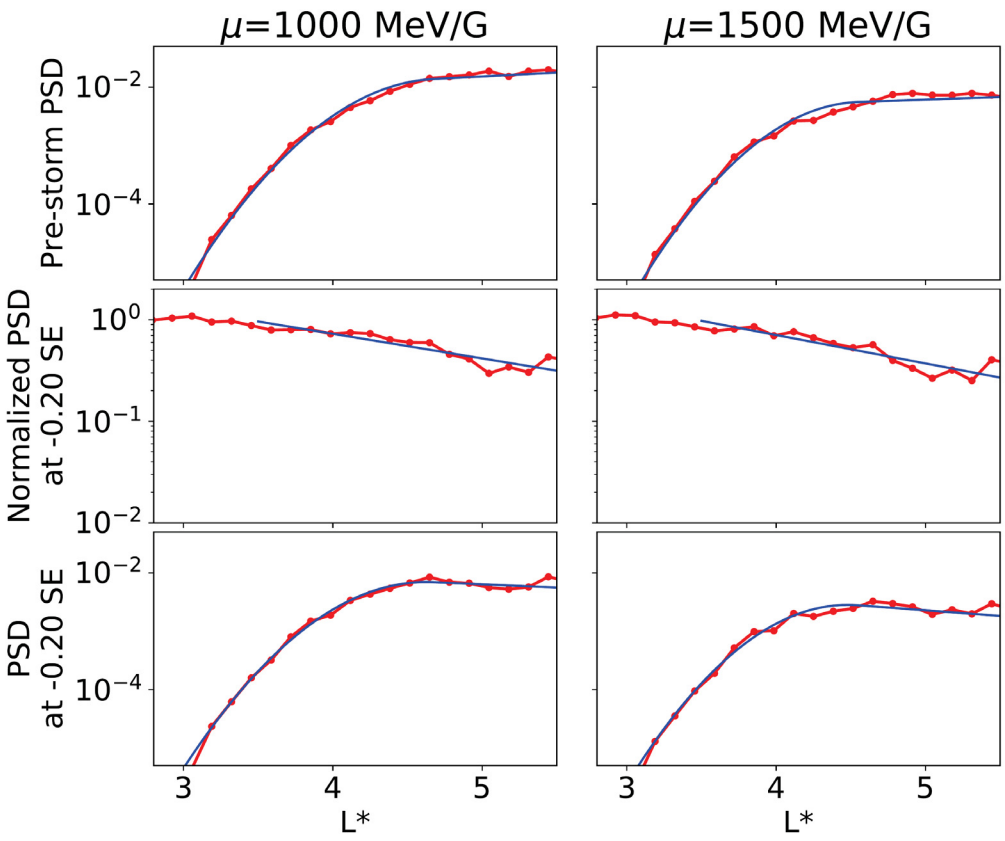

Figure E.4: Example of the application of the technique used for statistical phase space density (PSD) calculation from observed median flux. The PSD profile as a function of L^* at any given time (bottom panel; in this case 0.2 days before the superposed epoch (SE) of minimum LCDS) is obtained by multiplying the pre-storm PSD (top panel) and the fractional PSD change (middle panel). The left and right columns represent the data for two examples of different first adiabatic invariants. The red line with dots represents the data and the blue lines represent the fits used in the calculation of PSD radial gradients shown in Figure 6 of the main paper.

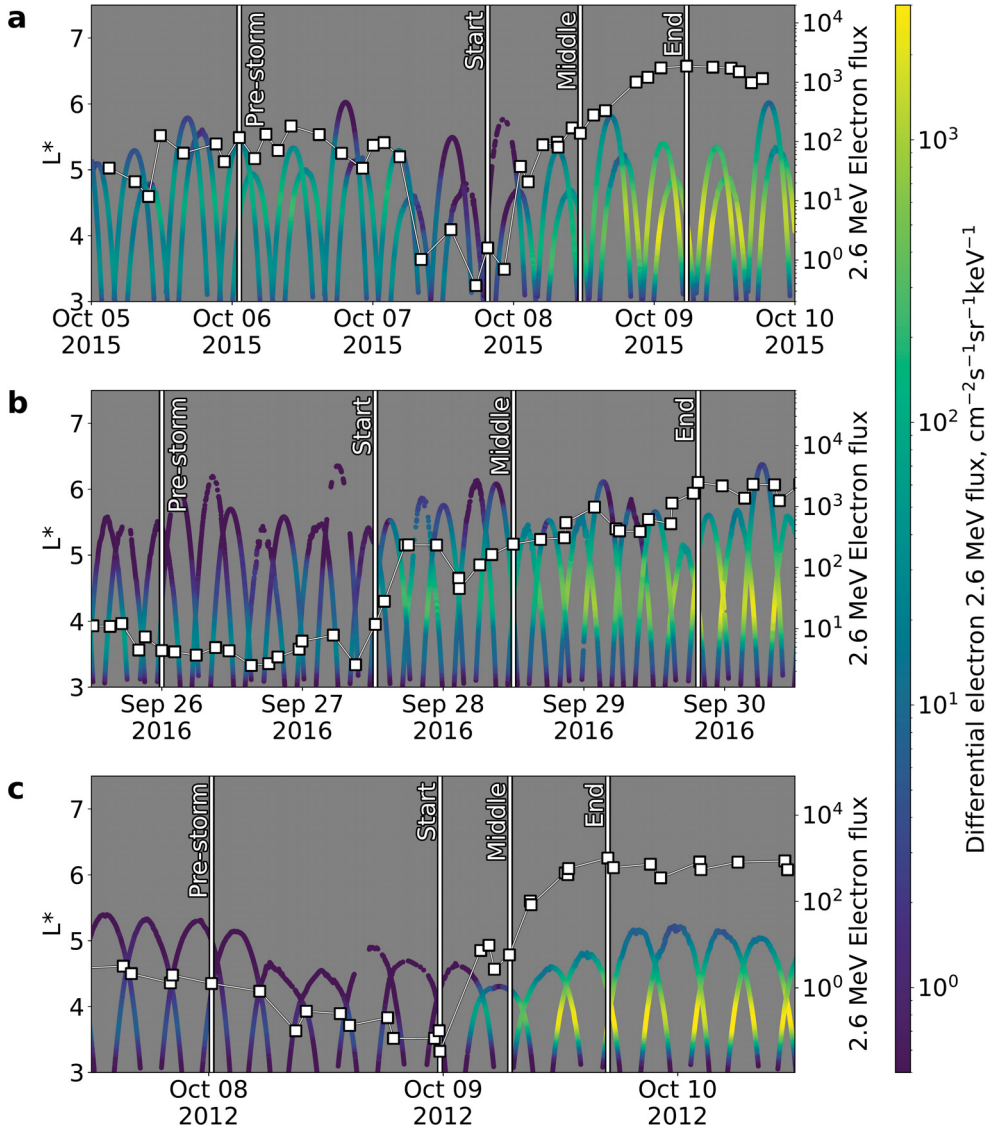

Figure E.5: Measured 2.6 MeV energy differential flux for 90° pitch angle electrons in the same format as Figure 5.1 of the main paper. **a**, electron flux data for the October 6-10, 2015 geomagnetic storm. **b**, electron flux during the September 26-30, 2016 storm **c**, the October 8-10, 2012 geomagnetic storm. All panels designate 4 times where the comparison to the Kennel-Petschek limit is conducted.

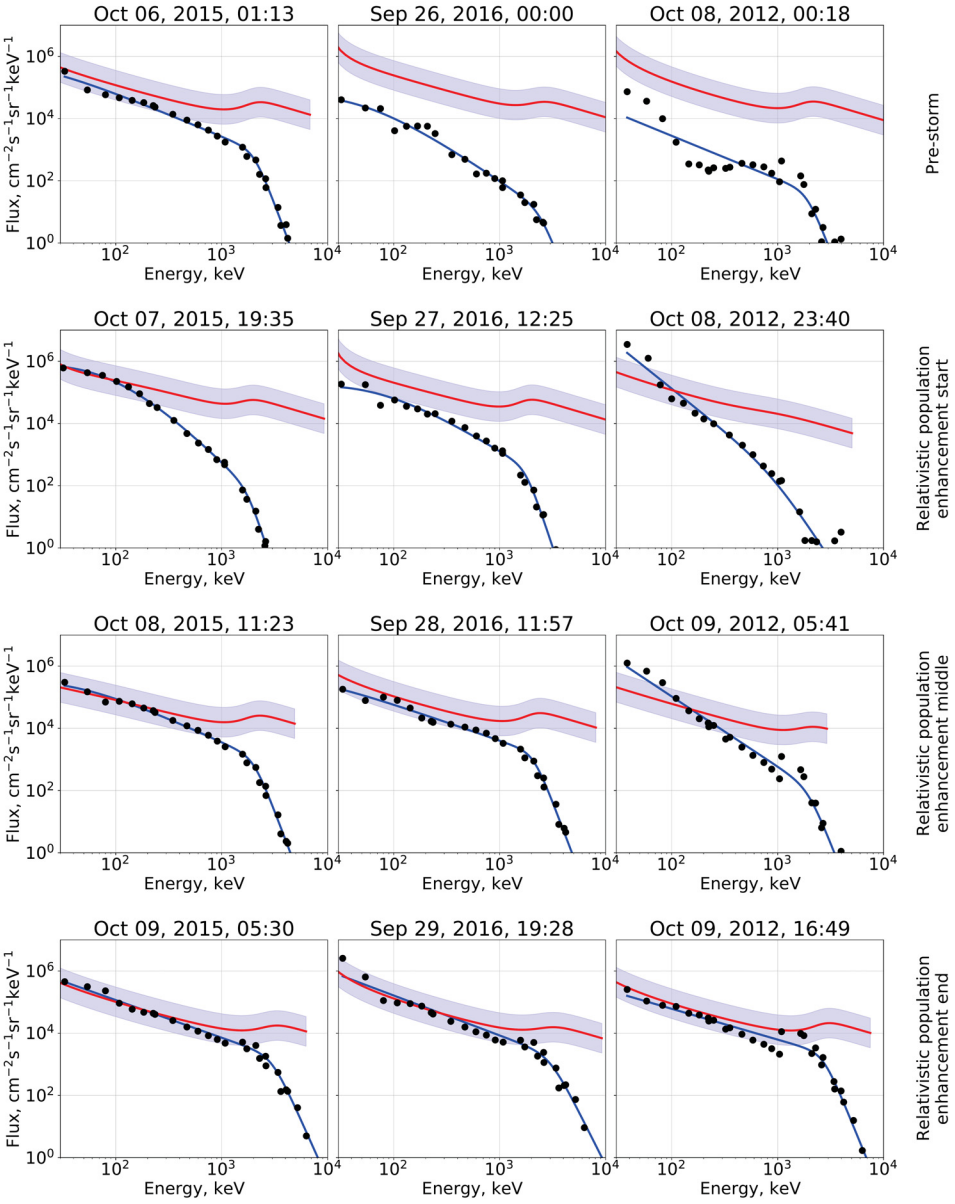

Figure E.6: Electron flux energy spectra and Kennel-Petschek limits during, **a**, the October 6-10, 2015 geomagnetic storm, **b**, the September 26-30, 2016 geomagnetic storm, **c**, the October 8-10, 2012 geomagnetic storm. This figure has the same format as that of Figure 5.2 of the main paper.

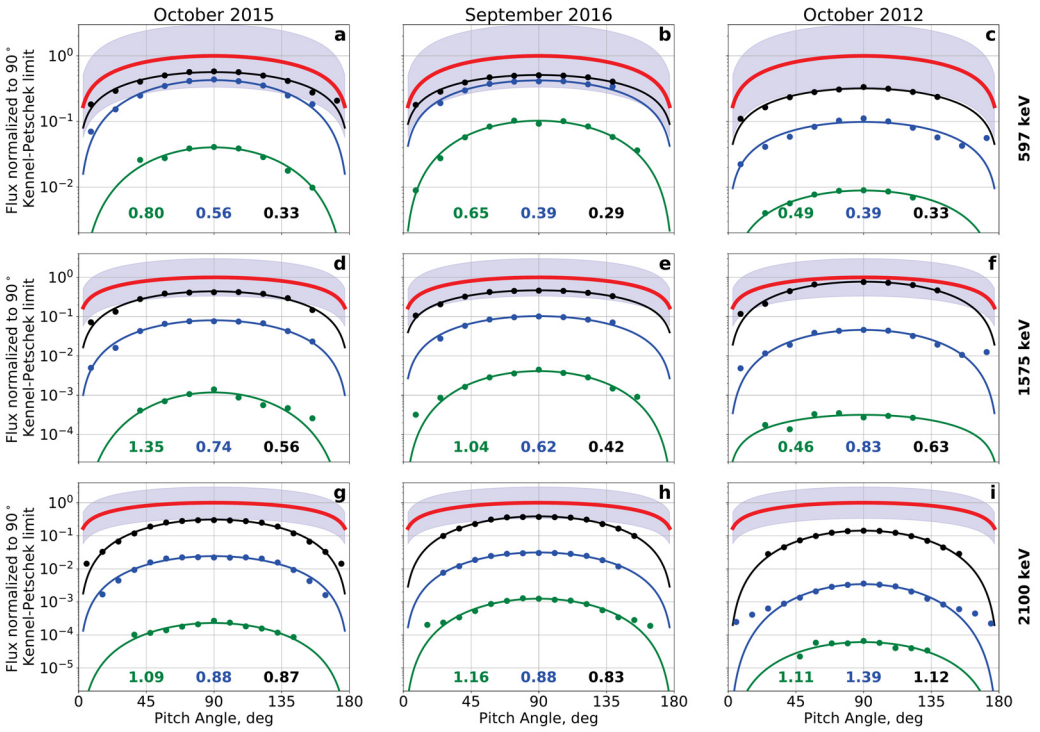

Figure E.7: Normalized electron flux pitch angle distributions at L^*=4.25 and corresponding Kennel-Petschek limits during, left column, the October 6-10, 2015 geomagnetic storm, middle column, the September 26-30, 2016 geomagnetic storm, right column, the October 8-10, 2012 geomagnetic storm. This figure has the same format as that of Figure 5.3 of the main paper.

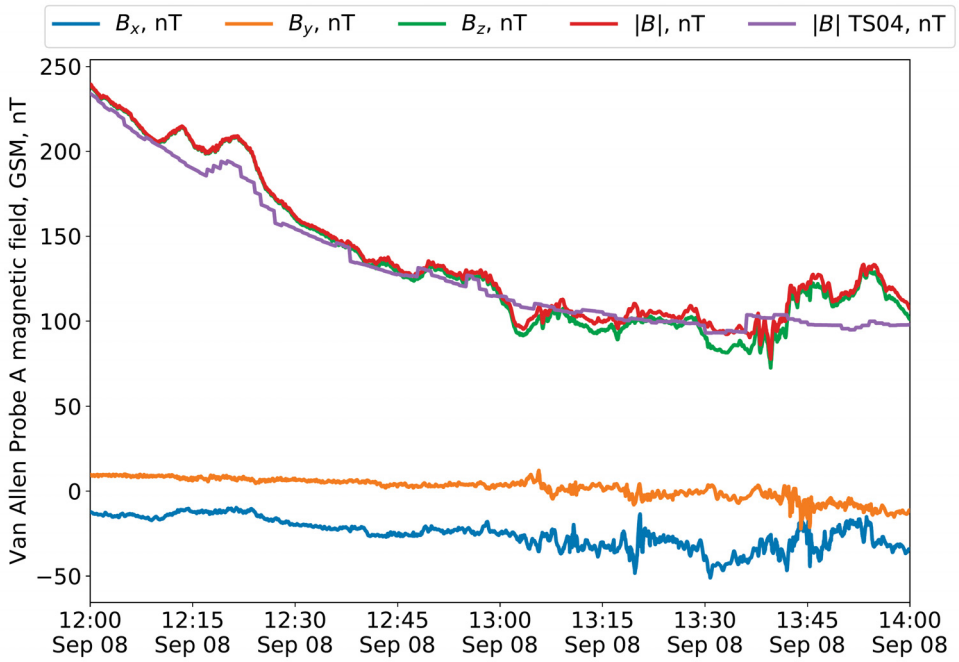

Figure E.8: Van Allen Probe A model and measured magnetic field data during the acceleration phase from 12 UT until 14 UT on September 8, 2017. Measured components of the magnetic field in the GSM coordinate system are shown in blue, orange, and green colors. The red color corresponds to the absolute value of the measured magnetic field vector and is used in the calculation of the first adiabatic invariant μ. The absolute value of the modeled magnetic field vector (*Tsyganenko and Sitnov*, 2005) is shown in purple. A comparison between the measured and modeled data provides a reliable assessment of the model data quality and is used to distinguish where the quantitative analysis of PSD is valid.

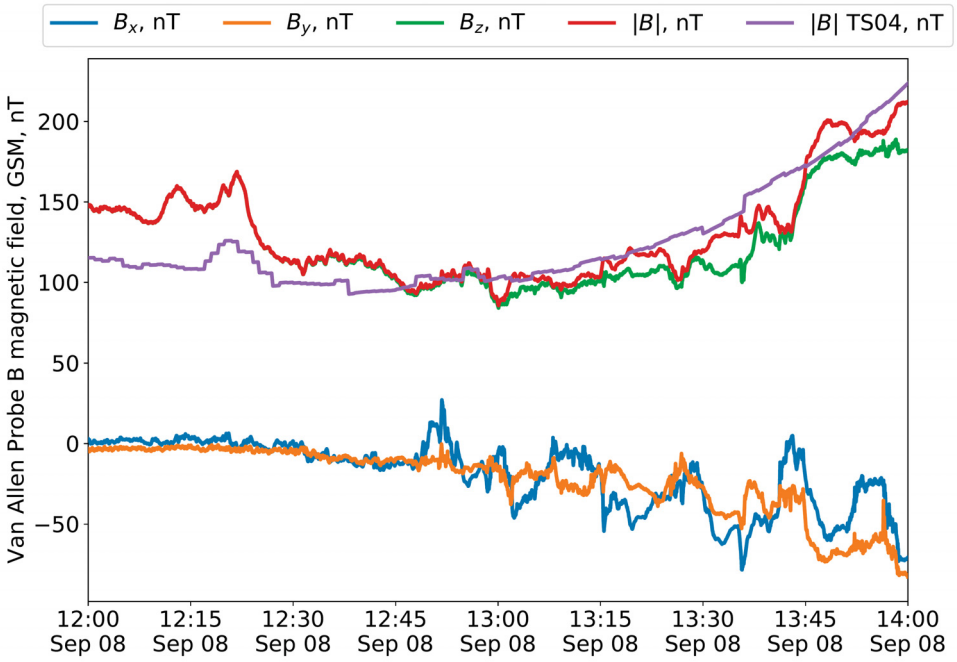

Figure E.9: Van Allen Probe B model and measured magnetic field data in the same format as Figure E.8.

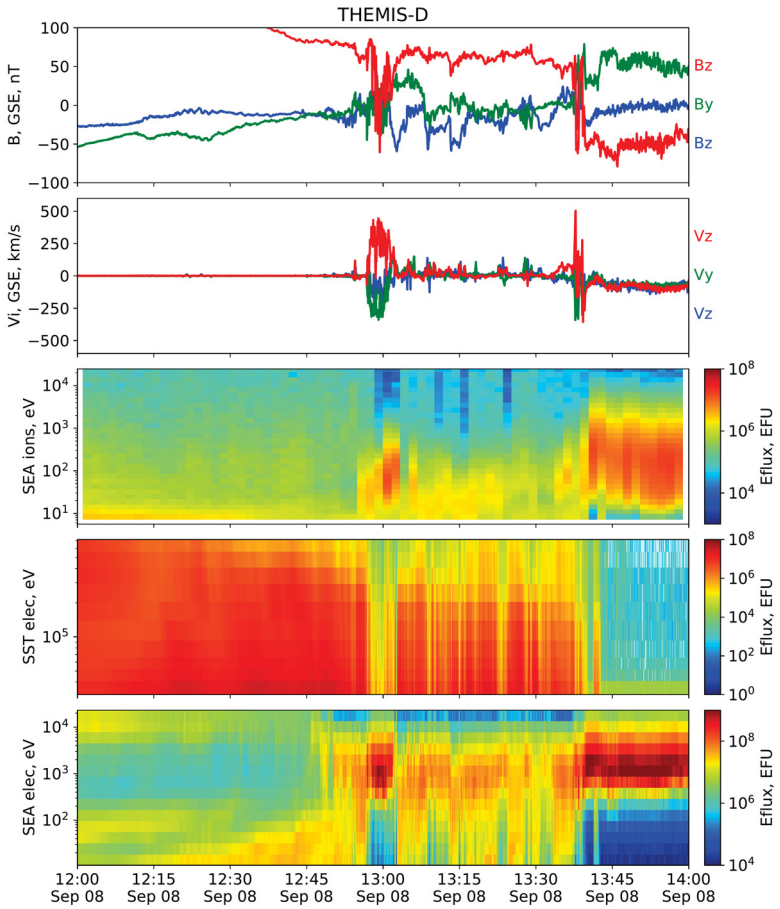

Figure E.10: A summary plot of THEMIS-D magnetic field and particle measurements. From top to bottom, the panels show magnetic field components in the GSE coordinate system, ion plasma flow velocity in the GSE coordinate system, and ion energy flux from the electrostatic analyzer (ESA), solid-state telescope (SST) electron energy flux, ESA electron energy flux. THEMIS-D briefly crosses the magnetopause at 12:57 UT, which corresponds to a sharp decrease in B_z component of the magnetic field, an increase in the ion drift velocity measurement of the warm sheath plasma populations, and a rapid drop in the electron measurements above 10 keV. THEMIS-D then enters the boundary layer, before crossing into the clean magnetosheath around 13:40 UT.

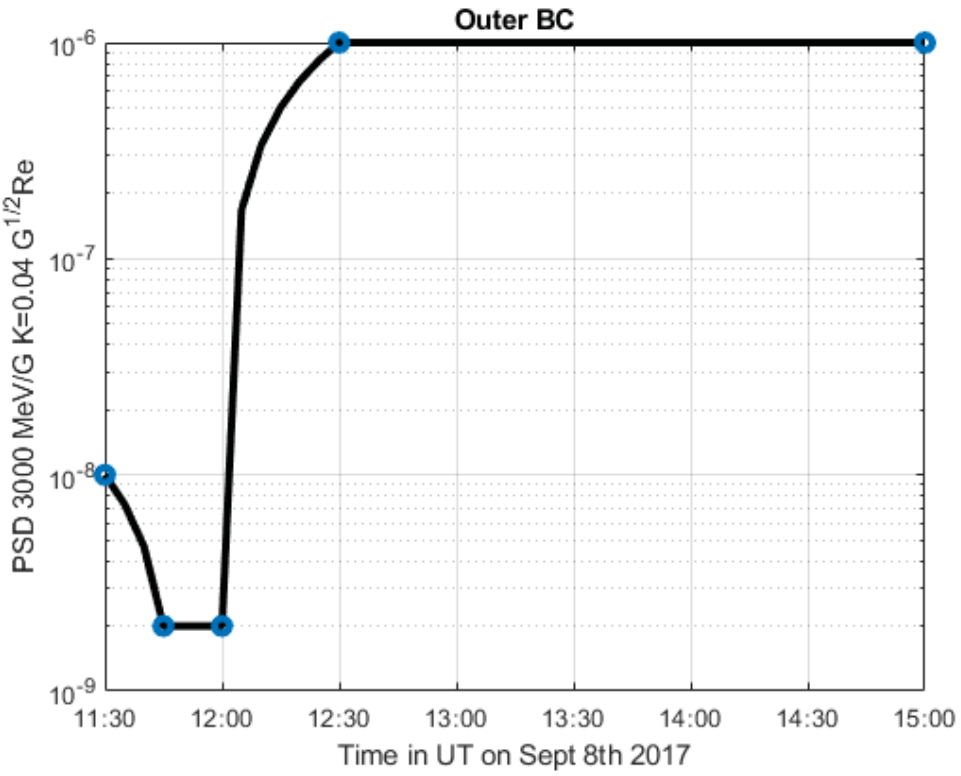

Figure E.11: Outer boundary conditions used in the radial diffusion simulation. The figure represents a short loss period, observed by Van Allen Probe B from 11:30 UT until 12:00 UT, which coincides with the inward motion of the last closed drift shell (LCDS), followed by a sharp assumed enhancement of the outer boundary electron population which acts as a source for the subsequent inwards radial diffusion. Note that these data were inferred from the observed electron phase space density data at fixed μ=3000 MeV/G and K=0.04 $R_E G^{0.5}$. However, such dynamics are representative of the relativistic electron population at other μ and K values as explained in the main text of the paper.

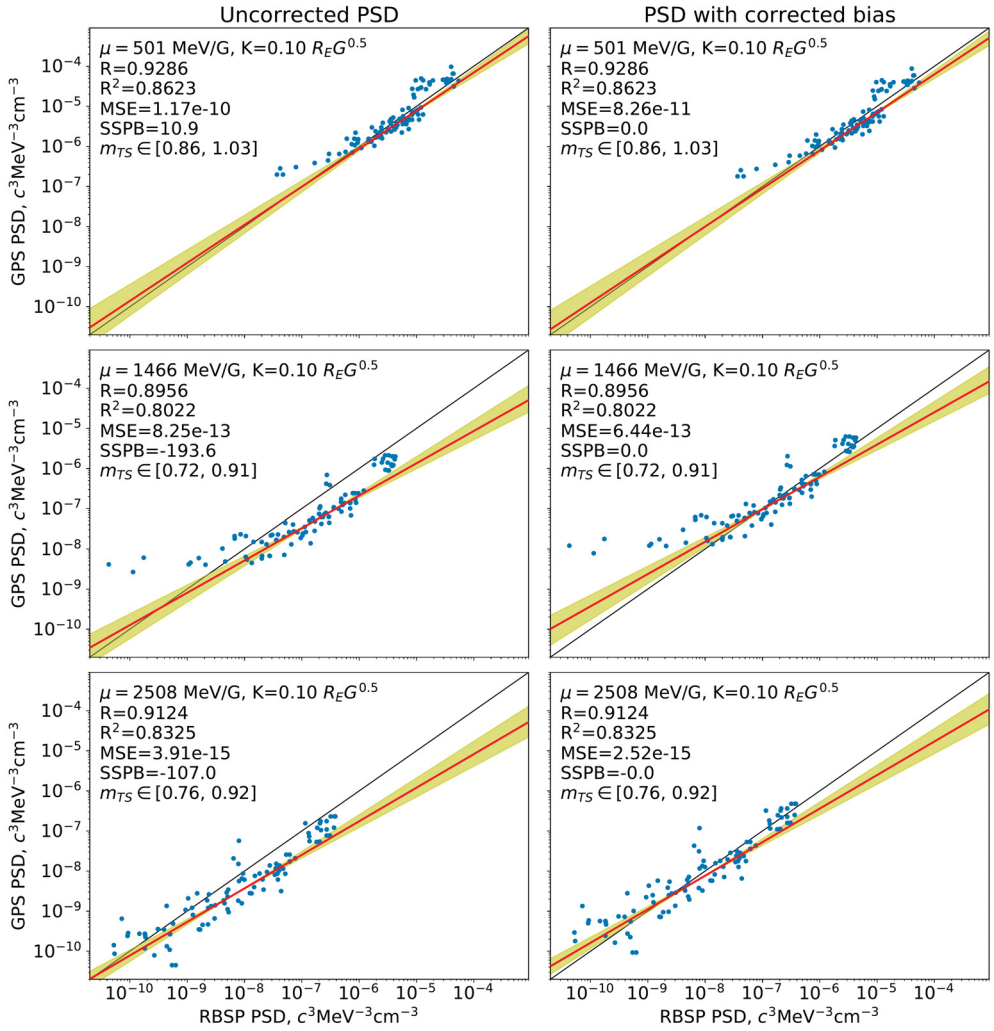

Figure E.12: Comparison between estimated electron phase space density from GPS satellite constellation and that of the Van Allen Probes during the August 2018 geomagnetic storm. Van Allen Probes PSD is shown on the x-axis and the estimated GPS PSD is shown on the y-axis. Only PSD measurements during the temporal and L^* conjunction are shown. Two columns show the GPS PSD data before and after correcting the bias of the GPS dataset to match the PSD levels from the Van Allen Probes. Different rows correspond to three different first adiabatic invariants μ, used in this study. Each panel also shows the Pearson correlation coefficient (R) and coefficient of determination (R^2) between the two data sets in log-space, mean square error (MSE), symmetric signed percentage bias (SSPB), and the 95% confidence interval for linear fit slope obtained using the Theil-Sen robust linear regression. The red line shows the resulting Theil-Sen fit with the yellow region showing the 95% confidence interval of the fit.

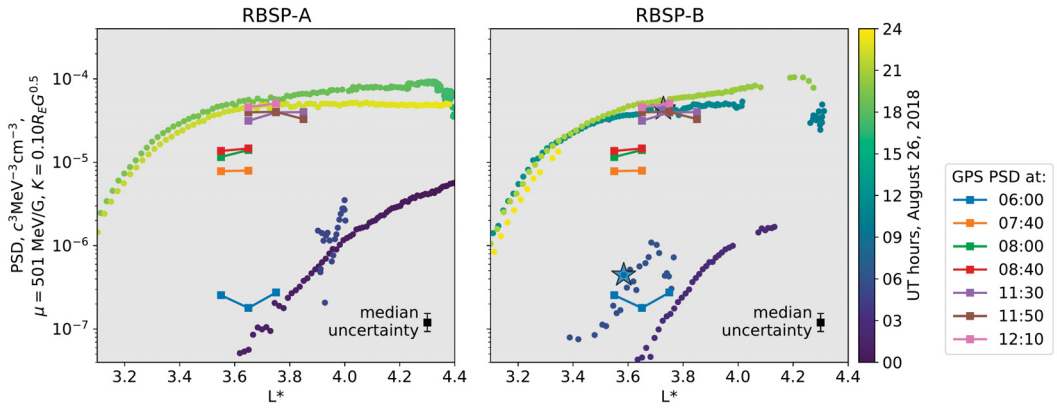

Figure E.13: Electron PSD profiles for μ=501 MeV/G population during the acceleration phase of the August 2018 geomagnetic storm. The electron PSD profiles obtained from the Van Allen Probes data are shown with a scatter plot in both panels (Probe A on the left and Probe B on the right). Due to the orbital movement of the spacecraft, the Van Allen Probes PSD is color-coded by UT time on August 26, 2018. The PSD profiles evaluated from the GPS satellites are shown with line plots, duplicated in both panels, during the first (06:00-08:40 UT) and second (11:50-12:10 UT) acceleration bursts. The star markers represent the times of conjunction between Van Allen Probe B and GPS at 06:00 UT and 11:30 UT. This plot is in the same format as Figure 7.2.

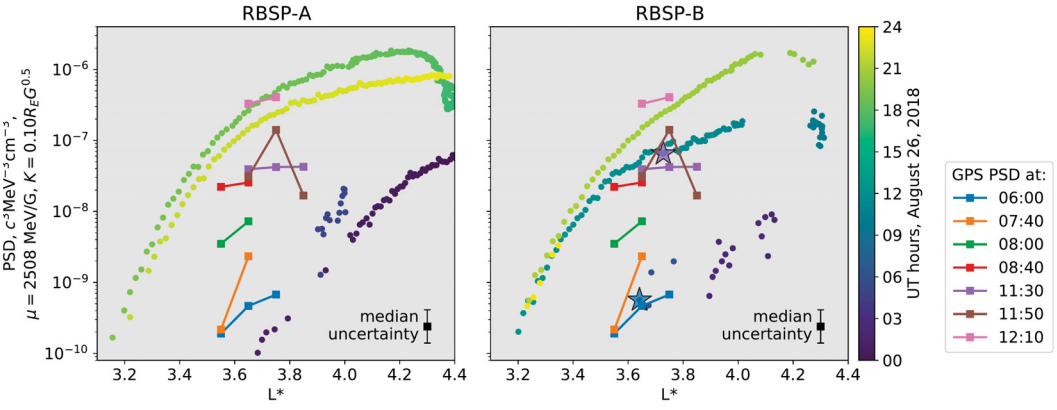

Figure E.14: Electron PSD profiles for μ=2508 MeV/G population during the acceleration phase of the August 2018 geomagnetic storm. Same format as Figure 7.2 and Supplementary Figure E.13.

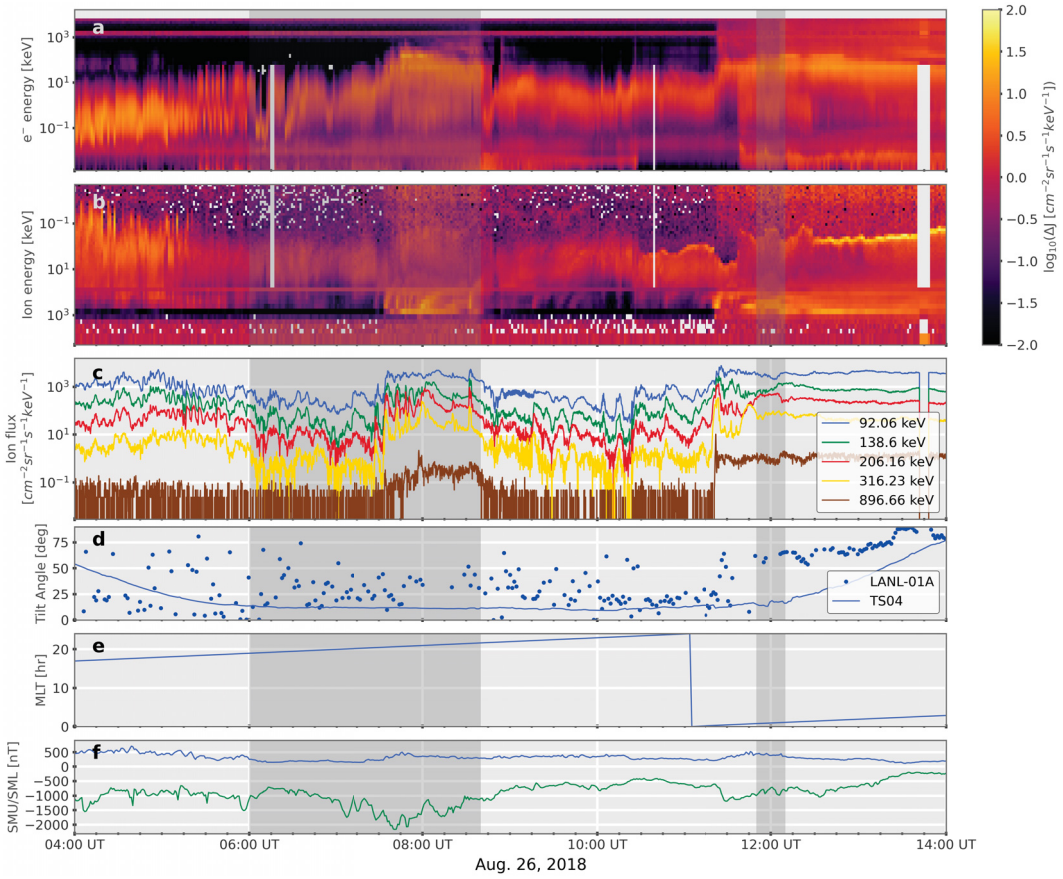

Figure E.15: Magnetic indices and geosynchronous measurements of energetic charged particles during the acceleration intervals. Panels **(a)** and **(b)** show spectrograms of flux perturbation, constructed by merging data from the MPA, SOPA, and ESP instruments on the LANL-01A geosynchronous satellite. The flux perturbation, ΔJ, is calculated as deviations of the differential flux from a robust average of $log_{10}(J)$ in that energy channel. This presentation is used to enhance energy-time dispersion signatures and the units associated with the color scale should be treated with caution. These panels are further shown in the McIlwain format, in which the proton energy axis is inverted. Panel **(c)** shows measured, spin-averaged ion fluxes between 92 keV and 897 keV. Dispersed charged particle injections, likely related to substorm activity with onset at ∼07:27 UTC, are seen in the second half of the first acceleration interval. Another substorm onset is observed at 11:18 UTC, Panel **(d)** displays the tilt-angle of the geomagnetic field derived from: (line) the Tsyganenko and Sitnov 2005 magnetic field model used in the body of this work, and; (dots) the 3D velocity distribution measured by the MPA instrument. The observational derivation relies on sufficient anisotropy being present to identify the symmetry axis and the derived vector is noisy and unreliable without sufficient anisotropy. We note here the clear dipolarization in conjunction with the substorm onset at 11:18 UTC. The magnetic local time of the satellite is plotted in panel **(e)**, and the SuperMAG SMU and SML indices are shown in panel **(f)**. The two acceleration intervals are highlighted in each panel by the grey boxes.